

UNIVERSITÉ DENIS DIDEROT  
PARIS 7

THÈSE

présentée  
pour obtenir le grade de

Docteur de l'Université Paris VII

**Spécialité:** *Astrophysique et Instrumentations Associées*

PAR AGLAÉ KELLERER

Assessing time scales of atmospheric  
turbulence at observatory sites

Soutenue le 7 Septembre 2007 devant la Commission d'examen :

*Président :* Pr. Gérard Rousset  
*Directeurs de thèse :* Dr. Vincent Coudé du Foresto  
Dr. Monika Petr-Gotzens  
*Rapporteurs :* Dr. Tony Travouillon  
Dr. Jean Vernin  
*Examineurs :* Dr. Thierry Fusco  
Dr. Marc Sarazin



*The worst moment for the atheist  
is when he is really thankful  
and has nobody to thank.*

Dante Gabriel Rossetti (1828-1882)

For me – as a really thankful atheist – it is a pleasure to have many people to thank, and first of all, my family.

I am grateful to my thesis supervisors Monika Petr-Gotzens and Vincent Coudé du Foresto and I am indebted to Marc Sarazin for very useful discussions and constant help. Thanks to Rodolphe Krawczyk who has followed my work with his natural enthusiasm, and to Tony Travouillon and Jean Vernin who have kindly accepted to referee this dissertation.

It was a pleasure and privilege to work with many other colleagues: Karim Agabi, Nancy Ageorges, Eric Aristidi, Gérardo Avila, Timothy Butterley, John Davis, Rosanna Faraggiana, Thierry Fusco, Michèle Gerbaldi, Christian Hummel, Pierre Kervella, Victor Kornilov, Stefan Kraus, Isabelle Mocoœur, Gérard Rousset, Tatyana Sadibekova, Klara Shabun, Bruno Valat, Martin Vannier, Richard Wilson, Markus Wittkowski.

Endless thanks go to Andrei Tokovinin. He patiently read through many drafts of my work. Deficiencies that remain, do so despite his best endeavors.



# Avant-propos

## Introduction

Ce travail de thèse est consacré à un sujet essentiel pour les observations astronomiques faites au sol; il s'agit de la caractérisation et de la spécification des conditions atmosphériques qui permettent d'utiliser au mieux les interféromètres et les systèmes d'optique adaptative.

La qualité d'observations astronomiques au sol est limitée par la turbulence atmosphérique. Mais ces observations restent compétitives par rapport aux observations depuis l'espace grâce à l'optique adaptative. Celle-ci permet en effet de corriger les fluctuations de phase atmosphériques suffisamment, pour que les plus grands télescopes actuels – avec des diamètres de miroirs compris entre 8 et 10 m – soient limités par la seule diffraction. En principe l'optique adaptative peut également compenser les fluctuations des différences de phase entre les pupilles d'entrée d'un interféromètre. Mais aujourd'hui cette correction est tout juste possible parce que les vitesses de compensation sont encore insuffisantes. De fait, les systèmes correcteurs actuels, comme par exemple FINITO à l'observatoire de Paranal au Chili, ne fonctionnent correctement que pour l'observation de quelques étoiles brillantes.

En règle générale, les temps d'exposition utilisés lors d'observations interférométriques doivent donc être suffisamment courts pour immobiliser les mouvements de la turbulence. Le prix en est une perte considérable en sensibilité. Si l'on découvrait des sites où la turbulence est plus lente, les systèmes de correction seraient alors assez rapides pour suivre la turbulence et la sensibilité des interféromètres en serait considérablement améliorée.

La turbulence atmosphérique est caractérisée par plusieurs paramètres, parmi lesquels: le paramètre de Fried,  $r_0$ , le temps de cohérence,  $\tau_0$ , l'échelle externe,  $L_0$ , l'angle isoplanétique,  $\theta_0$ . Les deux premiers paramètres:  $r_0$  et  $\tau_0$ , sont au centre de mon travail de thèse, et j'en donne donc une rapide définition:

- Le paramètre de Fried,  $r_0$ , est égal au diamètre d'un miroir pour lequel les pertes en résolution dues à la diffraction et aux turbulences atmosphériques sont tout juste égales. Une grande valeur du paramètre de Fried implique une grande taille des cellules de turbulence et présente ainsi un avantage direct pour la performance des systèmes d'optique adaptative.
- Un deuxième paramètre essentiel de la turbulence est le temps de cohérence,  $\tau_0$ . Il est défini de telle manière qu'en un lieu donné, au bout du temps de cohérence, la variance des fluctuations temporelles de phase dues à la turbulence soit égale à  $1 \text{ rad}^2$ . Le temps de cohérence détermine notamment la sensibilité des interféromètres.

Ces deux paramètres varient d'un site à l'autre, mais à la différence de  $r_0$ , le temps de cohérence dépend également de la vitesse de la turbulence. Et comme il n'existe actuellement aucune méthode adaptée pour mesurer le temps de cohérence avec un petit télescope, les campagnes de sélection et de monitoring s'appuient principalement sur la mesure du paramètre de Fried. En pratique, on se réfère plutôt au seeing,  $\varepsilon_0$ , qu'au paramètre de Fried, mais ces deux quantités sont en fait équivalentes: le seeing est égal à la résolution angulaire d'un télescope avec un miroir de diamètre  $r_0$ .

## Un nouvel instrument FADE

Au cours de mon travail de thèse, nous avons proposé une méthode pour mesurer le temps de cohérence. Elle consiste à défocaliser l'image d'une étoile et à en faire – grâce à une obstruction centrale sur le miroir primaire – un anneau diffus. Une lentille avec une aberration sphérique est alors placée sur le trajet du faisceau, la combinaison d'une défocalisation et de l'aberration sphérique étant choisie de façon à s'apparenter au mieux à une aberration conique: l'anneau diffus est ainsi focalisé sur un anneau fin. De fait, notre méthode est la fille isotrope du *Differential Image Motion Monitor*, DIMM, l'instrument de référence pour la mesure du seeing.

La turbulence atmosphérique déforme l'image; ces déformations peuvent être convenablement mesurées parce qu'au premier ordre elles se traduisent par des changements de rayons de l'anneau. L'avantage de cette méthode est notamment son insensibilité aux aberrations de *tip* et *tilt* qui sont causées en partie par la turbulence mais aussi par les vibrations de télescope, et qui n'intéressent donc pas la turbulence seule. Au lieu du *tip* et *tilt*, nous mesurons le coefficient de défocalisation qui est à l'origine des variations du rayon. Une relation entre les fluctuations temporelles du rayon et le temps de cohérence a été établie dans le cadre du modèle de Kolmogorov de la turbulence atmosphérique.<sup>1</sup>

Des premières mesures avec ce *Fast Defocus Monitor*, FADE, ont été obtenues à l'observatoire de Cerro Tololo au Chili, du 29 Octobre au 2 Novembre 2006. L'instrument comportait un télescope de 0.35 m de diamètre et une caméra à lecture rapide; nous avons enregistré des images d'anneaux pendant cinq nuits en faisant varier les paramètres instrumentaux. L'analyse de ces mesures et de leurs incertitudes est présentée dans le manuscrit. Il nous a fallu faire particulièrement attention aux aberrations optiques du télescope et aux taches de scintillation causées par la turbulence dans la haute atmosphère. Ces deux effets pouvant modifier le rayon de l'anneau, nous avons établis des critères de rejet des images trop déformées.

Le seeing et le temps de cohérence estimés avec FADE ont été comparés aux résultats obtenus par les instruments de référence que sont DIMM et le *Multi Aperture Scintillation Sensor*, MASS. A Cerro Tololo, MASS et DIMM sont installés derrière un même télescope, sur une tour de 6 m à 10 m du dôme dans lequel se trouvait FADE. Les résultats ne sont pas identiques parce que MASS et DIMM observaient des étoiles moins brillantes que FADE, et sondaient donc une partie différente de l'atmosphère. Statistiquement, sur l'ensemble des 5 nuits, FADE a tendance à sous-estimer le seeing. Nous avons pu reproduire cet effet avec des simulations d'anneaux diffus. Et nous pensons donc que cette sous-estimation est due – sur cet instrument prototype – à ce que la combinaison de

---

<sup>1</sup>On préfère souvent caractériser la turbulence en utilisant le modèle de Van Karman, qui est essentiellement équivalent au modèle de Kolmogorov à ceci près qu'il prend en compte l'effet de l'échelle externe. Or l'échelle externe n'a pas d'effet sur les fluctuations rapides qui déterminent le temps de cohérence, et nous nous sommes donc placés dans le cadre plus simple du modèle de Kolmogorov.

défocalisation et d'aberrations sphérique n'était pas optimisée et ne s'apparentait pas bien à une aberration conique.

En ce qui concerne les temps de cohérence, les estimations obtenues avec MASS se basent sur des mesures de scintillation. La turbulence en dessous de 500 m d'altitude n'engendrant pas de scintillation, la méthode n'est pas sensible à la turbulence basse – contrairement à DIMM et FADE. Par conséquent MASS n'a pas pu nous servir d'instrument de référence pour nos mesures. Et c'est pourquoi nous organisons actuellement une deuxième campagne de mesures qui aura lieu en Août 2007 à l'observatoire de Paranal. Ces observations se feront simultanément avec le système d'optique adaptative NAOS qui est installé derrière un des *Very Large Telescopes*, VLT, et qui fournit des mesures fiables du temps de cohérence.

A terme, l'objectif est d'utiliser FADE lors des campagnes de caractérisations de sites. En particulier, des mesures sont prévues à Dôme C en Antarctique; un site potentiel pour les futures générations de grands télescopes et d'interféromètres.

Mais l'étude de la turbulence n'est pas une fin en soi et je complète donc le manuscrit en donnant un exemple d'un travail de recherche rendu possible grâce à la maîtrise des effets de la turbulence.

## Observations du système triple $\delta$ Velorum

Comme il a été souligné plus haut, aujourd'hui les interféromètres sont limités à l'observation des sources les plus brillantes à cause de la rapidité des turbulences atmosphériques. Mais pourtant, même dans ces conditions, l'interférométrie reste une technique clef pour beaucoup d'observations, parmi lesquelles l'observation de systèmes d'étoiles multiples. L'état, l'évolution et l'origine de ces systèmes ne pourront être compris que si les études dynamiques sont confrontées aux résultats d'observations à haute résolution angulaire.  $\delta$  Velorum donne un exemple d'une avancée récente due à des observations interférométriques.

En 2000,  $\delta$  Velorum était encore considéré comme un système de quatre étoiles et il servait d'étoile de référence au système d'autoguidage du satellite Galilée. Il fut la cause d'une véritable frayeur des ingénieurs qui suivaient le satellite, lorsque la sonde signala une baisse brusque d'intensité. Les ingénieurs crurent à une panne du système de guidage, mais Galilée avait en fait été témoin d'une éclipse.

Ainsi, au début de ma thèse  $\delta$  Velorum avait acquis le rang de système quintuple. Nous voulions saisir la chance de mesurer les paramètres d'un tel système: cinq étoiles du même âge mais avec des masses différentes.  $\delta$  Velorum pouvait devenir un système clef pour tester des modèles d'évolutions stellaires. J'ai analysé dans cet objectif les observations de  $\delta$  Velorum obtenues avec le *VLT Interferometer Commissioning Instrument*, VINCI, qui est installé à l'observatoire de Paranal.

Les résultats des observations avec VINCI nous ont surpris parce que les deux étoiles éclipsantes semblent avoir des diamètres deux à trois fois plus grands que ceux attendus pour des étoiles de la séquence principale et parce qu'elles se trouvent donc probablement dans des stades avancés de leur évolution. Mais nous avons été tout autant surpris quand, en analysant des données photométriques et spectroscopiques existantes, nous avons réalisé que deux des cinq étoiles ne font en fait pas partie du système. Ainsi  $\delta$  Velorum a gagné en intérêt à cause des propriétés inattendues des deux étoiles éclipsantes, mais en même temps il est retombé au rang de système triple. Ce travail est décrit dans le dernier chapitre du manuscrit.



# Contents

|  |    |
|--|----|
| Avant-propos   | 5  |
| 1 Introduction: Our screen towards the Universe, the turbulent atmosphere                                  | 13 |
| 1.1 Looking through the screen   | 13 |
| 1.2 Characterizing the screen  | 14 |
| 1.2.1 The notion of turbulence   | 14 |
| 1.2.2 Is there a theory of turbulence?   | 15 |
| 1.2.3 Parameters for the viewing condition and their dependence on turbulence                              | 16 |
| 1.2.4 Statistical description of atmospheric turbulence  | 18 |
| 1.2.5 Coherence-time measurements  | 20 |
| 1.3 Constituents of this thesis  | 21 |
| 1.3.1 Assessing time scales of turbulence at Dome C, Antarctica  | 21 |
| 1.3.2 A new instrument to measure the coherence time   | 23 |
| 1.3.3 Astrophysical application: interferometric observations of $\delta$ Velorum                          | 24 |
| 2 A method of estimating time scales of atmospheric piston and its application at Dome C (Antarctica)      | 27 |
| 2.1 Introduction   | 28 |
| 2.2 Measurements   | 28 |
| 2.2.1 Observational setup  | 28 |
| 2.2.2 Data description   | 29 |
| 2.3 Quantifying the motion of the fringe pattern and the Airy discs  | 31 |
| 2.4 Coherence time   | 33 |
| 2.4.1 Estimating coherence time through Fourier analysis   | 33 |
| 2.4.2 Estimating coherence time through the evolution of correlation                                       | 34 |
| 2.4.3 Optimal setup for coherence time measurements  | 36 |
| 2.5 Conclusion   | 36 |
| 3 A method of estimating time scales of atmospheric piston and its application at Dome C (Antarctica) – II | 39 |
| 3.1 Introduction   | 40 |
| 3.2 Formalism  | 41 |
| 3.3 Measurements at Paranal  | 43 |

|       |  |    |
|-------|--|----|
| 3.3.1 | Observational set-up . . . . .   | 43 |
| 3.3.2 | Derivation of atmospheric parameters . . . . .   | 44 |
| 3.3.3 | Performance of the piston scope . . . . .  | 45 |
| 3.4   | Measurements at Dome C . . . . .   | 48 |
| 3.5   | Conclusions . . . . .  | 51 |
| 4     | Atmospheric coherence times in interferometry: definition and measurement . . . . .    | 53 |
| 4.1   | Introduction . . . . .   | 54 |
| 4.2   | Atmospheric coherence time in interferometry . . . . .                                 | 54 |
| 4.2.1 | Atmospheric coherence time $\tau_0$ . . . . .  | 54 |
| 4.2.2 | Piston time constant . . . . .   | 56 |
| 4.2.3 | Piston power spectrum and structure function . . . . .                                 | 57 |
| 4.2.4 | Error of a fringe tracking servo . . . . .   | 58 |
| 4.2.5 | Summary of definitions and discussion . . . . .  | 59 |
| 4.3   | Measuring the atmospheric time constant . . . . .                                      | 60 |
| 4.3.1 | Existing methods of $\tau_0$ measurement . . . . .                                     | 60 |
| 4.3.2 | The new method: FADE . . . . .   | 61 |
| 4.4   | Conclusions . . . . .  | 64 |
| 4.5   | Appendix A - Derivation of the piston structure function . . . . .                     | 65 |
| 4.6   | Appendix B - Fast focus variation . . . . .  | 67 |
| 5     | FADE, an instrument to measure the atmospheric coherence time . . . . .                | 69 |
| 5.1   | Introduction . . . . .   | 70 |
| 5.2   | The instrument . . . . .   | 71 |
| 5.2.1 | Operational principle . . . . .  | 71 |
| 5.2.2 | Hardware . . . . .   | 72 |
| 5.2.3 | Optics . . . . .   | 72 |
| 5.2.4 | Acquisition software . . . . .   | 73 |
| 5.2.5 | Observations . . . . .   | 74 |
| 5.3   | Data analysis . . . . .  | 74 |
| 5.3.1 | Estimating the ring radius . . . . .   | 74 |
| 5.3.2 | Noise and limiting stellar magnitude . . . . .   | 76 |
| 5.3.3 | The response coefficient of FADE . . . . .   | 77 |
| 5.3.4 | Derivation of the seeing and coherence time . . . . .                                  | 78 |
| 5.4   | Analysis of observations . . . . .   | 80 |
| 5.4.1 | Influence of instrumental parameters . . . . .   | 80 |
| 5.4.2 | Comparison with MASS and DIMM . . . . .  | 82 |
| 5.5   | Conclusions and perspectives . . . . .   | 83 |
| 5.6   | Appendix A – Estimator of the ring radius and center . . . . .                         | 84 |
| 5.7   | Appendix B – Structure function of atmospheric defocus . . . . .                       | 85 |
| 5.8   | Appendix C – Simulations . . . . .   | 86 |
| 5.8.1 | Simulation tool . . . . .  | 86 |
| 6     | Interferometric observations of the multiple stellar system $\delta$ Velorum . . . . . | 93 |
| 6.1   | Introductory remarks to the article . . . . .  | 93 |
| 6.2   | Introduction . . . . .   | 97 |

|       |  |     |
|-------|--|-----|
| 6.3   | Characteristics of $\delta$ Vel A derived from previous measurements . | 98  |
| 6.3.1 | Orbit orientation and eccentricity . . . . .                           | 98  |
| 6.3.2 | Semi-major axis and stellar parameters . . . . .                       | 100 |
| 6.4   | VLT Interferometer/VINCI observations . . . . .                        | 101 |
| 6.4.1 | Data description . . . . .   | 101 |
| 6.4.2 | Comparison to a model . . . . .  | 102 |
| 6.5   | Results and discussion . . . . .                                       | 104 |
| 6.5.1 | The close eclipsing binary $\delta$ Vel (Aa-Ab) . . . . .              | 104 |
| 6.5.2 | The physical association of $\delta$ Vel C and D . . . . .             | 105 |
| 6.6   | Summary . . . . .  | 105 |
| 7     | Conclusion   | 107 |
|       | Bibliography   | 111 |
|       | Summary  | 115 |



# Chapter 1

## Introduction: Our screen towards the Universe, the turbulent atmosphere

Life on earth and its evolution have become possible because of the radiation shield, i.e. the atmosphere layer with a mass equivalent to about 10 m of water. While it is a precondition for existence, it complicates life for the astronomer and astrophysicist, who desires an unfiltered view of the universe. Looking through the screen in order to find those locations on the planet where the view is least obstructed is, thus, an important task. It is also the major issue of the research outlined in this thesis.

### 1.1 Looking through the screen

It is doubtlessly a tribute to the astronomers and engineers that they have developed instruments precise enough to detect earth-like planets several light years removed. An example of current interest are the lately discovered companions of the 20 light-years distant *Gliese 581* [9]. Their detection was, of course, indirect: temporal line-shifts on the spectrum of the star, corresponding to velocity variations of only 2 to 3 meters per second, were used to infer the presence of a planet about 5 times the mass of Earth. To resolve the planet against its central star, i.e. to obtain a separate point image (1 pixel) at optical wavelengths, a telescope with mirror diameter of at least 15 m would be required. To obtain more than a point image a truly gigantic mirror, far beyond technical feasibility would be required. While a point image will probably be achieved with the next generation of large telescopes, the system could already be resolved by combining the light collected by several telescopes, that is by interferometry – provided the distortion by atmospheric fluctuations could be overcome. At present the angular resolution and contrast of single-dish telescopes, as well as the sensitivity of interferometers, are limited by atmospheric turbulence and the planets of *Gliese 581* can, therefore, not yet be resolved.

Still, ground based observations will remain competitive to observations from space, because adaptive optics can, by now, correct the wave-front phase fluctuations sufficiently to let the resolution of the currently largest telescopes – with mirrors of 8-10 m diameter – attain the limit set by optical diffraction. Adaptive optics can likewise compensate for the fluctuation of the phase differences between individual beams of interferometers. However, with current technologies, the task remains difficult, because the correction is not sufficiently fast. Even at prime observation sites, such as Paranal, Chile, exposure times are, therefore, employed that are short enough to immobilize the atmospheric turbulence. The price is a significant loss of sensitivity for interferometric observations. If sites were to be found with substantially slower turbulence, available phasing devices might be fast enough to follow the phase fluctuations, and exposure times could then be substantially increased.

## 1.2 Characterizing the screen

### 1.2.1 The notion of turbulence

But what is turbulence? Amazingly no simple definition can be given, even though earthbound astronomy as well as everyday life are permanently confronted with it. A look out of the window shows leaves whirling in the wind and smoke curling over the roofs. Driving to work this morning one was an atom of a turbulent circulation, or – if the highway was free – has created a track of turbulent air flow.

What is common to all such processes? A first predominant element – and not just, as the name might suggest, of gaseous turbulence – is chaos; i.e. the evolution of turbulence depends erratically on initial conditions.

But even three or four particles can evolve chaotically, i.e. with an extreme sensitiveness to the initial conditions, and this does not make for turbulence yet. Thus, a second requirement is, indeed, the random involvement of a large number of particles.

Imagine a company of soldiers led daily by another commander who chooses the route of the parade. The path that is followed depends on the whim of the leader, yet a company of properly disciplined soldiers will not accept to be termed turbulent. A third requirement is, thus, that there must be random motion over a continuous and broad range in time and in space.

Clearly, this is a modest and incomplete attempt to characterize turbulence, but the reader who desires a more rigorous definition may turn to Davidson's monograph "Turbulence" [18].

### 1.2.2 Is there a theory of turbulence?

Turbulence is in general merely a nuisance phenomenon. Where it becomes critical, however, for example in aerodynamics, thermodynamics or meteorology it needs to be studied and it is found to be complex and quite diverse. A pilot may be well informed about turbulence in aerodynamics, yet he would be confused, when the meteorologist were to add to the weather forecast his analysis of atmospheric turbulence. Likewise an astrophysicist might approach his colleague from the thermodynamics department and give him mass, temperature and size of a star of particular interest whose spectral image he would like to understand. He, too, might be confounded by a host of information in the answer, that is difficult to relate to his problem and by the great number of associated caveats.

To simplify matters, one would wish to have a theory that predicts large-scale movements in turbulent flows, and that indicates the energy distribution over different spatial scales. Ideally, it should be applicable to a broad range of phenomena, from gas flows in galaxies to currents in the oceans. But presently there are as many theories as there are problems.

Yet astronomers are fortunate: where they wish to characterize atmospheric turbulence, they profit from one of the exceptional success stories in turbulence physics. It is due to the Russian mathematician Andrei N. Kolmogorov who studied turbulent flows from air jets and published his results in 1931 [43]. As his point of departure, Kolmogorov used Richardson's assumption that – in a turbulent medium – the energy is continually transferred from large-scale to small-scale structures, where it is eventually dissipated by viscosity [56]; he then assumed an isotropic medium in equilibrium and deduced the law:

$$E(f, \epsilon) = \alpha \epsilon^{2/3} f^{-5/3} \quad (1.1)$$

where  $f$  is the norm of the three-dimensional spatial-frequency vector  $\mathbf{f}$ , and  $E(f, \epsilon) \mathrm{d}f$  equals the energy contained in vortices with spatial frequencies between  $f$  and  $f + \mathrm{d}f$ , in a fluid characterized by its rate,  $\epsilon$ , of viscous dissipation. The Kolmogorov constant,  $\alpha$ , is a function of the Reynolds number,  $R = LV/\nu$ , where  $L$  and  $V$  are the characteristic size and speed of the turbulent flow, while  $\nu$  is the viscosity of the fluid. The viscosity of air is  $15 \cdot 10^{-6} \text{m}^2 \text{s}^{-1}$ ; taking  $L = 15 \text{m/s}$  and  $V = 1 \text{m/s}$  leads to  $R = 10^6$  which corresponds to fully developed turbulence. Landau and Lifshitz [45] have shown that  $\alpha \sim 1.52$ , at such high Reynolds numbers.

This law, which predicts the energy distribution over spatial scales, rests entirely on the hypothesis of a continuous dissipation of kinetic energy from large to small scales. Even though it is heuristic and not strictly proven, the law is in excellent agreement with observations, within the *inertial range*  $1/L_0 \ll f \ll 1/l_0$ . Here  $L_0$  denotes the size of the largest vortices, which – for

our atmosphere – may vary between roughly 10 m and 100 m. While  $l_0$  – the scale, below which the energy is predominantly dissipated by viscous friction – ranges from a few millimeters to about 1 cm.

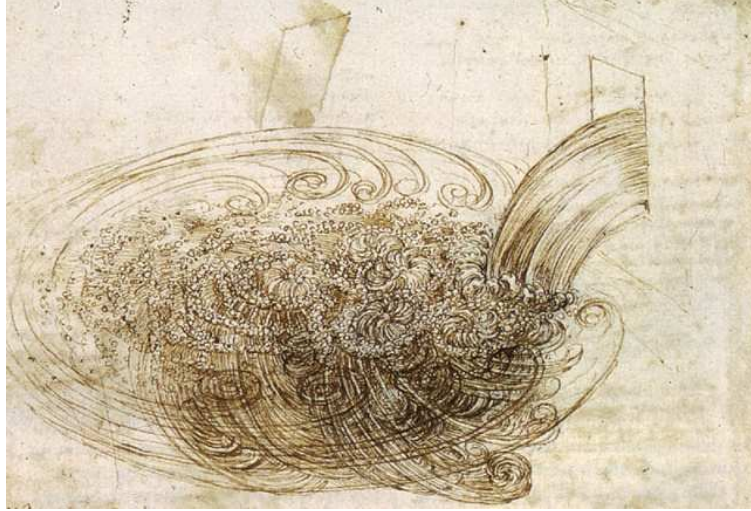


Figure 1.1: A turbulent cascade as seen by Leonardo da Vinci. Reproduced from [19].

### 1.2.3 Parameters for the viewing condition and their dependence on turbulence

The viewing conditions at an observatory site relate to two major aspects. The first aspect is the resolution attainable with long exposures and a telescope of given mirror diameter,  $D$ . For small telescopes the angular resolution is entirely limited by diffraction:

$$\varepsilon = 0.976 \lambda/D \quad (1.2)$$

For a 0.1 m-telescope, the angular resolution at wavelength  $\lambda = 0.5 \mu\text{m}$  equals  $4.9 \cdot 10^{-6}$  rad, i.e. 1".

With increasing mirror sizes the resolution tends to be increasingly affected by the wavefront distortions due to atmospheric turbulence. To characterize the magnitude of this influence, it is convenient to refer to the mirror diameter where the effect of diffraction becomes just equal to the degradation of resolution due to the atmosphere. This diameter is termed *Fried parameter*,  $r_0$ , where the somewhat uncommon use of the letter  $r$  for a diameter needs to be noted. Under poor conditions – for example even during clear nights at sea level – the Fried parameter may rarely be better than about 1 cm. Under optimum conditions, such as on clear nights at Paranal, Chile, the value may go up to 1 m for wavelengths between 0.5 to  $1 \mu\text{m}$ . Large telescope mirrors can then profitably be used, and they will attain excellent resolution, when adaptive optics are being used that correct for phase differences by acting on individual mirror segments.

In practice one tends to refer to the *seeing*,  $\varepsilon_0$ , rather than the Fried parameter,  $r_0$ , but the two quantities are essentially equivalent, the seeing being the angular resolution of a telescope with mirror diameter  $r_0$ :

$$\varepsilon_0 = 0.976 \lambda / r_0 \quad (1.3)$$

Thus, the Fried parameters 1 cm and 1 m correspond, at the wavelength  $0.5 \mu\text{m}$ , to seeing values of  $10''$  and  $0.1''$ .

If the exposure time is shorter than the characteristic time of turbulent motions, say below 5 ms, the image of a star consists of individual *speckles* inside the spot formed by the long-exposure image. Speckles result from the interference between those parts of the wavefront where the turbulence-induced wavefront-inclinations are the same; and these small interference patterns contain information at angular resolutions up to the diffraction limit. Accordingly, the angular resolution of large telescopes approaches the diffraction limit with decreasing exposure times – the price being a considerable loss in sensitivity.

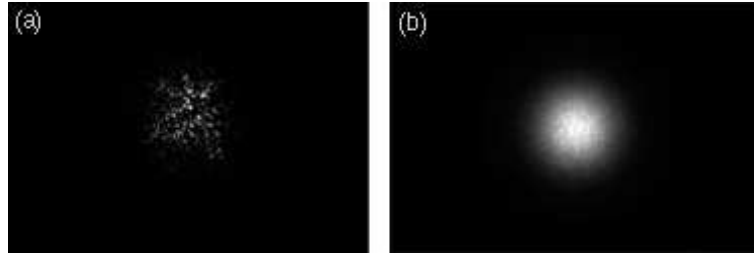


Figure 1.2: Two images of a star through a telescope with a mirror diameter,  $D$ , substantially larger than the Fried parameter,  $r_0$ . (a) If the exposure image is shorter than the coherence time of turbulence,  $\tau_0$ , the angular size of the smallest image-details is set by the diffraction on the telescope mirror:  $\varepsilon = 0.976 \lambda / D$ . (b) After a much longer exposure time, the superposition of many speckles gives the image its more uniform aspect. The angular size of the spot then equals the seeing:  $\varepsilon_0 = 0.976 \lambda / r_0$ . Reproduced from [47].

The stability of such short-exposure images is a second aspect of the goodness of viewing conditions. The parameter that is being used to characterize the stability is the *coherence time*,  $\tau_0$ . It equals the time interval over which the rms-phase distortion at a point due to turbulence is 1 radian. This is equivalent to stating that the coherence time equals 0.314 times the ratio of the Fried parameter to the mean velocity of the turbulent medium. Hence, for a single turbulent layer with velocity 50 m/s and a Fried parameter 0.5 m, the coherence time is 3.14 ms.

In summary, for a mirror of diameter  $r_0$  and an exposure time  $\tau_0$ , the effects due to diffraction, finite mirror diameter, and finite exposure time are just equal.

### 1.2.4 Statistical description of atmospheric turbulence

In his extensive analysis of the statistical properties of atmospheric turbulence, Roddier [58] examined the implications of Kolmogorov's law for the propagation of optical wavefronts. Some of the results that are used in the subsequent chapters can be summarized as follows.

The turbulent mixing of the air creates inhomogeneities of temperature,  $T$ , which likewise follow Kolmogorov's law:

$$W_T(f) \propto f^{-5/3} \quad (1.4)$$

$W_T(f) = |\tilde{T}(f)|^2$  is the power spectrum of temperature fluctuations, where the symbol:  $\tilde{\cdot}$  denotes the Fourier transform. In an isotropic medium, the three-dimensional power spectrum  $W_T(\mathbf{f}) = W_T(f_x, f_y, f_z)$  is related to the one-dimensional power spectrum through an integration over two directions:

$$W_T(f) = 4\pi f^2 W_T(\mathbf{f}) \quad (1.5)$$

Thus,

$$W_T(\mathbf{f}) \propto f^{-11/3} \quad (1.6)$$

The refractive index of air,  $n$ , is a function not only of the temperature but also of the humidity. However at visible and near infrared wavelengths,  $n$  proves to be largely insensitive to water vapor concentration; its fluctuations follow therefore the same law as the temperature fluctuations:

$$W_n(\mathbf{f}) = 3.9 \cdot 10^{-5} C_n^2 f^{-11/3} \quad (1.7)$$

The *index structure constant*,  $C_n^2$ , is related to the local gradient of the optical index. It determines the contribution of the turbulence in the specified air layer to optical propagation and typically it varies between  $10^{-15} \text{ m}^{-2/3}$  and  $10^{-13} \text{ m}^{-2/3}$ .

Fluctuations of the wavefront phase,  $\varphi$ , are due to the fluctuations of the optical index. In the case of many thin turbulent layers – contributing each only a small phase change:  $d\varphi \ll 1 \text{ rad}$  – the spectrum of phase fluctuations is, accordingly:

$$W_\varphi(\mathbf{f}) = 9.7 \cdot 10^{-3} k^2 f^{-11/3} \int_0^{h_{\max}} C_n(h)^2 dh \quad (1.8)$$

$k = 2\pi/\lambda$  is the spectral wave number, and  $h$  denotes the altitude of a turbulent layer with thickness  $dh$ . This spectrum applies within the inertial range  $1/L_0 \ll f \ll 1/l_0$ .

So much for the results of Roddier's analysis. We conclude that, with regard to the propagation of visible light through the atmosphere, three essential parameters are:  $C_n^2$ ,  $l_0$  and  $L_0$ . A fourth parameter is the mean velocity,  $\bar{V}$ , of the turbulent medium. Together these parameters determine the Fried parameter (or the seeing) and the coherence time:

- The Fried parameter,  $r_0$ , is an integral over the structure index constant,  $C_n^2$ :

$$r_0 = [ 0.423 k^2 \cos(\gamma)^{-1} \int_0^{h_{\max}} C_n(h)^2 dh ]^{-3/5} \quad (1.9)$$

where  $\gamma$  is the zenith-angle. The viewing conditions are optimized, when observations are directed at the zenith; for lower angles the Fried parameter decreases.

- The coherence time is a combination of the Fried parameter and of an averaged wind speed,  $\bar{V}_{5/3}$  (see Chapter 4):

$$\tau_0 = 0.314 r_0 / \bar{V}_{5/3} \quad (1.10)$$

$$\bar{V}_p = \left[ \frac{\int_0^{h_{\max}} V(h)^p C_n(h)^2 dh}{\int_0^{h_{\max}} C_n(h)^2 dh} \right]^{1/p} \quad (1.11)$$

This definition is based on the assumption that independent layers at different heights,  $h$ , contribute to the turbulence, and that – in each layer – the turbulence as a whole is being displaced horizontally with velocity  $V(h)$ .<sup>1</sup>

Both parameters, the seeing,  $\varepsilon_0$ , and the coherence time,  $\tau_0$ , are site dependent. But there is a difference: the coherence time depends also on wind speed, and there is currently no adequate technique to measure the coherence time. For this reason, site testing and monitoring campaigns are currently restricted to the assessment of the seeing.

---

<sup>1</sup>Turbulence arises predominantly at the interface of cold and warm layers that move in different directions. The resulting shear layer is displaced along the layers' interface in good agreement with Taylor's hypothesis which assumes *frozen flows*: "If the velocity of the air stream which carries the eddies is very much greater than the turbulent velocity, one may assume that the sequence of changes at a fixed point are simply due to the passage of an unchanging pattern of turbulent motion over that point" [66]. But is this hypothesis adequate in spite of the fact that there are – relative to the overall motion of the layer – motions of the vortices and eddies? Most astronomers are familiar with the aspect of turbulent patterns that are formed over a telescope-mirror, because these patterns are readily observed on defocused stellar images: Generally, the pattern translates, indeed, with a common global motion, yet each individual, turbulent cell evolves and moves during the time it crosses the telescope aperture. This suggests that the turbulent motion is a combination of a frozen-flow and a dispersive motion and Taylor's hypothesis is, accordingly, an approximation. In fact, it has been shown that his *frozen-flow hypothesis* describes the turbulent motions up to time intervals 20 to 30 milliseconds, i.e. typically a few coherence-times (Gendron & Léna [24] and Schoeck & Spillar [62]).

### 1.2.5 Coherence-time measurements

Because it determines the sensitivity of interferometers and the performance of adaptive optic systems, the atmospheric coherence time,  $\tau_0$ , is a parameter of major importance. Several instruments measure  $\tau_0$  or related parameters, but all current methods have limitations: either the instrument is not well suited for site monitoring, or the method is burdened by intrinsic uncertainties and biases.

- SCIDAR (Scintillation Detection And Ranging) has provided good results on  $\tau_0$ , but it requires large telescopes and is not suitable for monitoring, since it necessitates manual data processing (Fuchs et al. [22]).
- Balloons provide only single-shot profiles of low statistical significance (Azouit & Vernin [8]).
- Adaptive-optic systems and interferometers give good results, but are suitable neither for testing projected sites nor for long-term monitoring (Fusco et al. [23]).

The four subsequent methods all use small telescopes and can, thus, be used for site-testing. They all have their special attractions. However, with regard to the coherence time each has intrinsic problems:

- SSS (Single Star SCIDAR) in essence extends the SCIDAR technique to small telescopes: profiles of  $C_n(h)^2$  and  $V(h)$  are obtained with less altitude resolution than with SCIDAR, and are then used to derive the coherence time (Habib et al. [29]).
- The GSM (Generalized Seeing Monitor) measures velocities of prominent atmospheric layers. By refined data processing, a coherence time,  $\tau_{AA}$  – but one with a different dependence on the turbulence profile than  $\tau_0$  – is deduced from the angle-of-arrival fluctuations (Ziad et al [73]).
- MASS (Multi-Aperture Scintillation Sensor) is a recent, but already well proven, turbulence monitor. One of the measured quantities, related to scintillation in a 2 cm-aperture, approximates the coherence time, but this averaging does not include low-altitude layers and thus gives a biased estimate of  $\tau_0$  (Kornilov et al. [44]).
- DIMM (Differential Image Motion Monitor) is not actually meant to determine  $\tau_0$ , but an estimation of the coherence time can nevertheless be obtained by combining the measured  $r_0$  with meteorological wind-speed data (Sarazin & Tokovinin [59]).

We conclude from this brief survey, that there is, at this point, no sufficiently simple technique to measure  $\tau_0$  with a small telescope.

## 1.3 Constituents of this thesis

### 1.3.1 Assessing time scales of turbulence at Dome C, Antarctica

Dome C is a 3235 m high summit ( $75^{\circ}06' \text{ S}$ ,  $123^{\circ}23' \text{ E}$ ) on the Antarctic plateau. Because of its elevation, the location does not experience the winds that are typical for the coastal regions of Antarctica. This has led to the assumption, that the atmospheric conditions might be particularly advantageous. In 2005, *Concordia*, a French-Italian station opened on Dome C, for research in astronomy, glaciology, earth-science, etc. Aristidi et al. [5] and Lawrence et al. [46] determined the size of the turbulent cells, as measured 30 m above ground, to be 2 to 3 times larger than at the best mid-latitude sites. The latter authors concluded, that an interferometer built on Dome C could potentially work on projects that would otherwise require a space mission. This is a clear possibility, but it needs to be confirmed by measurements of the coherence time.

**Chapter 2** presents an analysis of the first interferometric fringes recorded at Dome C, Antarctica. Measurements were taken between January 31<sup>st</sup> and February 2<sup>nd</sup> 2005 at daytime. The instrumental set-up, termed *Pistonscope*, aims at measuring temporal fluctuations of the atmospheric piston, which are critical for interferometers and determine their sensitivity. The characteristic time scales are derived through the motion of the image that is formed in the focal plane of a Fizeau interferometer. Although the coherence time of piston could not be determined directly – due to insufficient temporal and spatial sampling – a lower limit was, nevertheless, determined by studying the decay rate of correlation between successive fringes. Coherence times in excess of 10 ms were determined in the analysis, i.e. at least three times higher than the median coherence time measured at the site of Paranal (3.3 ms).

To test the validity of the results derived in terms of the pistonscope, measurements with this instrument have subsequently been obtained at the observatory of Paranal, Chile, in April 2006 with high temporal and spatial resolution. In **Chapter 3** the observations are analyzed, and it is found that the resulting atmospheric parameters are consistent with the data from the astronomical site monitor, if the Taylor hypothesis of “frozen flow” is invoked with a single turbulent layer, i.e. if the atmospheric turbulence is taken to be displaced along a single direction. This has permitted a reassessment of our preliminary measurements – recorded with lower temporal and spatial resolution – at the Antarctic site of Dome C, and it was seen that the calibration in terms of the new data sharpened the conclusions of the first qualitative examination in Chapter 2.

As seen in Chapters 2 and 3, we have, in spite of the current limitations in methodology and instrumentation, been able to infer considerably increased coherence times at Dome C, Antarctica, which is consistent with the earlier extensive determinations of other parameters that demonstrate the superior con-

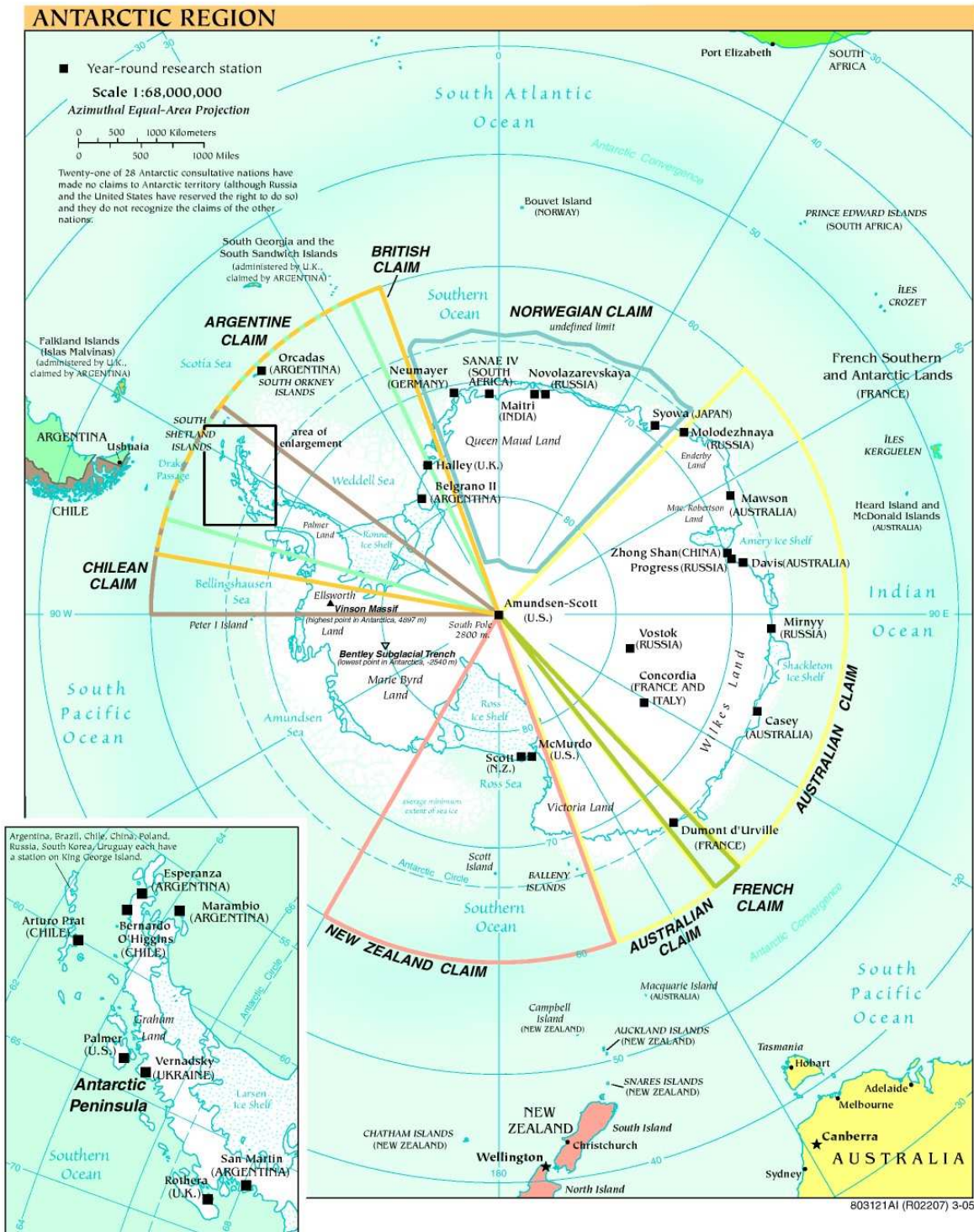


Figure 1.3: Political map of Antarctica and year-round research stations (2005). Reproduced from [13].

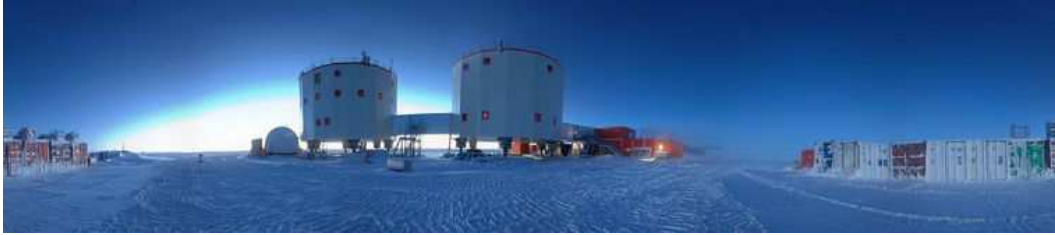


Figure 1.4: Panoramic view of the *Concordia* station at Dome C. Reproduced from [70].

dition for astronomical observations at this site (Agabi et al. [2] and Lawrence et al.[46]). The two chapters make it equally clear, however, that a major effort was required for this limited achievement, and that – even with more extensive sampling – the reliability and accuracy of the measured coherence times could not be fully satisfactory because of the influence of the uncertain angle between the instrumental set-up and the wind direction. The temporal variations of the fringe pattern become faster, as the angle between the wind direction and the interferometric axis diminishes. To derive – without continuous assessment of changing wind directions – meaningful values of  $\tau_0$ , a parameter must, therefore, be measured that is independent of the wind direction. To make routine monitoring possible, the measurement would also have to be comparatively simple. The challenge to find such a parameter and to develop an instrument that permits its fast and reliable determination has, thus, become central to this thesis.

### 1.3.2 A new instrument to measure the coherence time

Since there exists currently no method to measure the coherence time directly and to achieve this with a compact instrument, Andrei Tokovinin and myself have sought a new approach to close the gap. A comparatively simple method has been adopted and an instrument has been designed to shift the image of a star somewhat out of focus, which converts it – due to a suitably enlarged central blind area of the telescope – to a ring. Insertion of a lens with proper spherical aberration sharpens this ring into a narrow circle. Atmospheric turbulence causes then distortions which can be conveniently assessed, because, to a first approximation, they appear as ring-radius changes.

The strength of the *Fast Defocus Monitor*, FADE, lies in the fact, that it is insensitive to *tip* and *tilt*, which – being jointly caused by telescope vibrations and atmospheric turbulence – can not be meaningful indicators of turbulence alone. Instead we measure the higher order aberration *defocus*, that causes the radius changes. A relation between the temporal properties of the radius variations and the coherence time has been developed in the framework of the Kolmogorov theory of turbulence.

**Chapter 4** deals with the consistency of the definition of  $\tau_0$ , since this is a precondition for the application of FADE. The interferometric coherence time

– that characterizes the time scale of the fringe motion in an interferometer – is analyzed and is found to have the same dependence on atmospheric parameters as the coherence time which is used in adaptive optics.

First measurements with FADE were obtained at Cerro Tololo, Chile, from October 29<sup>th</sup> to November 2<sup>nd</sup> 2006. The instrumental set-up is based on a telescope with mirror diameter 0.35 m and a fast CCD detector. Ring images were recorded during five nights with a broad range of instrument settings. The measurements and their uncertainties are analyzed in **Chapter 5**, and the seeing and coherence-time values obtained in terms of our instrument are compared with simultaneous measurements from the MASS and DIMM site-monitoring instruments.

### 1.3.3 Astrophysical application: interferometric observations of $\delta$ Velorum

**Chapter 6** presents an example of how research is facilitated, when the influence of the atmospheric fluctuations can be partly overcome. Interferometers have been introduced in astronomy to gain spatial resolution without the need to build extremely large telescopes. To resolve  $\delta$  Velorum in the infrared would require a telescope of about 100 m mirror diameter. In contrast, the *VLT Interferometer Commissioning Instrument*, VINCI, installed on Paranal in Chile, allows to resolve the bright, eclipsing binary Aa-Ab in  $\delta$  Velorum with two small 0.4 m siderostats 100 m apart.

Today, interferometric observations are limited to the brightest sources because of turbulence-related rapid motions of the image. In spite of this current limitation, interferometry proves to be a key technique in many astrophysical domains. The study of multiple star systems is an example: to understand the state, evolution and origin of such systems, the results of dynamical studies need to be compared to observations with high angular resolutions.

In 2000,  $\delta$  Velorum had become infamously famous among the engineers of the Galileo spacecraft;  $\delta$  Velorum was used as reference star for the guidance system, but at some point the system failed. While an instrumental defect was assumed at first, it turned out subsequently that the star, not the space probe, was at fault. Galileo had in fact witnessed an eclipse. Since then  $\delta$  Velorum had been classified as a quintuple stellar system and it promised to become a key system for testing stellar evolutionary models: five stars of same age and with different masses.

Three years ago, I began analyzing observations that had been obtained with the VINCI recombination instrument. The results were startling, because the diameters of the two eclipsing stars appear to be 2 to 3 times larger than expected for main sequence stars: the two stars are thus probably in a more advanced evolutionary state. In the continued analysis of existing photometric and spectroscopic data we found, that two of the five stars are, in fact, not part of the system. Thus,  $\delta$  Velorum has become more attractive due

to the unexpected properties of the eclipsing binary, while, at the same time, it relapsed to the status of a triple stellar system. This work is detailed in Chapter 6.



## Chapter 2

# A method of estimating time scales of atmospheric piston and its application at Dome C (Antarctica)

A. Kellerer, M. Sarazin, V. Coudé du Foresto, K. Agabi, E. Aristidi, T. Sadibekova, 2006, Applied Optics, 45, 5709-5715

### Abstract

This article presents the analysis of the first interferometric fringes recorded at Dome C, Antarctica. Measurements were done on January 31<sup>st</sup> and February 1<sup>st</sup> 2005 at daytime.

The aim of the analysis is to measure temporal fluctuations of the atmospheric piston, which are critical for interferometers and determine their sensitivity. These scales are derived through the motion of the image that is formed in the focal plane of a Fizeau interferometer.

We could establish a lower limit to the coherence time by studying the decay rate of correlation between successive fringes. Coherence times are measured to be larger than 10 ms, i.e. at least three times higher than the median coherence time measured at the site of Paranal (3.3 ms).

## 2.1 Introduction

While astronomical sites are usually selected mostly for the mild intensity of the atmospheric turbulence (large values of the Fried parameter  $r_0$ ), an equally important performance driver for ground based stellar interferometers is its temporal behavior. In passive arrays, a fast turbulence requires shorter exposure times to be frozen, thus reducing the sensitivity. In new generation active arrays (which include phase control through adaptive optics and fringe tracking), the optimum loop rate (for a given detection noise) is determined mostly by the coherence time  $t_0$  of the atmospheric phase fluctuations, or in a more complete way by their temporal spectral power density. In a low flux regime, a slower turbulence enables a lock of active systems on fainter sources, and therefore a higher sensitivity. For bright sources, a slower optimum loop rate results in lower phase residuals, which are critical in high dynamic range applications such as coronagraphy or interferometric nulling [1]. Even in a single-mode interferometer, where residual phase fluctuations across a single sub-pupil can be removed by proper spatial filtering (at the expense of a loss of photons), turbulence power remains in the form of the piston mode between two separate sub-pupils, which causes fringe jitter and can be reduced only by active fringe tracking.

Much interest has recently arisen in the potential of the high Antarctic plateau for astronomical observations. At Dome C ( $75^{\circ}06' \text{ S}$ ,  $123^{\circ}23' \text{ E}$ , 3235 m altitude), Agabi et al. [2] and Lawrence et al. [46] have – during the antarctic night and for a telescope positioned 30 m above the ground – determined a Fried parameter roughly equal to 37 cm, which is 2 to 3 times larger than at the best mid-latitude sites. However, direct measurements of the fluctuation times have yet to be performed.

In this paper we exploit the first stellar fringes recorded at Dome C (obtained with a Fizeau interferometer on a 20 cm baseline) and investigate how, despite their incomplete spatial and temporal sampling, they can be used to derive information on the coherence time of the piston.

## 2.2 Measurements

### 2.2.1 Observational setup

Several observations of *Canopus* were made at Dome C on January 31<sup>st</sup> and February 1<sup>st</sup> 2005, i.e. during the antarctic day. To track the fluctuations of the atmospheric piston, a modified Differential Image Motion Monitor (DIMM) [60] was placed 3.50 m above the ground. The DIMM is a telescope with a focal length of 2.80 m and 0.28 m diameter primary mirror, whose entrance pupil is covered by a mask with two 0.06 m diameter circular openings, with centers 0.20 m apart.

In a standard DIMM the two light beams remain separated, and the motions of the two images are compared. For our experiment, the light beams were recombined, the resulting image being a fringe pattern within the superposition of the two diffraction discs. The image is continuously deformed and shifted on the detector due to the atmospheric turbulence. The detector is a  $640 \times 480$  array of ( $9.9 \mu\text{m} \times 9.9 \mu\text{m}$ ) pixels. A Barlow lens was used to increase the effective focal length by a factor of three, which makes each pixel correspond to an angular increment  $0.24''$ . Images were taken every 28 ms, with exposure times of 1, 2 or 3 ms. Each film contains between 209 and 723 images and, thus, lasts roughly 5 to 20 s. Details are given in Table 2.1.

| Film number | Date     | Universal time | Altitude of<br>Canopus | Number<br>of frames | Exposure<br>time [ms] |
|-------------|----------|----------------|------------------------|---------------------|-----------------------|
| 1           | 31/01/05 | 9:03           | $61^\circ$             | 209                 | 3                     |
| 2           | 31/01/05 | 9:07           | $61^\circ$             | 723                 | 3                     |
| 3           | 01/02/05 | 7:45           | $59^\circ$             | 723                 | 3                     |
| 4           | 01/02/05 | 7:49           | $59^\circ$             | 723                 | 3                     |
| 5           | 01/02/05 | 8:11           | $58^\circ$             | 723                 | 3                     |
| 6           | 01/02/05 | 8:56           | $55^\circ$             | 723                 | 3                     |
| 7           | 01/02/05 | 8:59           | $55^\circ$             | 723                 | 2                     |
| 8           | 01/02/05 | 9:00           | $55^\circ$             | 723                 | 1                     |
| 9           | 01/02/05 | 9:41           | $52^\circ$             | 620                 | 1                     |

Table 2.1: Observational set-up. The observations were made on *Canopus* (HD 45348) at wavelengths between 350 and 600 nm. Images were taken every 28 milliseconds.

### 2.2.2 Data description

With perfectly stable atmosphere and no telescope vibrations all images would look alike. To analyse the effect of atmospheric turbulence, it is convenient to distinguish three image components:

- The two first components are the sets of *Airy discs* with diffraction rings, as they would be obtained for each hole separately. The two sets coincide in the absence of atmospheric disturbance. They are characterised by the angular diameter of their central lobe (Airy disc):

$$\theta_{\text{airy}} = 2.44 \lambda_0 / D = 3.98'' \quad (2.1)$$

$D = 6$  cm: diameter of the holes,  $\lambda_0 = 475$  nm: central wavelength.

- The third component is the fringe pattern due to the interference of light from the two mask openings. The fringes are perpendicular to the line joining the centres of the two holes, the *interferometric axis*. Their angular separation equals:

$$\theta_{\text{fringes}} = \lambda_0 / B = 0.49'' \quad (2.2)$$

$B = 20$  cm: baseline of the interferometer, i.e. distance between the centres of the two mask openings.

The interference pattern is finite, because the observations are made on a broad spectral band from 350 nm to 600 nm. The characteristic angular width where fringes appear is:

$$\theta_{\text{coh}} = 2 \lambda_0^2 / (B \Delta\lambda) = 1.86'' \quad (2.3)$$

$\Delta\lambda = 250$  nm: width of the wavelength interval.

The intensity profiles along the interferometric axis, is:

$$I(\theta) = 2 I(0) \left[ J_1 \left( \frac{2.44\pi\theta}{\theta_{\text{airy}}} \right) / \left( \frac{2.44\pi\theta}{\theta_{\text{airy}}} \right) \right]^2 \left[ 1 + \text{sinc} \left( \frac{2\pi\theta}{\theta_{\text{coh}}} \right) \cos \left( \frac{2\pi\theta}{\theta_{\text{fringes}}} \right) \right] \quad (2.4)$$

Even if the atmosphere were turbulence free and the telescope were optically perfect, the measured profile would differ from the pattern specified in Eq. 2.4. This is so, because – constrained by the available instrumentation – the fringe pattern had to be sampled with relatively crude resolution. Whereas the fringe pattern has an angular period of  $\theta_{\text{fringes}} = 0.49''$ , each pixel corresponds already to an angular increment  $\theta_{\text{pixel}} = 0.23''$ . As it results from the integration over fairly crude intervals, the measured intensity profile can, thus, not resemble closely the intensity profile given by Eq. 2.4. However, as shown in the following section, the information content is sufficient to extract – with suitable fitting procedure – the relevant parameters. Figure 2.1 exemplifies a recorded

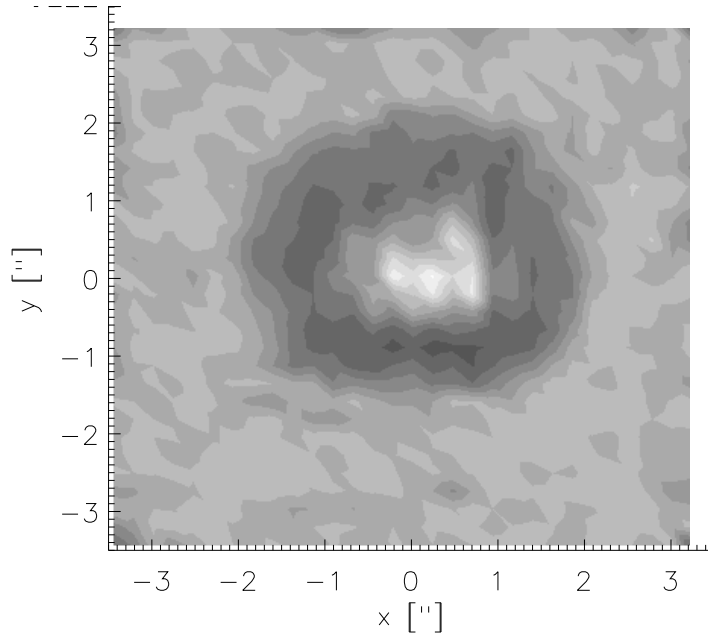


Figure 2.1: Example of an image recorded through the interferometer. The mask openings are aligned along the x axis.

image. The atmospheric turbulence keeps the image of the star moving on the

detector. The local inclination of the wave front over each of the holes causes the movements of the Airy discs, whereas difference in the optical path for the two holes, i.e. the piston, shifts the fringe pattern relative to the centre of the Airy discs. Telescope vibrations, on the other hand, cause merely a common movement of Airy discs and fringes. The relative movements between airy discs and fringes are, therefore, solely due to the atmospheric turbulence. The subsequent analysis deals with their temporal patterns.

Piston changes shift the fringe pattern relative to the Airy discs along the interferometric axis. Accordingly, in order to assess the temporal fluctuations of the piston it is sufficient to consider the shift along the axis.

### 2.3 Quantifying the motion of the fringe pattern and the Airy discs

Observations with a DIMM are commonly aimed at measuring the seeing parameter by observing the relative motions of the Airy discs. In the present measurements the two beams have been combined in order to analyze the piston in terms of the motion of the fringe packet relative to the combined Airy discs. The quantification of the axial motion requires the extraction of 4 parameters from the observed images:

- position of the central fringe  $\theta_f$  and contrast of the fringe pattern  $k$ ,
- position, along the interferometric axis, of the center of the combined Airy discs:  $\theta_0$ ,
- intensity at the center of the combined Airy discs:  $I_0$ .

No attempt was made to separate the two airy discs, since this would have meant fitting six parameters on intensity profiles specified in terms of only 8 ( $\sim \theta_{\text{coh}}/\theta_{\text{pixel}}$ ) data points.

The intensity profile is made up of three components with different spatial periods (cf. Eq. 2.4):  $\theta_{\text{airy}}/1.22$ ,  $\theta_{\text{coh}}$  and  $\theta_{\text{fringes}}$ . In line with relations discussed in the previous section, all three periods are superior to twice the pixel size  $\theta_{\text{pixel}}$ . Hence, in spite of the fairly crude detector resolution the intensity profile is adequately sampled to extract unambiguously the central position of the two Airy discs and the fringe pattern. To do so, the following profile was fitted onto the recorded intensity profiles:

$$I(\theta) = \int_{\theta - \theta_{\text{pixel}}/2}^{\theta + \theta_{\text{pixel}}/2} 2I_0 \left[ J_1 \left( \frac{2.44\pi(\theta' - \theta_0)}{\theta_{\text{airy}}} \right) / \left( \frac{2.44\pi(\theta' - \theta_0)}{\theta_{\text{airy}}} \right) \right]^2 \left[ 1 + k \operatorname{sinc} \left( \frac{2\pi(\theta' - \theta_f)}{\theta_{\text{coh}}} \right) \cos \left( \frac{2\pi(\theta' - \theta_f)}{\theta_{\text{fringes}}} \right) \right] d\theta' \quad (2.5)$$

The non-linear least square algorithm written by C. Markwardt [51] was uti-

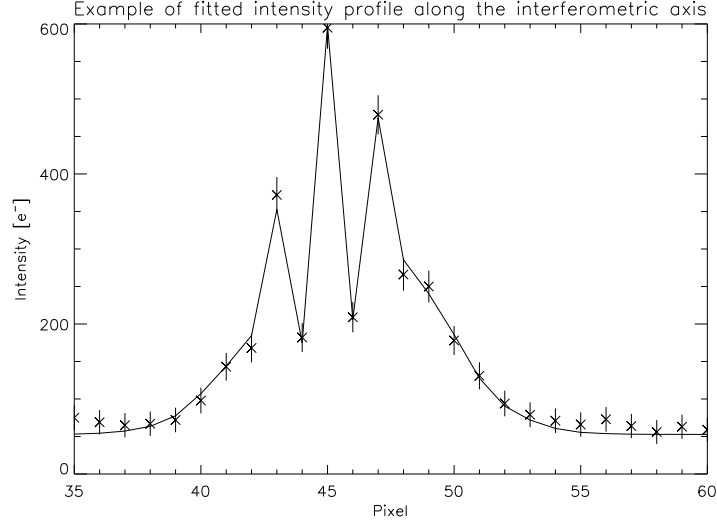


Figure 2.2: Example of data points recorded along the interferometric axis. The fit (solid line) is done on four parameters  $(\theta_f, k, \theta_0, I_0)$ , using Eq. 2.5. See text for more details. The graph refers to an image of film 5.

lized. Figure 2.2 shows a profile fitted onto an image of film 5. The error bars around the data points are computed through following relation:

$$\sigma(\theta) = (\sigma_p(\theta)^2 + \sigma_d^2)^{1/2} \quad (2.6)$$

The photon noise,  $\sigma_p$ , equals the square root of the signal, whereas the noise of the detector is dominated by the readout noise and equals  $\sigma_d \sim 14$  electrons.

Each fit determines the set of four parameters  $(\theta_f, k, \theta_0, I_0)$  that minimizes the mean squared distance,  $\chi^2$ , between the data points and the values derived from Eq. 2.5. The error bars on the parameters correspond to  $\chi^2$  doubling. Two of the parameters then provide the axial separation between the central fringe and the center of the combined Airy discs:  $\theta_f - \theta_0$ . Figure 2.3 gives the *rms* of the position of the combined Airy discs,  $\theta_0$ , and of the separation between the central fringe and the combined Airy discs,  $\theta_f - \theta_0$ , up to the times specified on the abscissa. The starting values are based on the 100 images taken up to  $t = 2.8$  s. For the characterization of the atmospheric turbulence instrument related artifacts need to be negligible. For the absolute motion this condition is violated by telescope vibrations and by the imperfect tracking which makes the star actually drift off: the *rms* does not converge towards a fixed value, i.e. the motion is not stationary. For the separations the value fluctuates around a central value with roughly constant amplitude, i.e. the *rms* remains essentially constant (cf. Figure 2.3). This indicates that the observed relative motion is due to atmospheric turbulence which is stationary.

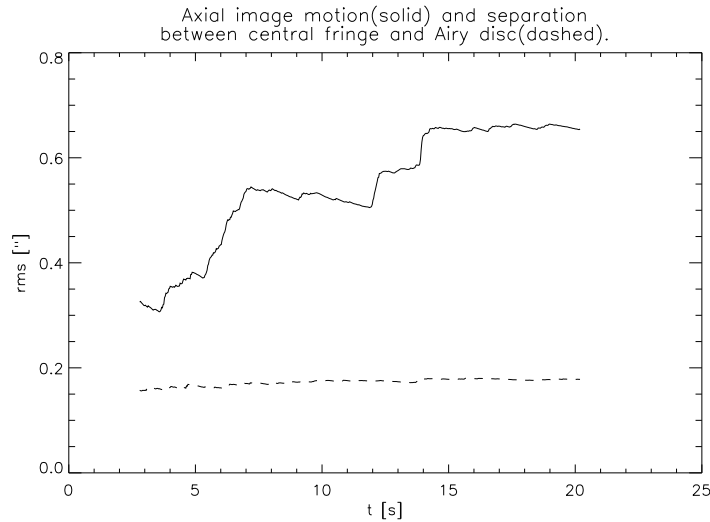


Figure 2.3: Solid line: *rms* deviations of the axial image motion, measured over subsets of increasing size between 100 and 723 images. Dashed line: *rms* deviations of the axial separation between the central fringe and the combined Airy discs. The graph refers to the data set of film 5.

## 2.4 Coherence time

### 2.4.1 Estimating coherence time through Fourier analysis

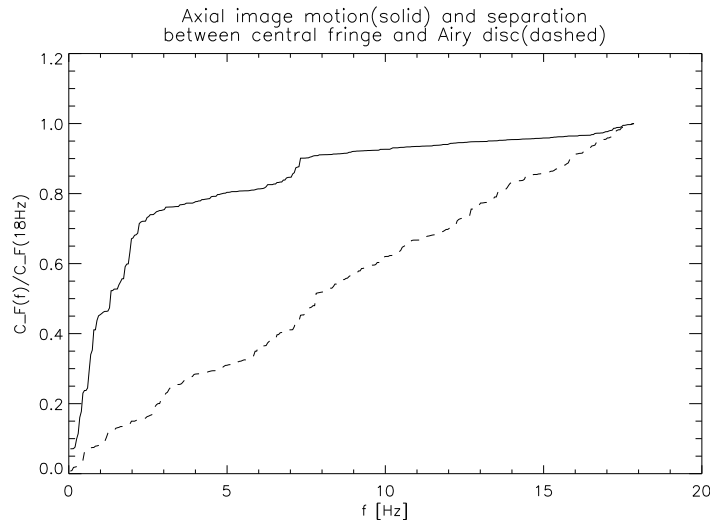


Figure 2.4: Cumulative squared norm of the Fourier transform for the data set of film 5.

To measure the complete spectrum of turbulence induced movement, it is necessary to record images at least about twice as fast as the fastest component of the turbulence. In the present measurements the recording rate was constrained by the camera to  $\sim 35$  Hz. Accordingly, the Fourier analysis can reveal spectral components of the turbulence up to only  $\sim 17$  Hz.

Whether the predominant fraction of the turbulence is slower than the sam-

pling rate is judged by taking the Fourier transform of the image motions and plotting the cumulated squared norm versus the frequency (cf. Figure 2.4). According to the Kolmogorov theory of turbulence the cumulative squared norm,  $C_F(f)$ , becomes constant after the highest frequencies of atmospheric turbulence.

- For the absolute motions the nearly horizontal slope at 17 Hz implies that the main part of the telescope vibrations is associated with lower frequencies.
- For the relative motions the dependence  $C_F(f)$  still has positive slope at  $f = 17$  Hz, which suggests that the fastest components of the turbulence exceed the recording rate. Thus, the characteristic time scales of atmospheric turbulence are inferior to  $\sim 60$  ms, which is a very loose constraint, given typical atmospheric time scales. [46] It is of interest, whether the conclusions can be sharpened in terms of other considerations.

#### 2.4.2 Estimating coherence time through the evolution of correlation

Although the sampling rates were too low in the present measurements to assess the fastest atmospheric turbulence through Fourier analysis, some informative inferences are still possible, because relevant information can be obtained by tracing the decay time of correlation between successive fringe positions. Figure 2.6 represents the following structure function as a function of temporal separation:

$$D_{\Delta\theta}(t) = \langle |\Delta\theta(\tau + t) - \Delta\theta(\tau)|^2 \rangle \quad (2.7)$$

$\Delta\theta = \theta_f - \theta_0$ : separation between the central fringe and the combined Airy discs.

Figure 2.6 suggests that during films 1, 3, 5, 6, 7, 8 the cells of the turbulent atmosphere were correlated up to a hundred milliseconds, which is a very promising result.

The coherence time of piston is estimated by comparing the structure function predicted by the Kolmogorov spectrum of fluctuations [58] with the observed data:

$$D(t) = D(t \gg t_0) \times (1 - \exp(-(t/t_0)^{-5/3})) \quad (2.8)$$

$t_0$ : coherence time.

Theoretical calculations have shown temporal power spectra of fringe motion to have a shape that is unaffected by wind direction and baseline orientation. [17] In the case of differential image motion, only the low frequency domain is dependent of wind direction. Evolution times of the separation

between the central fringe and the combined Airy discs should, thus, be insensitive to wind direction and baseline orientation on times scales of several coherence times. We therefore take Eq. 2.8 as a valid approximation independently of wind direction and baseline orientation.

In Figure 2.6 the measured correlation curve is compared to theoretical curves obtained for the coherence times: 10, 30 and 50 milliseconds. At most five data points lie inside the domain where the structure function has not reached its asymptotic value. Still, Figure 2.6 appears to suggest that during films 1, 3, 5, 6, 7, 8, the coherence time of piston was superior to ten milliseconds. The coherence time was highest during films 6, 7, 8, i.e. around 9:00 UT on February 1<sup>st</sup>. This is consistent with measurements of the seeing

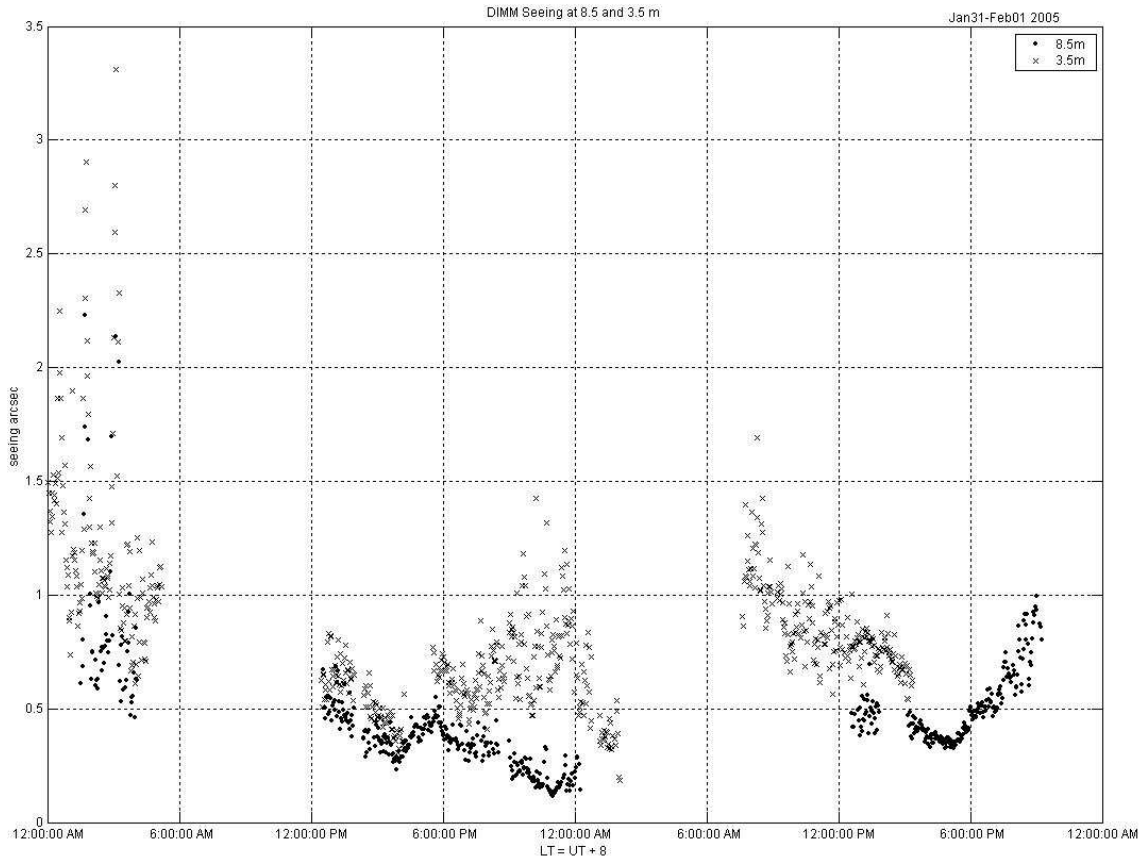


Figure 2.5: Seeing angles measured by two DIMM instruments: located 3.5 m and 8.5 m above the ground, on January 31<sup>st</sup> and February 1<sup>st</sup> 2005.

angle at the same epoch: Figure 2.5 gives the seeing angles measured by two DIMM instruments located 3.5 m and 8.5 m above the ground, on January 31<sup>st</sup> and February 1<sup>st</sup>. The upper data series were acquired by the same telescope which was used for recording the fringes here analyzed. This explains the interruptions of the upper data series around 9:00 UT the first day and starting from 7:45 UT the second day. As can be seen from the data recorded with the

instrument located at 8.5 m, the seeing angle reached a local minimum around 9:00 UT on February 1<sup>st</sup>.

### 2.4.3 Optimal setup for coherence time measurements

The observations reported here were made with the equipment available on the site and are subject to the following limitations, which will need to be lifted in future observations:

- The recording speed of the camera was not fully sufficient for sampling of atmospheric turbulence. Increased recording rate will permit the precise determination of the actual coherence time. The highest frequencies of the piston should – in line with the earlier (Agabi et al. [2] and Lawrence et al. [46]) and the present measurements – be less than 500 Hz. Accordingly a recording rate of 1000 Hz should ensure adequate temporal sampling.
- Caution is required, when the turbulent cells are larger than the distance between the two mask openings (20 cm). In these cases the difference between piston and tilt becomes too small to infer coherence times with sufficient precision. At the time of observations, the seeing varied between 0.5" and 1.0" (cf. Figure 2.5). Thus, at 500 nm wavelength, the turbulent cells had a characteristic size (Fried parameter) between 10 cm and 20 cm, i.e. only just smaller than the baseline. For future measurements, we consider the use of larger baselines up to 2 m.

## 2.5 Conclusion

Stellar fringes were recorded at the Antarctic site of Dome C during day time, using a Fizeau configuration on a modified DIMM telescope. Despite the partial temporal and spatial sampling limitations imposed by the locally available equipment, it was possible to determine a promising lower limit (around 10 ms) to the coherence time of piston and to validate our experimental procedure. We are now considering regular observations using a dedicated setup – with larger baselines and higher recording rates – to characterize the time scales of atmospheric piston at Dome C, both during day and night time.

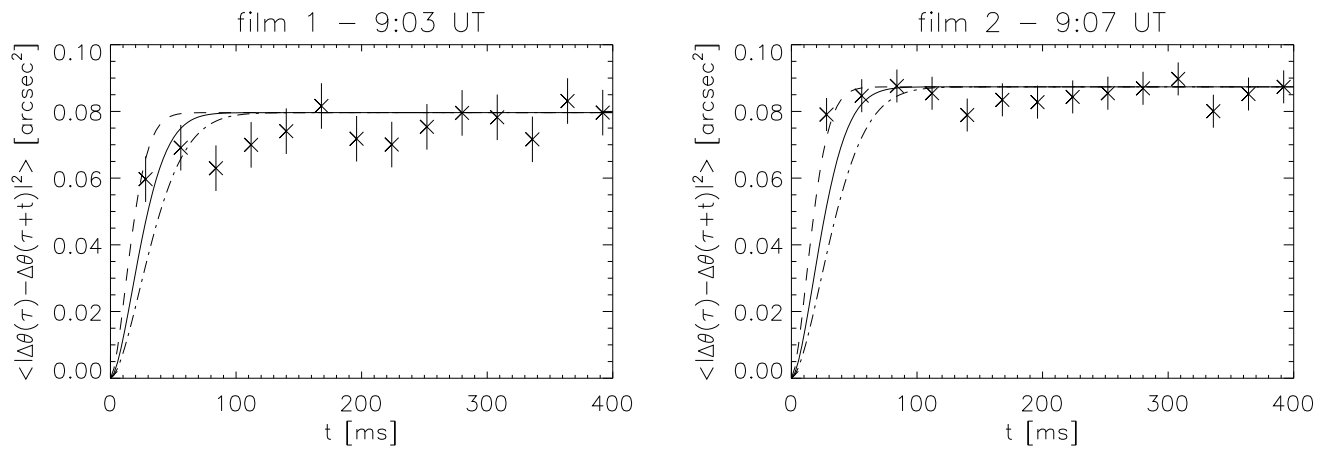
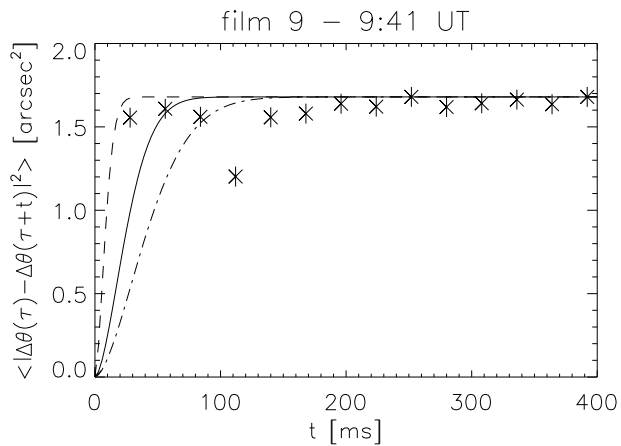
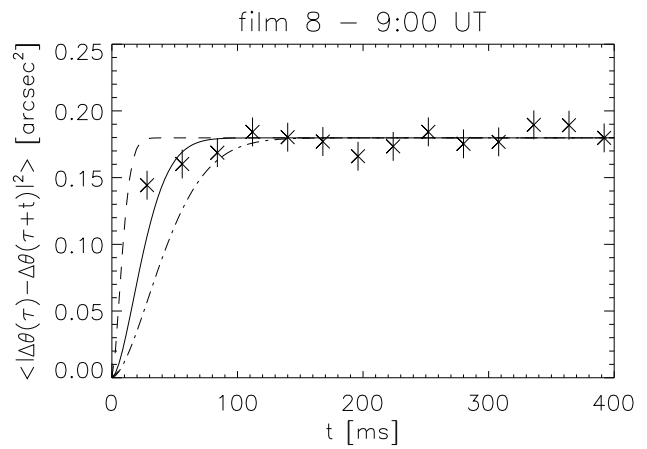
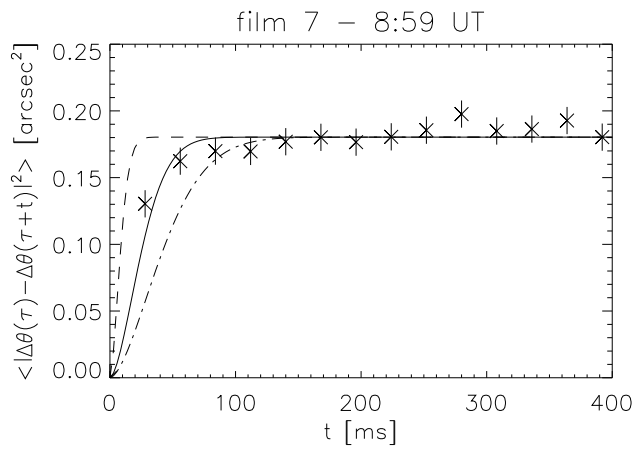
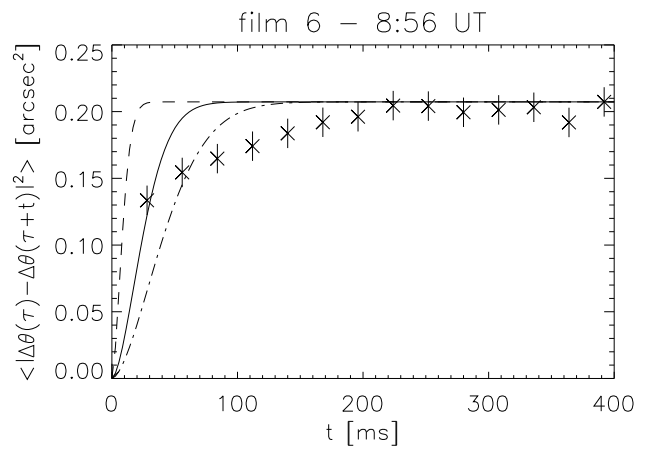
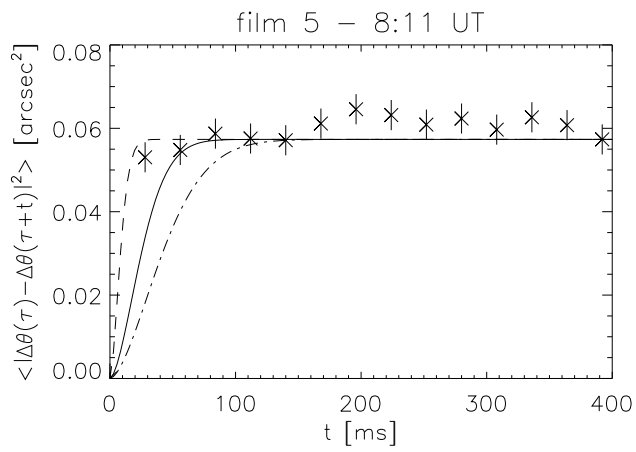
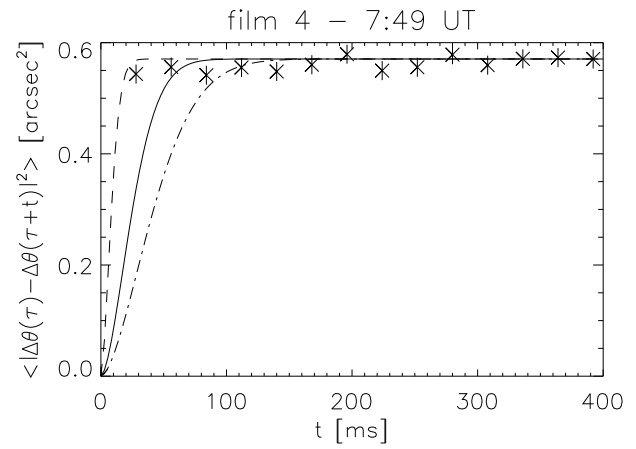
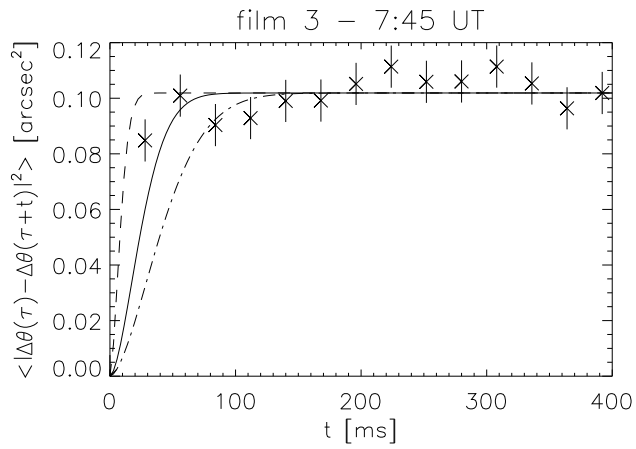


Figure 2.6: Structure function of the separation between the central fringe and the combined Airy discs. The fits correspond to coherence times equal to 10 (upper curve), 30, 50 ms (lower curve) (cf. Eq. 2.8). During films 1, 3, 5, 6, 7, 8 the coherence time appears to have been superior to ten milliseconds.



## Chapter 3

# A method of estimating time scales of atmospheric piston and its application at Dome C (Antarctica) – II

A. Kellerer, M. Sarazin, T. Butterley, R. Wilson, 2007, *Applies Optics*, in press

### Abstract

Temporal fluctuations of the atmospheric piston are critical for interferometers as they determine their sensitivity. We characterize an instrumental set-up, termed the piston scope, that aims at measuring the atmospheric time constant,  $\tau_0$ , through the image motion in the focal plane of a Fizeau interferometer.

High-resolution piston scope measurements have been obtained at the observatory of Paranal, Chile, in April 2006. The derived atmospheric parameters are shown to be consistent with data from the astronomical site monitor, provided that the atmospheric turbulence is displaced along a single direction. Piston scope measurements, of lower temporal and spatial resolution, were for the first time recorded in February 2005 at the Antarctic site of Dome C. Their re-analysis in terms of the new data calibration sharpens the conclusions of a first qualitative examination [41].

### 3.1 Introduction

Interferometers have been introduced in astronomy to gain in spatial resolution without the need to build extremely large telescopes. To resolve *Sirius*, observations in the infrared domain ( $\sim 2\mu\text{m}$ ) would require a telescope of about 170 m mirror diameter. Fortunately, *Sirius* can also be resolved by two telescopes of more modest size, separated by 170 m and operated as an interferometer. Yet, despite this considerable gain in resolution, interferometers are not the prime tool of today’s astronomers. This is largely due to their limited sensitivity: atmospheric turbulence makes the interferometric fringe pattern move in the detector plane. Accordingly, one tends to use exposure times that are short enough to “freeze” the turbulence, i.e. typically several milliseconds. To increase the sensitivity, phasing devices are being designed that measure the position of the fringe pattern due to a reference star, and correct continuously for the fringe motion of the target object. For such devices to work, a sufficient number of photons need to be collected on the reference star during the time when the atmosphere is frozen, i.e. during the *atmospheric coherence time*  $\tau_0 = 0.314 r_0/\bar{V}_{5/3}$ , where  $r_0$  is the *Fried parameter* and  $\bar{V}_{5/3}$  is a weighted average of the turbulent layers’ velocities. Clearly, the coherence time is the parameter that determines the performance of today’s interferometers. Different definitions of the atmospheric coherence time have been introduced in relation to various observational techniques: single telescopes with or without adaptive-optics, interferometers with or without fringe trackers etc. However the standard adaptive-optics coherence time  $\tau_0$  has been shown to quantify the performance of all these techniques [42].

In a previous article [41], we characterized the temporal evolution of fringe motion at Dome C, a summit on the antarctic continent, and a potential site for a future interferometer, using the motion of the fringe pattern formed in the focal plane of a Fizeau interferometer. The temporal and spatial sampling of the measurements were low due to the available equipment and, instead of determining coherence-time values, the mean duration of correlation was assessed by fitting the fringe correlation-function onto an exponential curve (cf. Section 3.4). Such measurements have now been repeated at the site of Paranal, Chile, with sufficient spatial and temporal sampling, to allow the determination of the coherence time. Further, all relevant atmospheric parameters are constantly monitored at Paranal by a meteorological station, hence the parameter values derived through our set-up (termed *piston scope*) can be checked against reference values.

In the first Section, the quantities measured with the piston scope are related to the following atmospheric parameters: the Fried parameter, the turbulent layers velocities and the coherence time – using the Kolmogorov theory of atmospheric turbulence. The relations are then tested on the observations performed at Paranal. It is shown that when the sampling is sufficient, the precision on the coherence time is limited by the piston scope’s sensitivity to wind direction. Given these results, the third Section presents a new analysis

of the measurements obtained at Dome C [41]. The lower limits to the coherence time, derived through our first qualitative analysis, are confirmed and additional results on the Fried parameter and wavefront speed are given.

## 3.2 Formalism

The purpose of the piston scope experiment is to track the rapid fluctuations of the atmospheric piston. To this effect, the entrance pupil of a telescope is covered by a mask with two circular openings. The resulting image is a fringe pattern within the superposition of the two diffraction discs. Atmospheric turbulence keeps the image of the star moving on the detector. The local inclination of the wave front over each of the holes causes the movement of the Airy discs, whereas difference in the optical path for the two holes, i.e. the piston, shifts the fringe pattern relative to the center of the Airy discs. Telescope vibrations, on the other hand, cause merely a common movement of Airy discs and fringes. The relative movements between Airy discs and fringes are, therefore, solely due to the atmospheric turbulence. The subsequent analysis deals with their temporal patterns. Piston changes shift the fringe pattern relative to the Airy discs along the interferometric axis. Accordingly, in order to assess the temporal fluctuations of the piston it is sufficient to consider the shift along the axis.

As suggested by Conan et al. [17], the spatial power spectrum  $W_\phi$  of the relative movements between Airy discs and fringes is derived from the phase spectrum  $W_\varphi$ , assuming a Kolmogorov model of turbulence with an infinite outer scale. In the following we use the notations of Conan et al. [17].

$$W_\varphi(\mathbf{f}) = 0.00969 k^2 \int_0^{+\infty} f^{-11/3} C_n^2 dh, \quad (3.1)$$

where  $\mathbf{f}$  is the spatial frequency and  $k = 2\pi/\lambda$  the wavenumber. The turbulence intensity of a layer  $i$  of thickness  $dh$  at altitude  $h$  is specified in terms of  $C_n^2 dh$ . The explicit dependence of  $C_n^2$  and all following parameters on  $h$  is dropped to ease the reading of the formulae. The measured quantity is the separation – along the interferometric axis,  $x$  – between the central fringe and the center of the combined Airy discs. The spatial filter  $\tilde{M}$  that converts  $W_\varphi$  into the power spectrum  $W_\phi$  equals:

$$\tilde{M}(\mathbf{f}) = \lambda/(2\pi) A(\mathbf{f}) FT[(\delta_B - \delta_0)/B - (\delta_B + \delta_0)/2 * d/dx](\mathbf{f}), \quad (3.2)$$

for a baseline vector  $\mathbf{B}$  and the aperture filter function  $A(\mathbf{f})$ . For a circular aperture of diameter  $D$ ,  $A(\mathbf{f}) = 2J_1(\pi f D)/(\pi f D)$  and  $f = |\mathbf{f}|$ .  $J_n$  stands for the Bessel function of order  $n$ .  $FT$  represents the Fourier transform,  $\delta_L$  is the delta function centered on  $L$  and  $*$  denotes convolution. Hence,

$$\tilde{M}(\mathbf{f}) = \lambda/(2\pi) A(\mathbf{f}) [2 \sin(\pi \mathbf{f} \mathbf{B}) - 2\pi \mathbf{f} \mathbf{B} \cos(\pi \mathbf{f} \mathbf{B})] / B \quad (3.3)$$

$$W_\phi(\mathbf{f}) = \tilde{M}^2(\mathbf{f}) W_\varphi(\mathbf{f}). \quad (3.4)$$

In the single layer approximation, we assume the turbulent layer to be transported with a velocity  $\mathbf{V}$  directed at an angle  $\alpha$  with respect to the baseline. The temporal power spectrum of the measured quantity is obtained by integrating in the frequency plane over a line displaced by  $f_x = v/V$  from the coordinate origin and inclined at angle  $\alpha$ . Let  $f_y$  be the integration variable along this line and  $f^2 = f_x^2 + f_y^2$ . The temporal power spectrum equals:

$$w_\phi(v) = \frac{1}{V} \int_{-\infty}^{+\infty} W_\phi(f_x \cos \alpha + f_y \sin \alpha, f_y \cos \alpha - f_x \sin \alpha) df_y \quad (3.5)$$

We then derive the expression of the structure function:

$$\begin{aligned} D_\phi(t) &= 2 \int_{-\infty}^{+\infty} (1 - \cos(2\pi vt)) w_\phi(v) dv & (3.6) \\ &= 2 \times 0.00969 C_n^2 dh / B^2 \int_0^{+\infty} f^{-8/3} (2J_1(\pi f d) / (\pi f d))^2 df \\ &\quad \int_0^{2\pi} (1 - \cos(2\pi f \cos(\theta + \alpha) V t)) \\ &\quad [2 \sin(\pi B f \cos \theta) - 2\pi f B \cos \theta \cos(\pi f B \cos \theta)]^2 d\theta & (3.7) \end{aligned}$$

The best estimate of the parameters is obtained by fitting the measured points

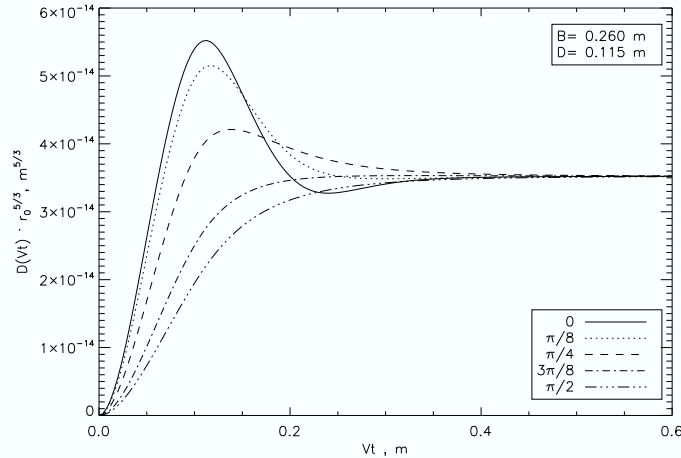


Figure 3.1: Structure functions of the fringe position relative to the combined Airy discs, for an interferometer with mirror diameters  $D$  and baseline length  $B$ . The atmosphere is assumed to consist of a single layer displaced with wind speed  $V$  at an angle  $\alpha$  from the baseline. The values of  $\alpha$  are indicated in the bottom right box.

to:  $D_\phi(t) + K$ , where  $K$  is a constant that allows for white measurement noise. As seen from Eq. 3.7, the structure function depends on the wind orientation  $\alpha$  because the mask of the piston scope is not rotationally symmetric. Temporal evolutions of the structure functions, for different values of  $\alpha$ , are represented on Figure 3.1. The asymptotic value of the structure function at large time

increments is determined by the Fried parameter  $r_0$ , whereas the time needed to reach the asymptotic value is a function of the velocity  $V$ .

### 3.3 Measurements at Paranal

#### 3.3.1 Observational set-up

Several observations of *Spica* were obtained at Paranal on the nights from 22-23 and 23-24 April 2006, using a modified SLODAR [12] (Slope detection and ranging). This SLODAR is designed to measure profiles of the atmospheric turbulence with a telescope that has a 0.4 m diameter primary mirror, and a focal length of 4.064 m. The detector is a  $128 \times 128$  array of  $(24 \times 24) \mu\text{m}^2$  pixels with a peak quantum efficiency of 92% at  $\lambda_0 = 550 \text{ nm}$  and next to zero read-out noise. For our experiment the entrance pupil of SLODAR was covered by a mask with two circular openings of diameter  $D = 0.115 \text{ m}$  and centers  $B = 0.260 \text{ m}$  apart. The resulting image is a fringe pattern of angular period  $\lambda_0/B = 0.44''$  within the superposition of two Airy discs of diameter  $2.44\lambda_0/D = 2.41''$ . Two lenses were used to increase the focal length by a factor 16.67, this makes each pixel correspond to an angular increment of  $0.073''$ . During the first night, a sequence of 1000 images was recorded at 240 Hz with an exposure time equal to 2 ms. On the following night, six sequences of 1000 images were recorded at 300 Hz with 1 ms exposure time.

The piston is quantified in terms of the motion of the fringe packet relative to the combined Airy discs. The quantification of the axial motion requires the extraction of the following parameters from the observed images: the position of the central fringe and the position – along the interferometric axis – of the center of the combined Airy discs. This extraction has been described in detail in a previous article [41]. An example of a raw image is shown on Figure 3.2 with the corresponding, fitted intensity profile.

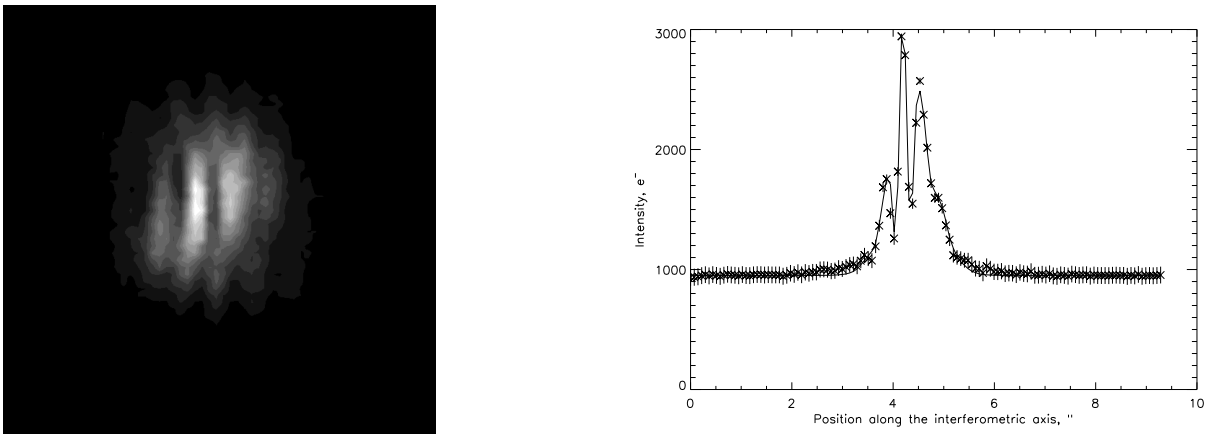
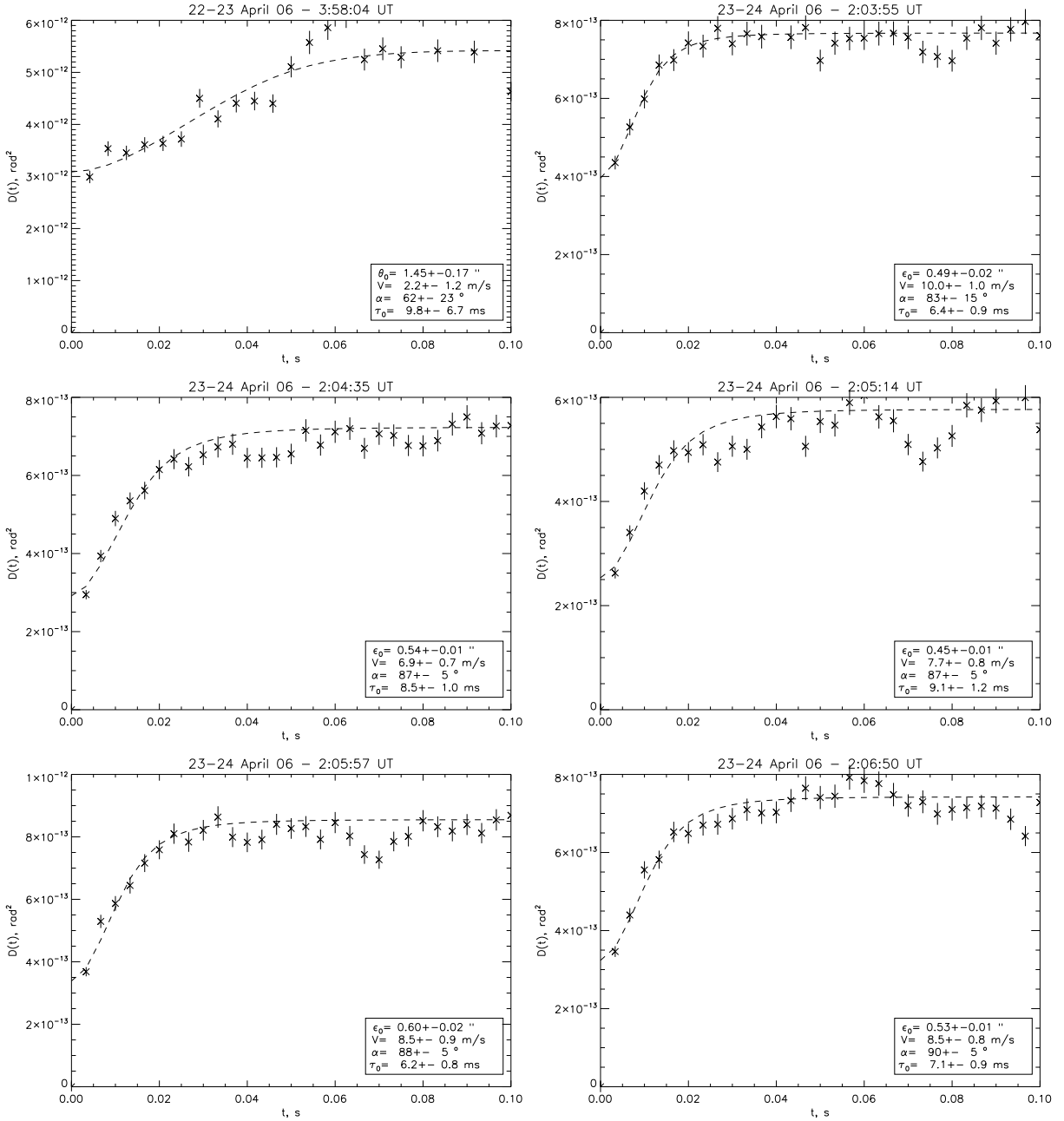


Figure 3.2: Example of an image recorded with 1 ms exposure time at Paranal on the night of 23-24 April at 02:03:55 UT and fitted intensity profile along the axial direction.

### 3.3.2 Derivation of atmospheric parameters



The Fried parameter  $r_0$ , the wavefront velocity  $V$  and orientation  $\alpha$  are derived by fitting  $D_\phi(t) + K$  onto the data points, as described in Section 3.2.  $D_\phi(t)$  corresponds to an atmospheric model where the turbulence is contained in a single layer, that is displaced as a whole with the velocity  $V$  under an angle  $\alpha$ .

The resulting parameter values and uncertainties are indicated on Figure 3.3. The latter correspond to a doubling of the squared deviation of the data points to the theoretic structure function. The Fried parameter is determined by the asymptotic value of the structure function at large time increments. To ease

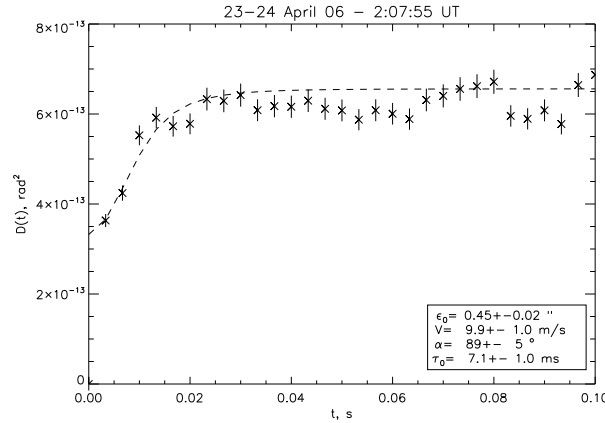


Figure 3.3: Theoretical structure functions (dashed lines) fitted onto data obtained at Paranal, the resulting seeing  $\epsilon_0$ , velocity  $V$ , wind orientation  $\alpha$  and coherence time  $\tau_0$  are indicated.

the comparison with the meteorological station of Paranal, we indicate the *seeing angle*  $\epsilon_0$  rather than the Fried parameter  $r_0$ , these two parameters are essentially equivalent:  $\epsilon_0 = 0.976 \lambda/r_0$  [rad].  $V$  and  $\alpha$  are derived from the first few measurement points and the coherence time,  $\tau_0$ , is then obtained through the classic relation:  $\tau_0 = 0.314 r_0/V$ .

### 3.3.3 Performance of the piston scope

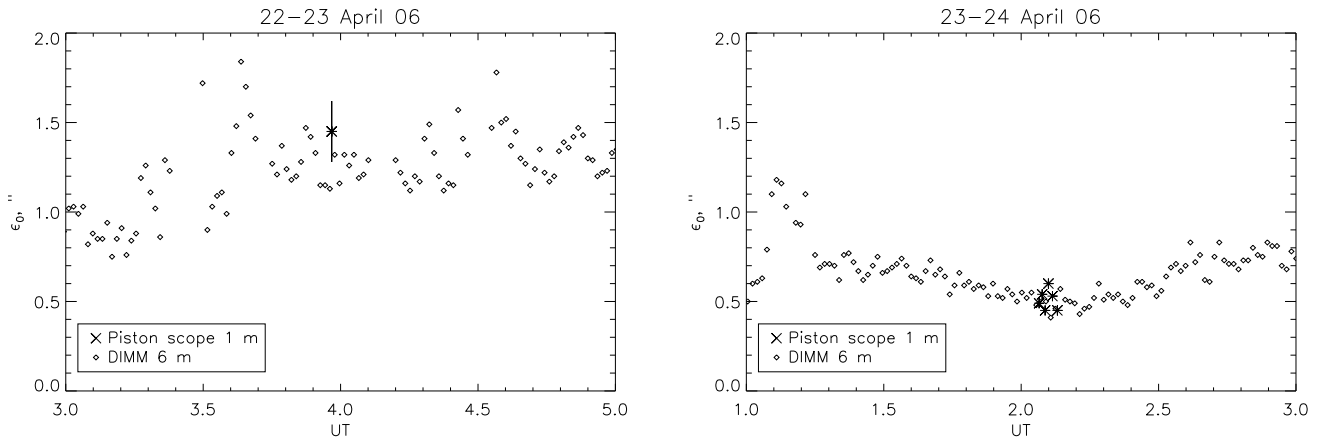


Figure 3.4: Seeing values measured at Paranal with the DIMM and the piston scope. The uncertainties of the piston scope values correspond to a twofold increase in the quality of the data adjustment.

On Figures 3.4-3.6, the values of  $\epsilon_0$ ,  $V_{ps}$  and  $\tau_0$  obtained with the piston scope are compared to measurements in terms of the Paranal monitoring-instruments. We do not compare the wind orientations, because the value of  $\alpha$  that is obtained with the piston scope depends on the position of the mask, hence on the pointing of the telescope, and it is difficult to relate it to the angle measured by the meteorological station.

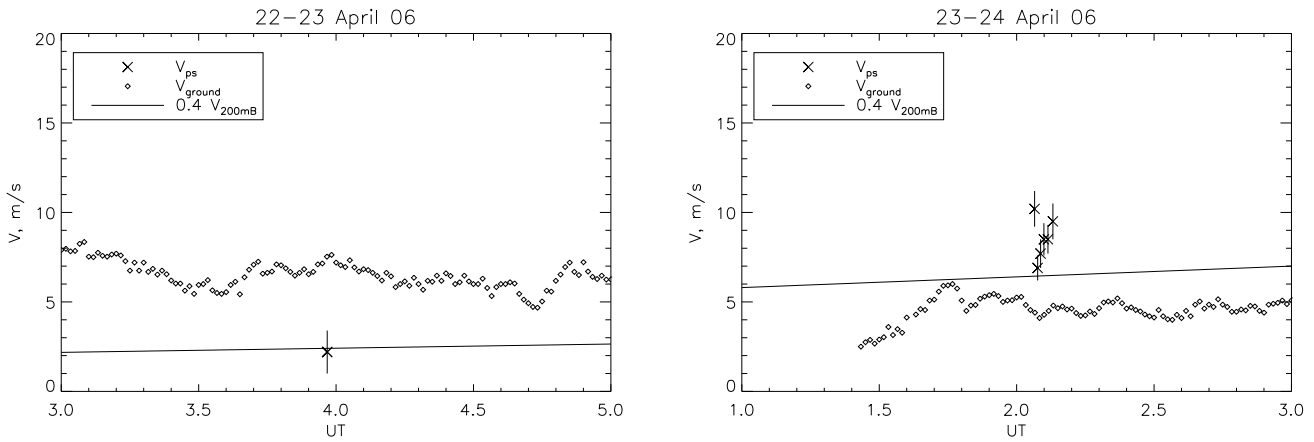


Figure 3.5: Wavefront velocities obtained with the piston scope ( $V_{ps}$ ), wind velocities measured by sensors at 30 m above the ground of Paranal ( $V_g$ ) and interpolated at 200 mB from ECMWF data ( $V_{200mB}$ ).

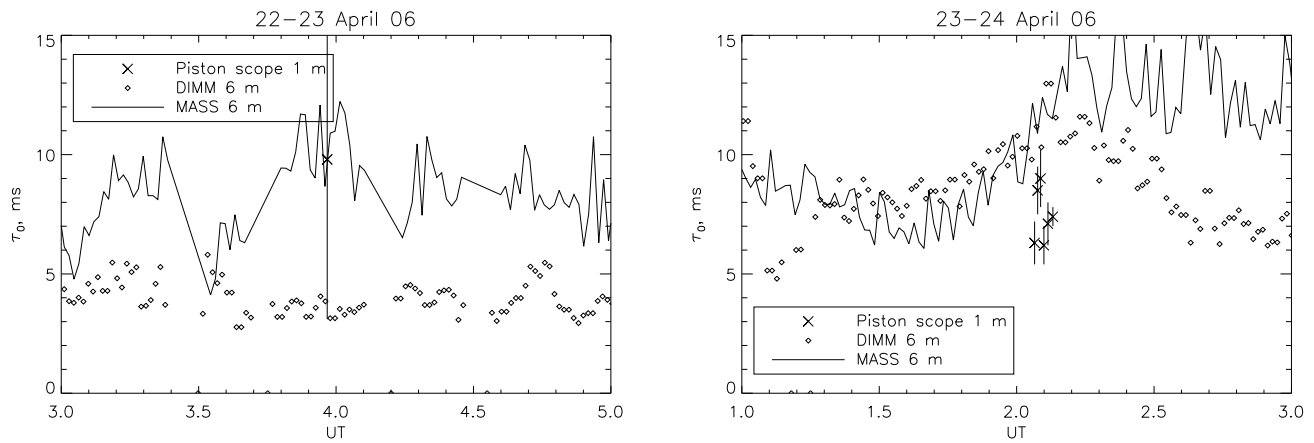


Figure 3.6: Coherence times obtained at Paranal through three different methods.

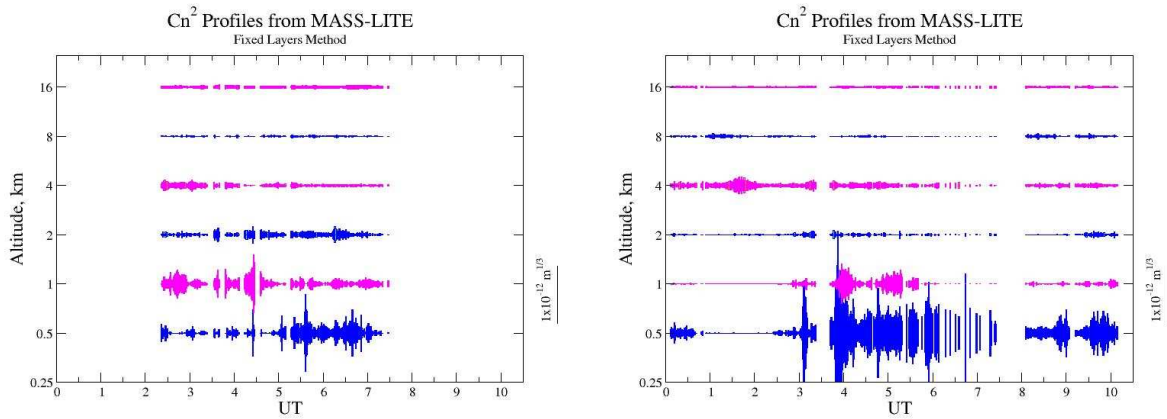


Figure 3.7: Profiles of the free atmosphere turbulence obtained by MASS at Paranal. On 22-23 April (left panel) the turbulence was contained in several layers of similar intensity, while on 23-24 April (right panel) one layer at 4 km was predominant around 2:00 UT.

- Seeing values (see Figure 3.4): The values estimated with the piston scope coincide with those measured at 6 m height by the DIMM [60] (Differential Image Motion Monitor). Note that we assume the atmosphere to consist of one layer displaced along a single direction, yet Figure 3.7 shows that on 22-23 April the turbulence was contained in several layers with similar intensity. However, the asymptotic value of the structure function has the same altitude dependence as the seeing:

$$D_\phi(t \gg \tau_0) \propto r_0^{-5/3} \propto \int_0^{+\infty} C_n^2 dh \quad (3.8)$$

therefore the seeing estimated by the piston scope is correct independently of turbulence profile.

- Velocities (see Figure 3.5): The wavefront velocity  $V_{\text{ps}}$  derived with the piston scope is a turbulence-weighted average of the layers' velocities  $V(h)$ . Ideally,  $V_{\text{ps}}$  should have the same dependence on turbulence parameters as  $\tau_0$ , hence:

$$V_{\text{ps}} \propto \bar{V}_{5/3} = \left[ \frac{\int_0^{+\infty} V(h)^{5/3} C_n^2(h) dh}{\int_0^{+\infty} C_n^2(h) dh} \right]^{3/5} \quad (3.9)$$

Sarazin & Tokovinin [59] give an empirical relation between  $\bar{V}_{5/3}$  and the wind speeds measured at ground level and at 200 mB pressure. That relation has been verified at Paranal and Cerro Pachon in Chile, and later confirmed at San Pedro de Martir, Mexico:

$$\bar{V}_{5/3} \approx \max(V_g, 0.4 V_{200\text{mB}}) \quad (3.10)$$

At Paranal,  $V_g$  is measured by wind sensors at 30 m height and  $V_{200\text{mB}}$  is estimated every 6 hours by the ECMWF [21] (European Center for Medium Range Weather Forecast) through a global meteorological model which runs twice a day at 00 UT and 12 UT. This involves the assimilation of worldwide-collected data from radio soundings, satellite observations etc.

It appears from Figure 3.5 that the wavefront velocities derived with the piston scope coincide with  $0.4 V_{200\text{mB}}$ , rather than  $\bar{V}_{5/3} \approx \max(V_g, 0.4 V_{200\text{mB}})$ . When the turbulence is contained in several layers, the measured structure function is an average of single-layer structure functions as represented on Figure 3.1. If these layers have different wind velocities and orientations, the dispersion of the data points around the best-fitting structure function is large and the resulting wavefront velocity is poorly constrained. Accordingly, and in line with Figure 3.7,  $V_{\text{ps}}$  is derived with respectively 55% and 10% uncertainties during the first and second night of observations.

- The coherence time (see Figure 3.6) is a combination of the seeing and wavefront velocity, thus it is essentially unconstrained during the first night. On the subsequent night, the values are consistent with those derived through the two following methods: With MASS,  $\tau_0$  is assessed

from the scintillation through a 2 cm diameter aperture. MASS is not sensitive to the lower layers of turbulence ( $< 500$  m), and, correspondingly, measures higher coherence times. A second value of  $\tau_0$  is obtained by combining DIMM seeing-values with measurements of the wind speed:  $\tau_0 = 0.314 r_0 / \bar{V}_{5/3}$ , where  $\bar{V}_{5/3}$  is estimated by Eq. 3.10. Since these values are obtained from distinct locations with different telescopes pointing at different stars, we do not expect them to coincide. The results seem to suggest that the piston scope sees more turbulence than MASS and DIMM: While this is probable – the piston scope is installed inside a dome at ground level, whereas MASS and DIMM are placed on an open platform at 6 m above the ground – no definite conclusion is possible given the amount of data.

### 3.4 Measurements at Dome C

Dome C is one of the summits on the Antarctic plateau with altitude 3235 m. The station, which is jointly operated by France and Italy, is located 1100 km inland from the French research station Dumont Durville and 1200 km inland from the Italian Zuchelli station. Dome C is known as a site with low wind speeds at high altitudes. Because of its elevated location and its relative distance from the edges of the Antarctic Plateau, Dome C does not experience the katabatic winds characteristic of the coastal regions of Antarctica. Hence the coherence times could be particularly high. Lawrence et al. [46] have, during the Antarctic night, determined high-altitude turbulence parameters that are 2 to 3 times better than at mid-latitude sites. Accordingly, they concluded that an interferometer located on Dome C might allow projects that would otherwise require instruments in space. The value of  $\tau_0 = 7.9$  ms obtained by Lawrence et al. was derived from measurements with the MASS instrument and hence, it does not take into account the turbulence below 500 m (see the MASS website for corresponding calibration studies [68]). Measurements of  $\tau_0$  integrated over the whole atmosphere still need to be obtained.

In this context, similar measurements to those presented in Section 3.3, have been performed at Dome C, Antarctica, on January 31<sup>st</sup> and February 1<sup>st</sup> 2005 at daytime. For these measurements, *Canopus* was observed with a telescope of focal length 2.80 m and a primary mirror of 0.28 m, placed 3.5 m above the ground. The entrance pupil was covered by a mask with two 0.06 m diameter circular openings and centers 0.20 m apart. The observational set-up, as well as a first qualitative data analysis has been presented in a previous article [41]. The observations – done with the available equipment – were both spatially and temporally under sampled. During six sequences out of nine, it was nevertheless possible to place a lower limit equal to 10 ms to the mean duration of correlation  $t_c$  of the fringe patterns. This was done by fitting an exponential curve onto the measured structure functions:

$$D_\phi(t) = D_\phi(t \gg t_c) \times (1 - \exp(-(t/t_c)^{-5/3})) \quad (3.11)$$

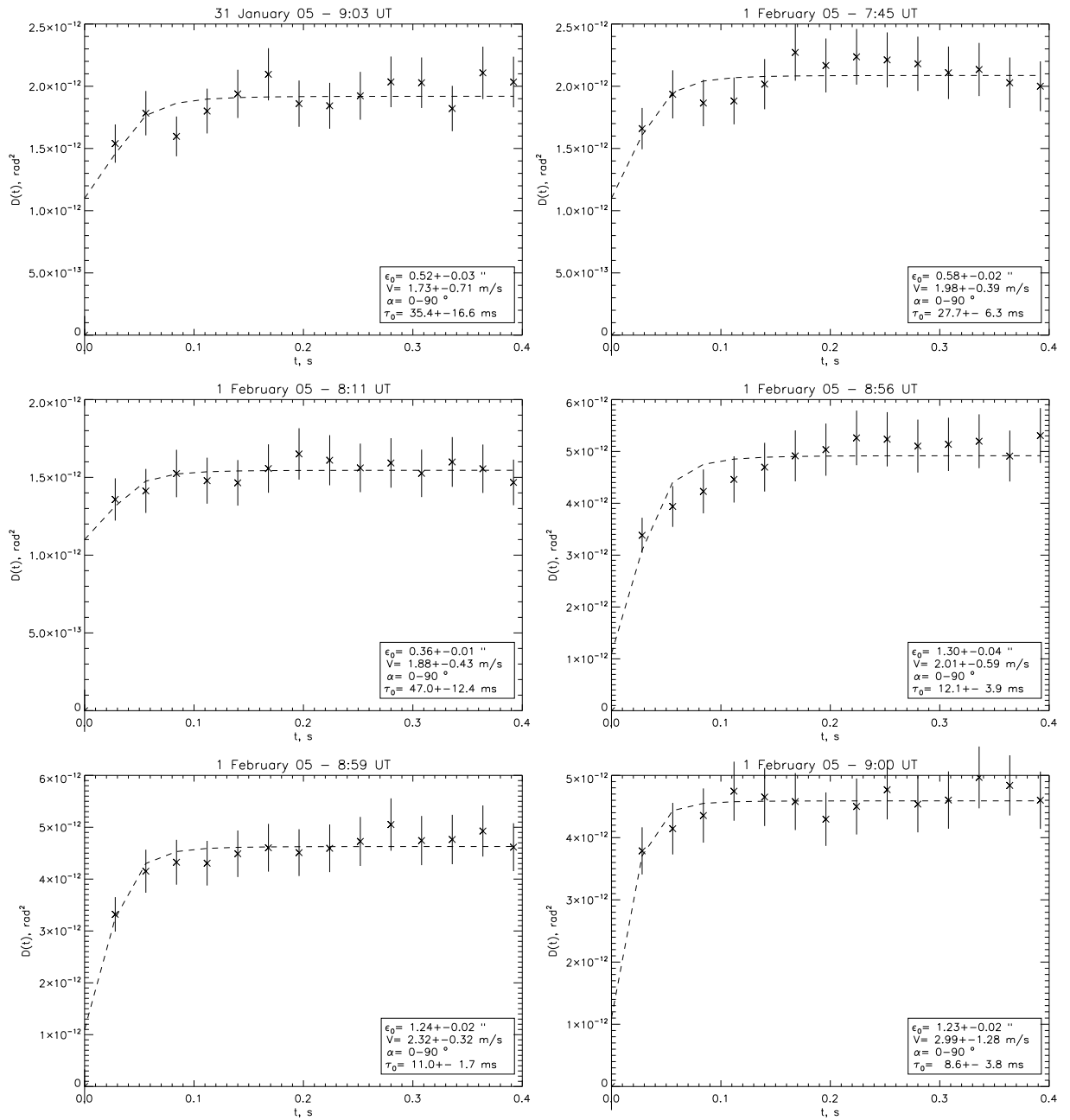


Figure 3.8: Atmospheric parameter values derived from measurements at Dome C.

In Section 3.2, the structure function has been related to the Fried parameter  $r_0$  and to the velocity vector  $\mathbf{V}$  in the case of a single turbulent layer, using the Kolmogorov model of atmospheric turbulence. This relation has been tested on well sampled piston scope measurements recorded at Paranal (see Section 3.3), and is now applied to re-analyze the data from Dome C.

We consider six out of nine sequences that were presented in the previous article. Images were taken every 28 ms, with exposure times of 1, 2 or 3 ms. Each sequence contains between 209 and 723 images and, thus, lasts roughly 5 to 20 s. Two sequences – recorded on February 1<sup>st</sup> at 7:49 UT and 9:41 UT – are not re-analyzed because the central positions of the fringe pattern and of the combined Airy discs are determined with too large uncertainties. In the previous article they were part of the three sequences during which the correlation time  $t_c$  was found to be less than 10 ms. For the third such sequence, recorded on January 31<sup>st</sup> at 9:07 UT, the fringe pattern can be fitted but since the structure function reaches its asymptotic value at the first measurement point, it can not be compared to a theoretical curve.

As seen on Figure 3.8, the structure functions reach their asymptotic value after the 4<sup>th</sup> to 5<sup>th</sup> data point. The fit involves three free parameters  $\epsilon_0, V, \alpha$  besides the white noise,  $K$ , that is approximately constant if the instrumental settings do not vary. The data obtained at Paranal from April 23<sup>rd</sup> to 24<sup>th</sup> yield:  $K = (3.2 \pm 0.7) 10^{-14} \text{ rad}^2$ . To constrain the fit,  $K$  is therefore fixed to the value that optimizes the global result of the six fitting procedures:  $K = 1.1 \times 10^{-12} \text{ rad}^2$ .

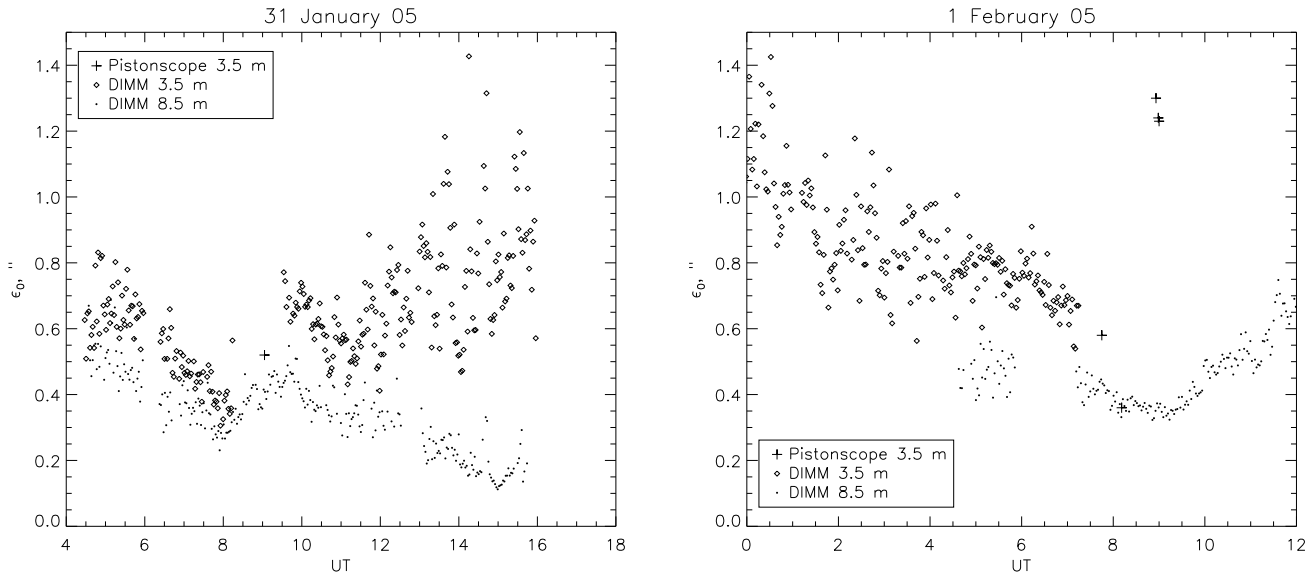


Figure 3.9: Seeing values measured at Dome C with the DIMM and the piston scope.

The derived parameter-values and uncertainties are indicated on Figure 3.8. As specified in Section 3.3, the uncertainties correspond to a two-fold increase in the squared deviation of the data points to the theoretic structure function. The values of the seeing are consistent with measurements by DIMM (Fig-

ure 3.9): The difference in the estimates by the piston scope and the DIMM at 8.5 m height, resembles the scatter between the values estimated by the DIMM instruments at 3.5 m and 8.5 m, and is due to ground layer turbulence. In line with our previous qualitative analysis, coherence times are found to lie above 10 ms during the periods when five of the nine sequences were recorded.

Note that the wind orientations are not constrained by the analysis. To derive – without continuous assessment of wind-direction profiles – more accurate values of  $\tau_0$ , a parameter needs to be measured that is independent of the wind orientation. We have pointed out what appears to be a suitable new method in a previous article [42].

### 3.5 Conclusions

The atmospheric coherence time,  $\tau_0$ , is the crucial parameter for interferometers because it determines their sensitivity. Yet, a simple method is still lacking to monitor the coherence time at different sites, and to decide where the future large interferometers ought to be built. Does the piston scope fulfill this need? To answer that question, we have related the measured quantity to parameters of the Kolmogorov model of turbulence.

It was found that due to its sensitivity to the wind direction the piston scope can be used to assess the wavefront velocity and the coherence time if, and only if, the whole turbulence is displaced along a single direction. Since the single layer model is not a permanent feature on most sites, the estimation of the coherence time is insecure. This conclusion is supported by seven sequences of 1000 images, recorded with the piston scope at the observatory of Paranal in April 2005. To determine the coherence time for any kind of atmospheric turbulence, a rotationally symmetric set-up has been proposed [42] and first measurements are planned.

The measurements performed at Dome C have been analyzed using the method here presented. Within the uncertainties due to low samplings, seeing angles are derived that coincide with simultaneous DIMM measurements. Mean wavefront speeds are found to be remarkably low. In agreement with a first qualitative analysis [41], the corresponding coherence times are determined to be superior to 10 ms during five out of nine sequences.



## Chapter 4

# Atmospheric coherence times in interferometry: definition and measurement

A. Kellerer, A. Tokovinin, 2007, *A&A*, 461, 775–781

### Abstract

Current and future ground-based interferometers require knowledge of the atmospheric time constant  $t_0$ , but this parameter has diverse definitions. Moreover, adequate techniques for monitoring  $t_0$  still have to be implemented.

We derive a new formula for the structure function of the fringe phase (piston) in a long-baseline interferometer, and review available techniques for measuring the atmospheric time constant and the shortcomings.

It is shown that the standard adaptive-optics atmospheric time constant is sufficient for quantifying the piston coherence time, with only minor modifications. The residual error of a fast fringe tracker and the loss of fringe visibility in a finite exposure time are calculated in terms of the same parameter.

A new method based on the fast variations of defocus is proposed. The formula for relating the defocus speed to the time constant is derived. Simulations of a 35-cm telescope demonstrate the feasibility of this new technique for site testing.

## 4.1 Introduction

Astronomical sites for classical observations are characterized in terms of atmospheric image quality (seeing). For high-angular resolution techniques such as adaptive optics (AO) and interferometry, we need to know additional parameters. The atmospheric coherence time is one of these. Here we refine the definition of the interferometric coherence time, review available techniques, and propose a new method for its measurements.

The AO *time constant*,  $\tau_0$ , is a well-defined parameter related to the vertical distribution of turbulence and wind speed (Roddier [58]). To correct wave fronts in real time, a sufficient number of photons from the guide star is needed within each coherence area during time  $\tau_0$ . This severely restricts the choice of natural guide stars and tends to impose the complex use of laser guide stars (Hardy [30]). It is shown below that new, simple methods of  $\tau_0$  monitoring are still needed.

Modern ground-based stellar interferometers attain extreme resolution, but their sensitivity is limited by the atmosphere. Even at the best observing sites, such as Paranal in Chile, fast fringe tracking is not fully operative yet, and one therefore tends to employ exposure times that are short enough to “freeze” the atmospheric turbulence. The price is a substantial loss in limiting magnitude. It is hence important to measure the *time constant*,  $t_0$ , of the piston – i. e. the mean phase over the telescope aperture – at existing and future sites. However, the exact definition of  $t_0$  is not clear, any more than are methods to measure it. Do we need an interferometer to evaluate  $t_0$ ? Is  $t_0$  different from  $\tau_0$ ? Does it depend on the aperture size and baseline? We review various definitions of the interferometric time constant based on the piston *structure function* (SF), on the error of a fringe tracker, and on the loss of fringe contrast during a finite exposure time. It is shown that the piston time constant is proportional to the AO coherence time  $\tau_0$ , both depending on the same combination of atmospheric parameters.

During site exploration campaigns, one would like to predict the performance of large base-line interferometers, and it is desirable to do this with single-dish and, preferably, small telescopes. The existing techniques for  $\tau_0$  measurement are listed and a new method for site testing proposed.

## 4.2 Atmospheric coherence time in interferometry

### 4.2.1 Atmospheric coherence time $\tau_0$

First, we introduce the relevant atmospheric parameters and the AO time constant  $\tau_0$ . For convenience, we outline the essential formulae, but for the general background, we refer the reader to Roddier [58].

The spatial and temporal fluctuations of atmospheric phase distortion  $\varphi$  are usually described by the SF

$$D_\varphi(\mathbf{r}, t) = \langle [\varphi(\mathbf{r}', t') - \varphi(\mathbf{r} + \mathbf{r}', t + t')]^2 \rangle, \quad (4.1)$$

which depends on the transverse spatial coordinate  $\mathbf{r}$  and time interval  $t$ . The angular brackets indicate statistical average.

The atmosphere consists of many layers. The contribution of a layer  $i$  of thickness  $dh$  at altitude  $h$  to the turbulence intensity is specified in terms of  $C_n^2(h)dh$ , equivalently expressed through the *Fried parameter*:

$$r_{0,i}^{-5/3} = 0.423k^2 C_n^2(h)dh, \quad (4.2)$$

$k = 2\pi/\lambda$  being the wavenumber. The spatial SF in the *inertial range* (between inner and outer scales) is

$$D_\varphi(\mathbf{r}, 0) = 6.883 (|\mathbf{r}|/r_0)^{5/3}. \quad (4.3)$$

It is assumed that each layer moves as a whole with the velocity vector  $\mathbf{V}(h)$  (Taylor hypothesis). The temporal SF of the piston fluctuations  $D_{\varphi,i}(\mathbf{0}, t)$  in one small aperture due to a single layer is then equal to, the spatial SF at shift  $Vt$ ,

$$D_{\varphi,i}(\mathbf{0}, t) = 6.883 [V(h)t/r_{0,i}]^{5/3}. \quad (4.4)$$

Summing the contributions of all layers, we obtain

$$\begin{aligned} D_\varphi(\mathbf{0}, t) &= 2.910 t^{5/3} k^2 \int_0^{+\infty} V^{5/3}(h) C_n^2(h) dh \\ &= 6.883 (t\bar{V}_{5/3}/r_0)^{5/3} = (t/\tau_0)^{5/3}, \end{aligned} \quad (4.5)$$

where  $\tau_0 = 0.314 (r_0/\bar{V}_{5/3})$  is the AO time constant (Roddiier 1981) and the average wind speed  $\bar{V}_p$  is computed as

$$\bar{V}_p = \left[ \frac{\int_0^{+\infty} V^p(h) C_n^2(h) dh}{\int_0^{+\infty} C_n^2(h) dh} \right]^{1/p}. \quad (4.6)$$

The formulae are valid for observations at zenith. At angle  $\gamma$  from the zenith, the optical path is increased in proportion to the *air mass*,  $\sec \gamma$ , and the SF increases by the same factor. Further, the transverse component of the wind velocity changes. In the following, we neglect these complications and consider only observations at zenith, but the analysis of real data must account for  $\gamma \neq 0$ .

### 4.2.2 Piston time constant

In an interferometer with a large baseline ( $B \gg L_0$ , where  $L_0$ : turbulence outer scale) the phase patterns over the apertures are uncorrelated on short time scales. Thus, for a small time interval ( $t < B/V$ ), the SF of the phase difference  $\phi$  (do not confuse with the phase  $\varphi$ ) in an interferometer with two small apertures will simply be two times larger,  $D_\phi(t) = 2D_\varphi(0, t)$  (Conan et al. [17]). As a result the differential piston variance reaches  $1 \text{ rad}^2$  for a time delay  $t_0 = 2^{-3/5} \tau_0 = 0.66 \tau_0$ . Note that, in the case of smaller baselines and large outer scales – when the assumption  $B \gg L_0$  becomes invalid –  $D_\phi(t) < 2D_\varphi(0, t)$  and the resulting coherence time, accordingly, lies between  $0.66 \tau_0$  and  $\tau_0$ . Yet,  $B \gg L_0$  applies to the characterization of large baseline interferometers at low-turbulence sites.

When an interferometer with larger circular apertures of diameter  $d$  is considered, phase fluctuations are averaged inside each aperture. As shown later, for time increments smaller than  $d/V$ , the piston structure function is quadratic in  $t$  and is essentially determined by the average wave-front tilt over the aperture. The variance of the gradient tilt  $\alpha$  (in radians) in one direction is (Roddiier [58], Conan et al. [17], Sasiela [61])

$$\sigma_\alpha^2 = 0.170 \lambda^2 r_0^{-5/3} d^{-1/3}. \quad (4.7)$$

We write the piston SF in this regime as  $D_\phi(t) \approx 2 (k\sigma_\alpha Vt)^2$ , sum the contributions of all layers, and obtain the expression

$$D_\phi(t) \approx 13.42 (\bar{V}_2 t / r_0)^2 (r_0 / d)^{1/3} = (t / t_1)^2, \quad (4.8)$$

where the modified time constant  $t_1 = 0.273 (r_0 / \bar{V}_2) (d / r_0)^{1/6}$ . The analysis of the tilt variance with finite outer scale by Conan et al. [15] is applicable here. The finite outer scale reduces the amplitude of the tilt and hence increases the piston time constant, but this effect depends on the aperture size and is not very strong for  $d < 1 \text{ m}$ .

Note that for small time intervals there is a weak dependence of the SF on the aperture diameter. Also, the wind velocity averaging is slightly modified. However, the expressions for  $t_1$  and  $t_0$  produce similar numerical results as long as  $d/r_0$  is not too large. Thus, the system-independent definition of the AO time constant (4.5) also gives a good description of the temporal variations of the piston.

For time delays of approximately  $B/V$  and larger, the pistons on two apertures are no longer independent. However, estimates of the time interval over which the Taylor hypothesis is valid range from  $\sim 40 \text{ ms}$  (Schoeck & Spillar [63]) to several seconds (Colavita et al. [14]). Hence, at time intervals of 1 s or more, the Taylor hypothesis is insecure. Moreover, the finite turbulence outer scale reduces the amplitude of slow piston variations substantially. Here we concentrate only on rapid piston variations where our approximations are

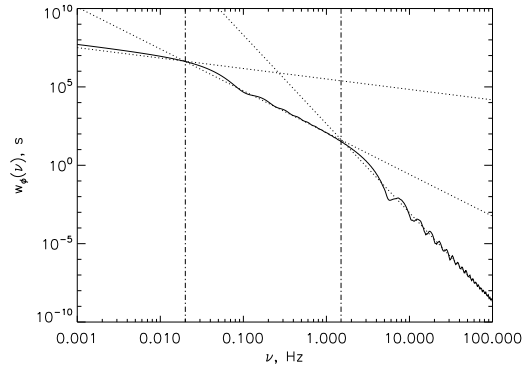


Figure 4.1: Theoretical temporal power spectrum of the fringe position at  $0.5\ \mu\text{m}$  wavelength. The two telescopes are separated by 100 m and have mirrors of 2 m diameter, the Fried parameter equals  $r_0=11$  cm, the wind vector makes an angle of  $\alpha = 45^\circ$  with the baseline,  $V = 10$  m/s. The vertical lines correspond to the frequencies:  $0.2 V/B$  and  $0.3 V/d$ . The asymptotic power laws are  $\nu^{-2/3}$ ,  $\nu^{-8/3}$ ,  $\nu^{-17/3}$  from lowest to highest frequencies.

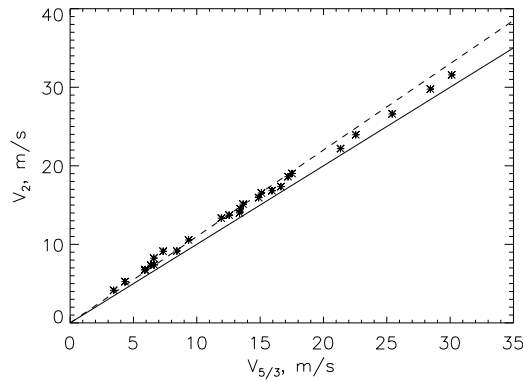


Figure 4.2: Relation between average wind velocities  $\bar{V}_{5/3}$  and  $\bar{V}_2$  for 26 balloon profiles at Cerro Pachon in Chile (Avila et al. [6]). The full line corresponds to equality, the dashed line is  $\bar{V}_2 = 1.1 \bar{V}_{5/3}$ .

valid.

### 4.2.3 Piston power spectrum and structure function

The temporal power spectrum of the atmospheric fringe position has been derived by Conan et al. [17]. Their result is reproduced in Appendix A with minor changes. The temporal piston power spectrum (4.18) produced by a single turbulent layer is represented in Fig. 4.1 for a specific set of parameters. Because of the infinite outer scale  $L_0$ , this example is not realistic for frequencies below  $\sim 1$  Hz. Moreover, as discussed in Sect. 4.2.2, Taylor's frozen flow hypothesis becomes invalid at low frequencies. Due to the infinite  $L_0$ , the asymptotic behavior of the spectrum, and in particular the cut-off frequencies, do not depend on the wind direction (Conan et al. [17]), whereas, in the real case of a finite outer scale, the cut-off frequencies are affected by wind direction, as described by Avila et al. [7]. Conan et al. [17] point out that changing

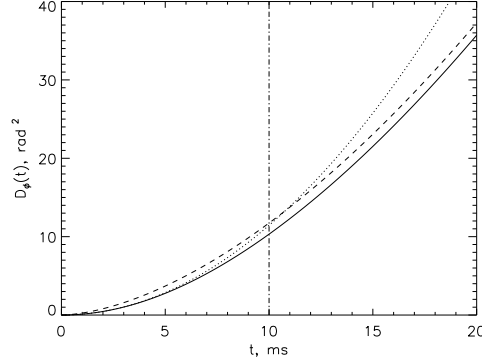


Figure 4.3: Structure function of the fringe position for an interferometer with mirror diameters  $d = 0.1$  m,  $r_0 = 11$  cm,  $V = 10$  m/s. The vertical line corresponds to  $t = d/V$ . For  $t < d/V$ , the SF is quadratic in  $t$  (dotted line), cf. Eq. 4.8. For longer time scales,  $D_\phi \approx 2D_\varphi$  (dashed line).

turbulence intensity and wind speed shift the spectrum vertically and horizontally, respectively, without changing the shape of the curve on the log-log plot. In observations with a small baseline ( $\sim 12$  m), the proportionality to  $\nu^{-2/3}$  at low frequencies and to  $\nu^{-8/3}$  at medium frequencies has actually been measured, e.g. by Colavita et al. [14].

Based on the piston power spectrum, we derive in Appendix A the new expression of the piston SF valid for time increments  $t < \min(B/\bar{V}, L_0/\bar{V})$ :

$$D_\phi(t) \approx 13.76 (\bar{V}t/r_0)^2 [1.17 (d/r_0)^2 + (\bar{V}t/r_0)^2]^{-1/6}. \quad (4.9)$$

As seen in Fig. 4.3, for  $t > d/\bar{V}$ , the piston averaging over apertures is not important and we obtain  $D_\phi = 2D_\varphi$  in agreement with heuristic arguments. For very short increments  $t \ll d/\bar{V}$ , (4.9) reduces to (4.8). The average wind speed is  $\bar{V} \approx \bar{V}_{5/3} \approx \bar{V}_2$ . The difference between  $\bar{V}_{5/3}$  and  $\bar{V}_2$  is indeed small (Fig. 4.2).

#### 4.2.4 Error of a fringe tracking servo

A fringe tracker measures the position of the central fringe and computes a correction. The actual compensation equals the integrated corrections applied after each iteration. Our analysis is similar to the classical work by Greenwood & Fried [28]. For a more detailed model that takes the effect of the finite exposure and response times of the phasing device into account, see the work by Conan et al. [16]. The error transfer function of a first-order phase-tracking loop equals

$$T(\nu) = i\nu/(\nu_c + i\nu), \quad (4.10)$$

where  $\nu_c$  is the 3 dB bandwidth of the system. The temporal power spectrum of the corrected fringe position is  $w_c(\nu) = |T(\nu)|^2 w_\phi(\nu)$ . The residual piston

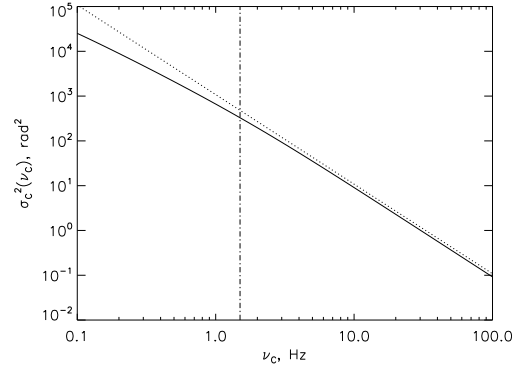


Figure 4.4: Variance of corrected fringe position as a function of the bandwidth frequency of the correction system. The parameters of the simulation are identical to those of Fig. 4.1. At frequencies higher than  $\nu_c = 0.3V/d$  (vertical line), the variance is approximated by  $(2\pi\nu_c t_1)^{-2}$  (dotted line).

variance characterizes the performance of the phasing device. This variance is shown in Fig. 4.4 as a function of  $\nu_c$  and is given by

$$\sigma_c^2(\nu_c) = \int_{-\infty}^{+\infty} \nu^2 / (\nu_c^2 + \nu^2) w_\phi(\nu) d\nu. \quad (4.11)$$

When  $\nu_c < 0.3V/d$ , the fringe tracker is too slow and leaves a large residual error; only fast trackers with  $\nu_c > 0.3V/d$  are of any practical interest. In this case, the dominant contribution to the residual variance in (4.11) comes from the frequencies just below  $0.3V/d$ , where the filter is approximated as  $(\nu/\nu_c)^2$ . Hence the residual variance is proportional to the variance of the piston velocity. There is a simple relation between the residual error of the fringe tracker and the structure function of the piston. For small arguments  $t$ , we can replace  $2[1 - \cos(2\pi\nu t)] \approx (2\pi\nu t)^2$  in the expression (4.19) for the phase SF. Then the residual error of the fast fringe tracker is simply

$$\sigma_c^2(\nu_c) \approx D_\phi[1/(2\pi\nu_c)] \approx (2\pi\nu_c t_1)^{-2}. \quad (4.12)$$

Thus, we have established that the error of the fast fringe tracker and the initial quadratic part of the piston SF are essentially determined by the variance of piston velocity which, in turn, depends on the tilt variance and the average wind speed  $\bar{V}_2$ .

#### 4.2.5 Summary of definitions and discussion

Table 4.1 assembles different definitions of the atmospheric coherence time. We have demonstrated that the time constant  $t_0$  of the piston SF is proportional to the AO time constant  $\tau_0$ . For small time increments, a slightly modified parameter  $t_1$  should be used.

A different, but essentially equivalent, definition of the piston coherence

Table 4.1: Definitions of atmospheric time constants

| Quantity of interest                         | Formula                                 | Time constant                                   |
|--|---|---|
| Phase SF                                     | $D_\varphi(t) = (t/\tau_0)^{5/3}$       | $\tau_0 = 0.314 r_0/\overline{V}_{5/3}$         |
| Piston SF, $t < d/V$                         | $D_\phi(t) = (t/t_1)^2$                 | $t_1 = 0.273 (r_0/\overline{V}_2)(d/r_0)^{1/6}$ |
| Piston SF, $t > d/V$                         | $D_\phi(t) = (t/t_0)^{5/3}$             | $t_0 = 0.66 \tau_0$                             |
| Piston variance during an exposure $t > d/V$ | $\sigma_\phi^2(t) = (t/T_0)^{5/3}$      | $T_0 = 2.58 \tau_0$                             |
| Phase tracker error, $v_c > 0.3 d/V$         | $\sigma_c^2(v_c) = (2\pi v_c t_1)^{-2}$ | $t_1$   |

time  $T_0 = 0.81 r_0/\overline{V}_{5/3} = 2.58 \tau_0$  has been given by Tango & Twiss [64] and reproduced by Colavita et al. [14]. It is the integration time during which the piston variance equals  $1 \text{ rad}^2$ . When fringes are integrated over a time  $T_0$ , the mean decrease in squared visibility equals  $1/e$ . Here we use the more convenient definition  $t_0 = 0.66 \tau_0$  based on the temporal SF and warn against confusion with Tango's  $T_0$ . The definition of  $T_0$  is valid only for  $T > d/V$ , while shorter integration times are of practical interest (see below).

The performance of the fringe-tracker in a long-baseline interferometer can be characterized by the atmospheric time constant  $t_1$  or, equivalently, by the average wind speed  $\overline{V}_2$ . The AO time constant  $\tau_0$  (or  $\overline{V}_{5/3}$ ) is also a good estimator of the piston coherence time, especially for small apertures  $d \sim r_0$ .

In order to reach a good magnitude limit, all modern interferometers have large apertures  $d > r_0$ . The atmospheric variance over the aperture is  $1.03 (d/r_0)^{5/3} > 1 \text{ rad}^2$  and has to be corrected by some means (tip-tilt guiding, full AO correction, spatial filtering of the PSF) even at short integration times. The temporal piston variance will also be  $>1 \text{ rad}^2$  on time scales of approximately  $r_0/\overline{V}$  and longer. Hence exposure times shorter than  $r_0/\overline{V}$  or fast fringe trackers are required in order to maintain high fringe contrast. In this regime, the relevant time constant that determines the visibility loss is  $t_1$ , rather than  $\tau_0$  and  $T_0$ .

All definitions of atmospheric time constants contain a combination of  $r_0$  and  $\overline{V}$ . As turbulence becomes stronger, the time constant decreases, although the wind speed may remain unchanged. Being less correlated, the parameters  $r_0, \overline{V}$  are thus more suitable for characterizing atmospheric turbulence than the parameters  $r_0, \tau_0$ . Astronomical sites with “slow” or “fast” seeing should be ranked in terms of  $\overline{V}$  rather than  $\tau_0$ . A fair correlation between  $\overline{V}$  and the wind speed at 200 mB altitude has been noted by Sarazin & Tokovinin [59].

## 4.3 Measuring the atmospheric time constant

### 4.3.1 Existing methods of $\tau_0$ measurement

Table 4.2 lists methods available for measuring the atmospheric coherence time  $\tau_0$  or related parameters. The 3rd column gives an indicative diameter of

Table 4.2: Methods of  $\tau_0$  measurement

| Method    | Measurables         | $d$ , m        | Problems                                  | Reference                |
|-----------|---------------------|----------------|---|--------------------------|
| SCIDAR    | $C_n^2(h), V(h)$    | $>1$           | Needs large telescope                     | Fuchs et al. [22]        |
| Balloons  | $C_n^2(h), V(h)$    | none           | Expensive, no monitoring                  | Azouit & Vernin [8]      |
| AO system | $r_0, \tau_0$       | $>1$           | Needs working AO                          | Fusco et al. [23]        |
| SSS       | $C_n^2(h), V(h)$    | $>0.4$         | Low height resolution                     | Habib et al. [29]        |
| GSM       | $r_0, V, \tau_{AA}$ | $4 \times 0.1$ | No obvious relation to $\tau_0$ and $t_1$ | Ziad et al [73]          |
| MASS      | $\tau_0^*$          | 0.02           | Biased (low layers ignored)               | Kornilov et al. [44]     |
| DIMM      | $r_0$               | 0.25           | Indirect $\tau_0$ estimate                | Sarazin & Tokovinin [59] |
| FADE      | $r_0, t_1$          | 0.35           | New method                                | This work                |

the telescope aperture required for each method. Short comments on each technique are given below.

SCIDAR (SCIntillation Detection And Ranging) has provided good results on  $\tau_0$ . It is not suitable for monitoring because manual data processing is still needed to extract  $V(h)$ , despite efforts to automate the process. Balloons provide only single-shot profiles of low individual statistical significance. The AO systems and interferometers give reliable results, but are not suitable for testing new sites or for long-term monitoring.

The methods listed in the next four rows of Table 4.2 all require small telescopes and can thus be used for site-testing. However, all these techniques have some intrinsic problems. SSS (Single Star SCIDAR) essentially extends the SCIDAR technique to small telescopes: profiles of  $C_n^2(h)$  and  $V(h)$  are obtained with lower height resolution than with the SCIDAR, and are then used to derive the coherence time. The GSM (Generalized Seeing Monitor) can only measure velocities of prominent layers after careful data processing. A coherence time,  $\tau_{AA}$  – which, however, does not have a similar dependence on the turbulence profile than  $\tau_0$  and  $t_1$  – is deduced from the angle of arrival fluctuations. MASS (Multi-Aperture Scintillation Sensor) is a recent, but already well-proven, turbulence monitor. One of its observables related to scintillation in a 2 cm aperture approximates  $\bar{V}_{5/3}$  (Tokovinin [68]), but this averaging does not include low layers and thus gives a biased estimate of  $\tau_0$ . An even less secure evaluation of  $\tau_0$  can be obtained from DIMM (Differential Image Motion Monitor) by combining the measured  $r_0$  with meteorological data on the wind speed (Sarazin & Tokovinin [59]).

We conclude from this brief survey that a correct yet simple technique for measuring  $\tau_0$  with a small-aperture telescope is still lacking. Such a method is proposed in the next section.

### 4.3.2 The new method: FADE

To measure the interferometric or AO time constant, we need an observable related to  $\bar{V}_2$  or  $\bar{V}_{5/3}$ . The atmosphere consists of many layers with different wind speeds and directions, so a true  $C_n^2$ -weighted estimator (4.6) is required.



Figure 4.5: Five consecutive ring images distorted by turbulence and detector noise. Each image is 16x16 pixels (13.8''), the average ring radius is 3'', the interval between images is 3 ms, the wind speed is 10 m/s.

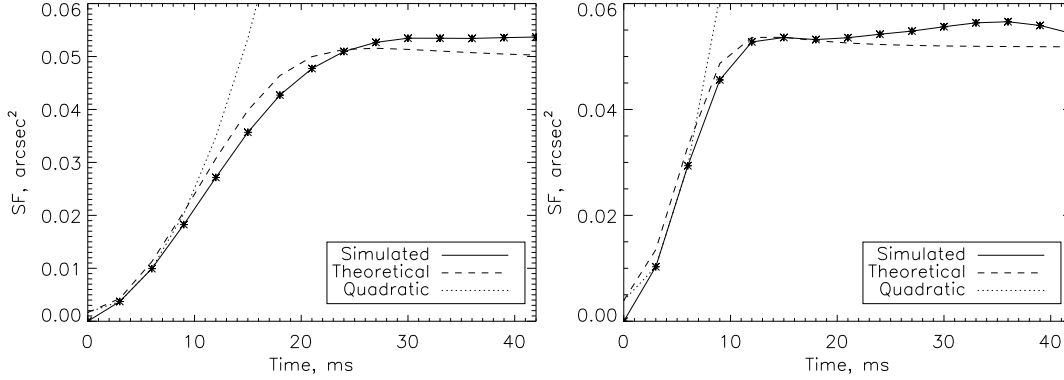


Figure 4.6: Temporal structure functions of simulated measurements of the ring radius for wind speeds 10 m/s (left) and 20 m/s (right) and  $r_0 = 0.1$  m seeing (time constants  $t_1$  of 3.36 and 1.68 ms, respectively).

Its response should be independent of the wind direction.

Wavefront distortions are commonly decomposed into Zernike modes (Noll [50]). The first mode, piston, cannot be sensed with a single telescope and the two subsequent modes, tip and tilt, tend to be corrupted by telescope vibrations. Of the remaining modes, the next three – defocus and two astigmatisms – have the highest variance and are the best candidates for measuring atmospheric parameters.

The total turbulence integral (or  $r_0$ ) is typically measured by the DIMM (Sarazin, & Roddier [60]). Lopez [49] tried to derive  $\tau_0$  from the speed of the DIMM signal, but this method did not prove to be practical. Because of its intrinsic asymmetry, DIMM does not provide an estimator of  $\bar{V}$  that is independent of the wind direction. On the other hand, the fourth Zernike mode (defocus) is rotationally symmetric.

We show in Appendix B that the variance of defocus velocity provides an estimator of the time constant  $t_1$ . The variance of the defocus itself gives a measure of  $r_0$ . Thus, we can measure both  $r_0$  and  $\bar{V}_2$ . The method is based on series of fast-defocus measurements, and we call it FADE (FASt DEfocus). The details of the future FADE instrument still need to be worked out and will be a subject of the forthcoming paper. Here we present numerical simulations to show the feasibility of this approach. We simulated a telescope of  $d = 0.35$  m diameter with a small central obstruction  $\epsilon = 0.1$ . A conic aberration was introduced to form ring-like images (Fig. 4.5). This configuration resembles a DIMM with a continuous annular aperture. The ring radius 3'' was chosen.

Monochromatic ( $\lambda = 500$  nm) images were computed on a  $64^2$  pixel grid from the interpolated distortions and binned into CCD pixels of  $0.86''$  size. We simulated photon noise corresponding to a star of  $R = 2$  magnitude and 3 ms exposure time (20 000 photons per frame) and added a readout noise of 15 electrons rms in each pixel.

The radius  $\rho$  of the ring image is calculated in the same way as standard centroids, by simply replacing coordinate with radius. The radius fluctuations  $\Delta\rho$  serve as an estimator for the defocus coefficient  $a_4$ . The radius change is approximated by the average slope of the Zernike defocus between inner and outer borders of the aperture:

$$\Delta\rho = C_\rho a_4 \approx [2\sqrt{3}(1 + \epsilon)/\pi (\lambda/d)] a_4. \quad (4.13)$$

The complex amplitude of the light distorted by two phase screens at 0 and 10 km altitude with combined  $r_0 = 0.1$  m was pre-calculated on a large square grid (15 m size, 0.015 m pixels). This distribution is periodic in both coordinates, and it was “moved” in front of the aperture in a helical pattern with the wind speed  $V$  to simulate the temporal evolution of the wave-front. The exposure time  $\Delta t = 3$  ms corresponds to a wave-front shift  $V\Delta t = 0.06$  m for  $V = 20$  m/s, such that the initial quadratic part of the defocus SF ( $\beta = 2Vt/d < 1$ ) extends only to  $\sim 3\Delta t$ .

Figure 4.6 shows the structure function,  $D_\rho$ , of the ring-image radius calculated from several seconds of simulated data. It contains a small additive component due to the measurement noise (in this case  $0.05''$  rms), which was determined from the data itself by a quadratic fit to the 2nd and 3rd points and its extrapolation to zero. The dashed lines are the theoretical SFs of defocus computed by (4.32) and converted into radius with the coefficient  $C_\rho$  (4.13). The slope between the second and third points of the simulated SF closely matches the analytical formula.

To measure the speed of defocus variations, it is sufficient to fit a quadratic approximation to the initial part of the measured SF,  $D_\rho(t) \approx at^2$ . Considering the noise, the best estimate of the coefficient  $a$  is obtained from the second and third points,  $a = [D_\rho(2\Delta t) - D_\rho(\Delta t)]/(3\Delta t^2)$ . This estimator is not biased by white measurement noise. Equating the quadratic fit to the theoretical expression  $D_\rho(t) = 0.0269(C_\rho t/t_1)^2$ , we get a recipe for calculating the time constant from the experimental data,

$$t_1 \approx 0.284 C_\rho \Delta t [D_\rho(2\Delta t) - D_\rho(\Delta t)]^{-1/2}. \quad (4.14)$$

Application of this formula to the simulated data gives  $t_1$  values of 3.88 and 2.20 ms for wind speeds 10 and 20 m/s, while the input values are 3.36 and 1.68 ms. Our simulated instrument slightly over-estimates  $t_1$  because the chosen exposure time of 3 ms is too long. Indeed, the error gets worse for a higher wind speed and disappears for  $V = 5$  m/s (true and measured  $t_1$  are 6.73 and 6.62 ms) or for a shorter exposure time. In the real situation of a multi-layer

atmosphere, the experimental SF will be the sum of the SFs produced by different layers. The contribution to the “jump” of the SF  $D_\rho(2\Delta t) - D_\rho(\Delta t)$  from fast layers will be reduced (in comparison with the quadratic formula) and will cause a bias in the measured  $t_1$ , increasing its value.

The crudeness of our simulations (discrete shifts of the phase screen, approximate  $C_\rho$ , etc.) also contributes to the mismatch. Averaging of the image during finite exposure time has not been simulated yet. The response and bias of a real instrument will be studied thoroughly by a more detailed simulation. However, the feasibility of the proposed technique for measuring  $t_1$  is already clear.

The next two Zernike modes number 5 and 6 (astigmatism) are not rotationally symmetric. However, the sum of the variances of the velocities of two astigmatism coefficients is again symmetric. In fact, it has the same spatial and temporal spectra as defocus, with a twice larger variance. Therefore, simultaneous measurement of the two astigmatism coefficients can be used to estimate the atmospheric time constant in the same way as defocus. Other measurables that are symmetric and have a cutoff at high frequencies can be used as well. However, defocus and astigmatism have the largest and slowest atmospheric variances making it easier to measure than other higher-order modes.

The FADE technique can be applied in a straightforward way to the analysis of the AO loop data, as a simple alternative to the more complicated method developed by Fusco et al. [23].

## 4.4 Conclusions

We reviewed the theory of fast temporal variations in the phase difference in a large-baseline interferometer. For a practically interesting case of large apertures  $d > r_0$ , the piston SF usually exceeds 1 rad<sup>2</sup> at the aperture crossing time  $t = d/\bar{V}$ . Hence, shorter times are of interest where the piston SF is quadratic (rather than  $\propto t^{5/3}$ ). The relevant atmospheric time constant is  $t_1$ . However, the standard AO time constant  $\tau_0$  also provides a good estimation of the piston coherence time. Both these parameters essentially depend on the turbulence-weighted average wind speed  $\bar{V}$ .

A brief review of available methods for measuring  $\tau_0$  shows the need for a simple technique suitable for site testing or monitoring, i.e. working on a small-aperture telescope. The FAst DEfocus (FADE) method proposed here fulfills this need. We argue that, for a given aperture size, this is the best way of extracting the information on  $\tau_0$ . The feasibility of the method is proven by simulation, which opens a way to the development of a real instrument. An instrument concept using a small telescope, some simple optics, and a fast camera will be described in a subsequent article.

## 4.5 Appendix A - Derivation of the piston structure function

The spatial power spectrum of the piston is derived from the spatial atmospheric phase spectrum (Roddier [58])

$$W_\varphi(\mathbf{f}) = 0.00969 k^2 \int_0^{+\infty} (f^2 + L_0^{-2})^{-11/6} C_n^2 dh, \quad (4.15)$$

where  $\mathbf{f}$  is the spatial frequency,  $L_0$  the turbulence outer scale at height  $h$ , and the other notations were introduced in Sect.4.2.1. We drop the explicit dependence of  $C_n$ ,  $L_0$ , and all following altitude dependent-parameters on  $h$ , to ease the reading of the formulae. The spatial filter that converts  $W_\varphi(\mathbf{f})$  into the piston power spectrum  $W_\phi(\mathbf{f})$  is

$$M^2(\mathbf{f}) = [2 \sin(\pi \mathbf{f} \mathbf{B}) A(\mathbf{f})]^2 \quad (4.16)$$

$$W_\phi(\mathbf{f}) = M^2(\mathbf{f}) W_\varphi(\mathbf{f}), \quad (4.17)$$

for a baseline vector  $\mathbf{B}$  and the aperture filter function  $A(\mathbf{f})$ . For a circular aperture of diameter  $d$ ,  $A(\mathbf{f}) = 2J_1(\pi f d)/(\pi f d)$  and  $f = |\mathbf{f}|$ . There  $J_n$  stands for the Bessel function of order  $n$ .

As usual, we assume that turbulent layers are transported with wind speed  $\mathbf{V}$  directed at an angle  $\alpha$  with respect to the baseline. The temporal power spectrum of the piston is then obtained by integrating in the frequency plane over a line displaced by  $f_x = \nu/V$  from the coordinate origin and inclined at angle  $\alpha$ . Let  $f_y$  be the integration variable along this line and  $f^2 = f_x^2 + f_y^2$ . The temporal spectrum equals

$$\begin{aligned} w_\phi(\nu) &= \frac{1}{V} \int_{-\infty}^{+\infty} W_\phi(f_x \cos \alpha + f_y \sin \alpha, f_y \cos \alpha - f_x \sin \alpha) df_y \\ &= 0.0388 k^2 \int_0^{+\infty} V^{-1} C_n^2 dh \int_{-\infty}^{+\infty} (f^2 + L_0^{-2})^{-11/6} \\ &\quad \times [\sin(\pi B f_x \cos \alpha + \pi B f_y \sin \alpha) A(f)]^2 df_y. \end{aligned} \quad (4.18)$$

We use the rotational symmetry of the aperture filter. This formula can be found in Conan et al. [17] in a slightly different form. The temporal power spectrum is defined here on  $\nu = (-\infty, +\infty)$  to keep the analogy with spatial power spectra.

The temporal structure function of the piston is

$$D_\phi(t) = \int_{-\infty}^{+\infty} 2[1 - \cos(2\pi t \nu)] w_\phi(\nu) d\nu. \quad (4.19)$$

For an interferometer with a large baseline  $B \gg d$ , the width of the aperture filter is much larger than the period of the  $\sin^2$  factor in (4.18). We can then replace the  $\sin^2$  with its average value 0.5. Assuming also that  $L_0 \gg d$ , we obtain an approximation for the piston power spectrum

$$w_\phi(\nu) \approx 0.0194 k^2 \int_0^{+\infty} V^{-1} C_n^2 dh \int_{-\infty}^{+\infty} A^2(f) f^{-11/3} df. \quad (4.20)$$

With this approximation,

$$\begin{aligned} D_\phi(t) &= 0.0388 k^2 \int_0^{+\infty} C_n^2 dh \int \int_{-\infty}^{+\infty} [1 - \cos(2\pi t f_x V)] A^2(f) f^{-11/3} df_x df_y \\ &= 0.244 k^2 \int_0^{+\infty} C_n^2 dh \int_0^{+\infty} [1 - J_0(2\pi t V f)] A^2(f) f^{-8/3} df. \end{aligned} \quad (4.21)$$

We used the relation (Gradshteyn & Ryzhik [26]):  $\int_0^{2\pi} \cos(2\pi z \cos \theta) d\theta = 2\pi J_0(2\pi z)$ . For a circular aperture of diameter  $d$ ,

$$D_\phi(t) = 1.641 k^2 d^{5/3} \int_0^{+\infty} C_n^2 dh K_1(2tV/d), \quad (4.22)$$

where the new dimensionless variables are  $\beta = 2tV/d$  and  $x = \pi f d$  and the function  $K_1(\beta)$

$$\begin{aligned} K_1(\beta) &= \int_0^{+\infty} [2J_1(x)/x]^2 x^{-8/3} [1 - J_0(\beta x)] dx \\ &\approx 1.1183 \frac{\beta^2}{(4.7 + \beta^2)^{1/6}}. \end{aligned} \quad (4.23)$$

The approximation of  $K_1(\beta)$  is accurate to 1% for all values of the argument and reproduces the analytic solutions of the integral for very large and very small  $\beta$ . For example, for large  $\beta$  the aperture filter tends to one; hence

$$\begin{aligned} K_1(\beta) &\approx \int_0^\infty x^{-8/3} [1 - J_0(\beta x)] dx \\ &= \pi / [2^{8/3} \Gamma^2(11/6) \sin(5\pi/6)] \beta^{5/3} = 1.1183 \beta^{5/3} \end{aligned} \quad (4.24)$$

(cf. Eq. 20 in Noll [50]). It follows that for  $t > d/\bar{V}$

$$D_\phi(t) \approx 13.77 (\bar{V}_{5/3} t/r_0)^{5/3} = (t/t_0)^{5/3}. \quad (4.25)$$

For  $t < d/\bar{V}$ ,  $K_1(\beta) \approx 0.864 \beta^2$  and

$$D_\phi(t) \approx 13.41 (\bar{V}_2 t/r_0)^2 (r_0/d)^{1/3} = (t/t_1)^2. \quad (4.26)$$

We recover (4.8). This proves that the initial part of the piston SF is indeed

defined by the overall wavefront tilts.

For a single turbulent layer, the piston SF is directly proportional to  $K_1(\beta)$ . Considering the small difference between two alternative definitions of the average wind speed,  $\bar{V}_{5/3} \approx \bar{V}_2 \approx \bar{V}$ , a good approximation for the SF at all time increments will be

$$D_\phi(t) \approx 3.88 (d/r_0)^{5/3} K_1(2t\bar{V}/d). \quad (4.27)$$

With the approximation (4.23), we finally obtain (4.9).

## 4.6 Appendix B - Fast focus variation

The temporal power spectrum of the Zernike defocus coefficient  $a_4$  is given in Conan et al. [17] as

$$w_4(\nu) = 0.00969 k^2 \int_{-\infty}^{+\infty} V^{-1} C_n^2 dh \int_{-\infty}^{+\infty} A_4^2(f) f^{-11/3} df, \quad (4.28)$$

where  $A_4(f) = 2\sqrt{3}J_3(\pi fd)/(\pi fd)$  is the spatial filter corresponding to the defocus on a clear aperture of diameter  $d$  (Noll [50]),  $f_x = \nu/V$ ,  $f^2 = f_x^2 + f_y^2$ , and we assume  $L_0 \gg d$ . This expression is similar to (4.20) but has a two times smaller coefficient and a different aperture filter. The variance of defocus is a function of the Fried parameter:

$$\begin{aligned} \sigma_4^2 &= \int_{-\infty}^{+\infty} w_4(\nu) d\nu \\ &= 0.00969 k^2 \int_0^{+\infty} C_n^2 dh \int \int_{-\infty}^{+\infty} A_4^2(f) f^{-11/3} df_x df_y \\ &= 0.0232 (d/r_0)^{5/3}. \end{aligned} \quad (4.29)$$

The variance of the defocus velocity has the following dependence on atmospheric parameters:

$$\begin{aligned} S_4^2 &= \int_{-\infty}^{+\infty} (2\pi\nu)^2 w_4(\nu) d\nu \\ &= 0.383 k^2 \int_0^{+\infty} V^2 C_n^2 dh \int \int_{-\infty}^{+\infty} f_x^2 A_4^2(f) f^{-11/3} df_x df_y. \end{aligned} \quad (4.30)$$

We set  $x = \pi fd$  and find:

$$\begin{aligned} S_4^2 &\approx 9.858 k^2 d^{-1/3} \int_0^{+\infty} V^2 C_n^2 dh \int_0^{+\infty} J_3^2(x) x^{-8/3} dx \\ &= 0.360 (\bar{V}_2/r_0)^2 (r_0/d)^{1/3} = 0.0269 t_1^{-2}. \end{aligned} \quad (4.31)$$

The transformation from (4.30) to (4.31) involves a coefficient increase by  $12\pi^{2/3}$ , while the definite integral is equal to  $\Gamma(8/3)\Gamma(13/6)/[2^{8/3}\Gamma^2(11/6)\Gamma(29/6)] = 0.01547$ .

The SF of defocus  $D_4(t)$  is derived in analogy with the piston SF, replacing the response  $A_1(f)$  for piston with  $A_4(f)$  for defocus. The coefficient is 2 times smaller because only one aperture is considered. In analogy with (4.22),

$$D_4(t) = 0.821 k^2 d^{5/3} \int_0^{+\infty} C_n^2 dh K_4(2tV/d), \quad (4.32)$$

$$\begin{aligned} K_4(\beta) &= 12 \int_0^{+\infty} [J_3(x)/x]^2 x^{-8/3} [1 - J_0(\beta x)] dx \\ &\approx \frac{0.0464\beta^2 + 0.024\beta^6}{1 + 1.2\beta^2 + \beta^6}. \end{aligned} \quad (4.33)$$

The approximation has a relative error less than 2% and correct asymptotes. Unlike  $K_1$ , the  $K_4$  function saturates for large arguments. Considering only the initial quadratic part of  $K_4$  at  $\beta \ll 1$ , we write for small time intervals

$$D_4(t) \approx 0.360 (t\bar{V}_2/r_0)^2 (r_0/d)^{1/3} = 0.0269 (t/t_1)^2. \quad (4.34)$$

## Chapter 5

# FADE, an instrument to measure the atmospheric coherence time

A. Tokovinin, A. Kellerer, V. Coudé du Foresto, 2007, submitted to A&A

### Abstract

A new method to derive the atmospheric time constant from the speed of the focus variations has been proposed by Kellerer & Tokovinin (2007). The instrument FADE implements this idea.

FADE uses a 36-cm Celestron telescope that is modified to transform stellar point images into a ring by increasing the central obstruction and combining defocus with spherical aberration. Sequences of such images are recorded with a fast CCD detector and are processed to determine the defocus and its variations in time, from the ring radii. The temporal structure function of the defocus is fitted with a model to derive the atmospheric seeing and time constant. The data reduction algorithm and instrumental biases are investigated by numerical simulation.

Bias caused by instrumental effects such as optical aberrations, detector noise, acquisition frequency etc. is quantified. The ring image must be well focused, i.e. must have a sufficiently sharp radial profile, otherwise scintillation seriously affects the results. An acquisition frequency of 700 Hz appears adequate. FADE was operated for 5 nights at the Cerro Tololo observatory in parallel to the regular site monitor. Reasonable agreement between the results from the two instruments has been obtained.

## 5.1 Introduction

The site- and time-dependent performance of telescopes, and especially of interferometers, can be characterized by the parameters *seeing*,  $\varepsilon_0$  (or, equivalently, the *Fried parameter*  $r_0 = 0.98\lambda/\varepsilon_0$ ), and the *coherence time*,  $\tau_0$ , that determines the required reaction speed of adaptive-optics (Roddier [58]). The variability of these parameters makes monitoring instruments essential. Seeing is usually measured with the Differential Image Motion Monitor, DIMM (Sarazin & Roddier [60]). However, a correct and simple technique to measure  $\tau_0$  is still lacking. At present this parameter is, therefore, variously inferred from the vertical profiles of wind speed and turbulence, from the temporal analysis of image motion, from scintillation, etc. (cf. the review in Kellerer & Tokovinin [42], hereafter KT07). In particular, a Multi-Aperture Scintillation Sensor, MASS (Kornilov et al. [44]) deduces the coherence time,  $\tau_0$ , from scintillation, but this method (Tokovinin [68]) is only approximate and has not, as yet, been verified by comparison with other techniques.

All current techniques having intrinsic limitations and shortcomings, a new method to measure the coherence time with a small telescope has recently been proposed in KT07. This method, termed FADE (FAst DEfocus), is based on recording and processing focus fluctuations produced by the atmospheric turbulence in a small telescope. The amplitude of defocus variation gives a measure of the seeing,  $\varepsilon_0$ , while the speed of the defocus change gives a measure of the time constant,  $\tau_0$  (cf. Section 5.3.4 for more details). FADE can be useful for site testing and monitoring, but its reliability has so far been demonstrated only by numerical simulation. Here we present an instrument implementing the new method.

The need for the new instrument is apparent from an overview of alternative ways to measure  $\tau_0$ . In principle, this quantity can be obtained from the temporal analysis of almost any quantity affected by turbulence, but all current approaches have weaknesses. Tilts, the easiest to measure, are typically corrupted by telescope shake and guiding errors, hence they are not suitable. The DIMM instrument is immune to the wind shake, but it is intrinsically asymmetric. An early attempt to extract  $\tau_0$  from the DIMM signal by Lopez [49] revealed the complexity of this approach and did not result in a practical instrument. If we discard tilts, the next second largest and slowest atmospheric terms are defocus and astigmatism. Defocus has angular symmetry and the rate of its variation is closely related to  $\tau_0$  (KT07). Thus, FADE, an instrument based on defocus analysis, is nearly optimal for  $\tau_0$  measurements. It is a full-aperture, i.e. symmetric, equivalent of DIMM and has some advantage over the latter even for classical seeing measurements.

The instrumental set-up is described in Section 5.2. Section 5.3 outlines the data analysis algorithm. In Section 5.4 the seeing and coherence time measured with FADE are checked for consistency and are compared to simultaneous data from the DIMM and MASS instruments. Section 5.5 contains conclusions and an outline of further work. Mathematical derivations and a detailed analysis

of instrumental biases by means of numerical simulation are given in Appendices 5.6–5.8.

## 5.2 The instrument

### 5.2.1 Operational principle

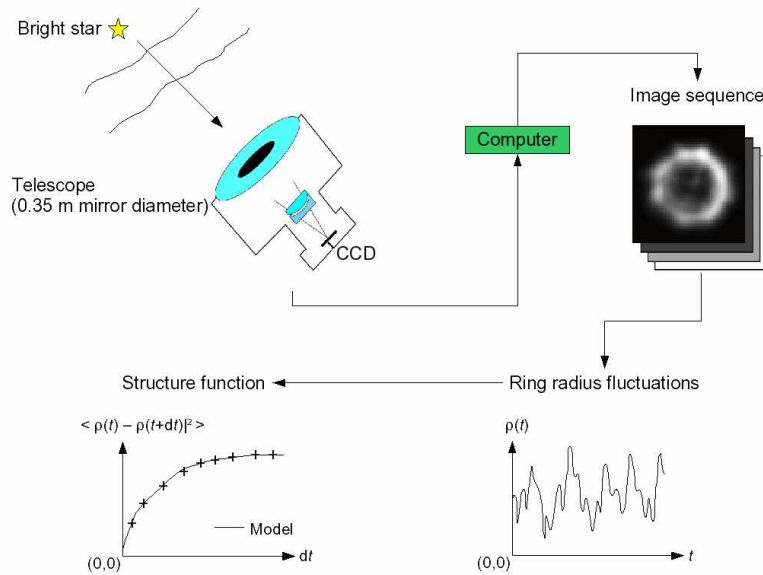


Figure 5.1: Overview of the FADE instrument and data analysis.

*Defocus* aberration can be measured with a wave-front sensor of any type or can be simply inferred from the size of a slightly defocused long-exposure stellar image (Tokovinin & Heathcote [67]). For FADE, a simple, fast, and accurate method is required. We chose to introduce a conic aberration into the beam in order to form a ring-like image. A small defocus slightly changes the radius of the ring. Ring-like images, “donuts”, are obtained by defocusing a telescope that has a central obstruction. However, unlike a donut, the ring is fairly sharp in the radial direction, which means that the determination of the ring radius is largely insensitive to intensity fluctuations (scintillation) at the telescope pupil. There is an inherent similarity between FADE and DIMM. In a DIMM, two peripheral beams are selected and are deviated by prisms to form an image of two spots. In FADE, the prisms are replaced by a cone and the whole annular aperture is used to form a ring-like image.

The ring images are recorded by a fast CCD detector and stored on a computer disk (Fig. 5.1). They are processed off-line to determine a temporal sequence of ring radii,  $\rho(t)$ . In order to estimate the atmospheric parameters  $\epsilon_0$  and  $\tau_0$ , the temporal structure function of the radius variations is then fitted to a model.

Atmospheric defocus fluctuations are fast: their temporal correlations decrease with a half-width 0.3 times the *aperture crossing time*  $t_{\text{cross}} = D/V$ , i.e. with 2.2 ms for a telescope diameter  $D = 0.36$  m and wind speed  $V = 50$  m/s (cf. Appendix B). To capture the focus variations of interest, an acquisition frequency  $\nu \geq 500$  Hz is required, which is attainable with today’s fast CCD detectors.

## 5.2.2 Hardware

Table 5.1: Components of the FADE instrument

| Component           | Description  |
|---------------------|--|
| Telescope           | <i>Celestron C14</i> , $D = 0.356$ m, $F = 3.910$ m                                  |
| Central obstruction | Circular mask of 150 mm diameter   |
| Aberrator           | PCX lenses ( <i>Linos 312321 &amp; 314321</i> ),<br>$d_L = 25$ mm, $f_L = \pm 50$ mm |
| Detector            | <i>Prosilica GE 680</i> , $640 \times 480$ ,<br>pixel $7.4 \mu\text{m}$ ( $0.39''$ ) |
| Interface           | Gigabit Ethernet IEEE 802.3 1000baseT  |
| Computer & OS       | <i>Dell D410</i> , <i>Windows XP</i>   |

We assembled the FADE prototype from readily available commercial components (Table 5.1). A 36-cm telescope was selected because the focus variations are too weak and too fast in a smaller telescope to be conveniently measured. Use of a fast CCD – GE 680 from *Prosilica* – is critical for the instrument, because it permits continuous acquisition with an image frequency 740 Hz when a 100x100 region-of-interest (ROI) is used. The signal is digitized in 12 bits. With the lowest internal gain setting, 0 dB, the conversion factor 2.86 ADU per electron, and the readout noise 38 ADU, i.e.  $13.4 e$ , were measured. According to the specifications, the maximum quantum efficiency (QE) is 0.5 electrons per photon at wavelength  $\lambda = 0.50 \mu\text{m}$  with a full-width half-maximum response of roughly  $\Delta\lambda = 0.25 \mu\text{m}$ . Indeed, the measured fluxes from stars correspond to the overall system QE of 0.35–0.40 electrons per photon, atmospheric and optical losses are included.

## 5.2.3 Optics

To create annular images, a conic aberration must be introduced into the beam. Conic lenses, *axicons*, have wide technical and research applications and are commercially available. For FADE the required conic aberration is so small that instead of an axicon a pair of conventional lenses can be used. The difference between quadratic (defocus) and conic aberrations on annular apertures with a large relative central obstruction  $\epsilon$  is already small. It can be reduced even further, if the next term, spherical aberration, is added in a suitable proportion. For a relative central obstruction  $\epsilon = 0.42$ , the mean squared deviation from a conic surface is minimized when  $a_{11} = -0.1 a_4$  (throughout

this article, the Zernike aberration coefficients are given in the Noll [50] notation). The ring image is then diffraction-limited if its radius is smaller than  $5''$ .

A small spherical aberration may already be inherent in the telescope or may be introduced by procedures such as refocusing from the nominal (design) position. To attain the desired aberration, we used an assembly of two simple plane-spherical lenses with equal but opposite curvature radii, which can be seen as a plane-parallel plate containing a meniscus-shaped void. The thickness of the meniscus is adjusted by changing the gap between the lenses. The positive lens is closer to the primary mirror, so that the meniscus curvature opposes the curvature of the wavefront. We used lenses with focal lengths  $f_L = \pm 50$  mm and a gap  $g = 0.7$  mm. When this element is placed at distance  $l = 93.5$  mm in front of the detector and the telescope is suitably refocused, a ring image of radius  $\rho \approx 53 \mu\text{m}$  is formed. Optical modeling in *Zemax* shows that this “aberrator” is reasonably achromatic. The spherical aberration is proportional to  $g l^6$ , therefore it can be adjusted over a wide range.

With the right combination of defocus and spherical aberrations, the wavefront is almost perfectly conic near the border of the aperture. To block the inner part of the wavefront, a central obstruction of 150 mm diameter, i.e. a relative diameter  $\epsilon = 0.42$ , was placed at the telescope entrance. The average ring image in the real FADE instrument (Fig. 5.2) shows marked aberrations other than conical, caused by the defects of optical surfaces and of alignment. Similar rings were reproduced in our simulations with a combination of coma and higher-order aberrations (cf. Sect. 5.8.1). We also fitted the Zernike aberrations directly using the donut method (Tokovinin & Heathcote [67]) and found that the coma coefficient could reach  $\sim 100$  nm (1.2 rad). Further, the defocus was not always kept at its optimum value required for sharp ring images. The effect of such aberrations is studied in Sect. 5.8.1 by simulation.

#### 5.2.4 Acquisition software

The GE 680 detector being relatively new, with no readily available software development kits as yet, we used the commercial software, *Streampix* from *Prosilica*. It provides all necessary functions for detector control and data storage in the FITS format, but the parameters need to be set manually at each acquisition, which requires constant attention. And they are not logged into the FITS headers or otherwise. Thus, *Streampix* is only a temporary solution. We checked that the image sequence is acquired at regular intervals, without time jitter. The detector was exposed for this purpose to a strictly periodic light signal at 10 Hz and a  $100 \times 100$  ROI was read at 400 Hz. The power spectrum of the flux calculated from these data is a narrow peak at  $(10.0 \pm 0.2)$  Hz without significant tails.

### 5.2.5 Observations

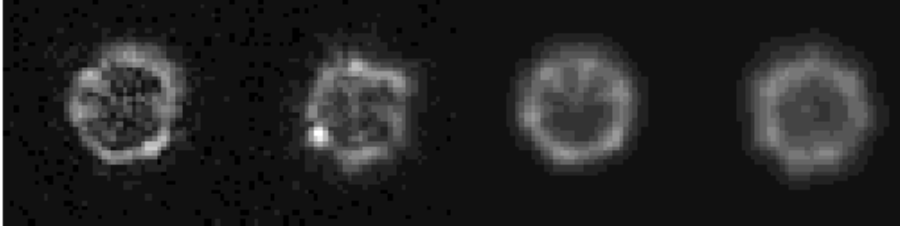


Figure 5.2: From left to right: Simulated ring image – Image of Sirius – Average of 1024 simulated images – Average of 1024 Sirius images. The sequence of Sirius images was recorded on Nov 2<sup>nd</sup> at 6:46 UT. The parameters for the data and simulations are given in Sec. 5.8.1.

The FADE instrument has been installed in the USNO dome of the Cerro Tololo Inter-American Observatory (CTIO) in Chile for the period October 27 to November 3, 2006. We pointed FADE at bright stars, *Fomalhaut* ( $\alpha$  PsA, A3V,  $m_V = 1.16$ ) in the evening, then *Sirius* ( $\alpha$  CMa, A1V,  $m_V = -1.47$ ). Figure 5.2 shows typical instantaneous and average images of Sirius, as well as simulated images. During our test run, the seeing was not very good, being roughly 1", and the turbulence in the high atmosphere was strong and fast, as evidenced by the MASS data.

## 5.3 Data analysis

A correct algorithm of data processing and interpretation is critical to derive the atmospheric parameters  $\varepsilon_0$  and  $\tau_0$ . We selected carefully the most robust method of calculating atmospheric defocus from the ring-like images and studied by numerical simulation the influence of various instrumental effects and of optical propagation on the results (Appendix 5.8).

### 5.3.1 Estimating the ring radius

The center of gravity of the image ( $x_c, y_c$ ) is calculated by the usual formula

$$x_c = \sum_{l,k} x_{l,k} I_{l,k} / \sum_{l,k} I_{l,k} \quad \text{and} \quad y_c = \sum_{l,k} y_{l,k} I_{l,k} / \sum_{l,k} I_{l,k}. \quad (5.1)$$

The ring radius  $\rho$  can then be estimated in a similar way, as the intensity-averaged distance from this center:

$$\rho = \sum_{l,k} r_{l,k} I_{l,k} / \sum_{l,k} I_{l,k}. \quad (5.2)$$

Here  $I_{l,k}$  is the light intensity at pixel  $(l, k)$ , and  $r_{l,k}$  is the distance of this pixel from the center. There are various caveats below the apparent simplicity of this procedure.

There is no unambiguous way to assign a center to a real, distorted and noisy ring image. A simple center-of-gravity is a very rough estimate of  $(x_c, y_c)$ , in particular it is affected by the intensity fluctuations in the ring due to scintillation. It is better to compute  $(x_c, y_c)$  with clipped intensities: 0 below a threshold and 1 above, the threshold being set safely above the background and its fluctuations. This initial estimate can be further improved by minimizing the intensity-weighted mean distance of the pixels from the ring, as described in Appendix A. However, small inaccuracies in the center determination do not affect the resulting radius critically and, in fact, we found the initial estimate to be adequate.

A second caveat concerns the choice of the pixels used for the radius estimate. A considerable fraction of pixels lie outside the ring in an empty area that contributes only noise. To reduce the noise with a minimal loss of information, we have restricted the pixels used in (5.2) to a mask of inner radius  $\bar{\rho} - \Delta\rho$  and outer radius  $\bar{\rho} + \Delta\rho$ , where  $\bar{\rho}$  is the average ring radius. We express the mask half-width  $\Delta\rho$  as a fraction  $\delta$  of the diffraction half-width of the ring,

$$\Delta\rho = \delta \lambda / [0.5 D (1 - \epsilon)]. \quad (5.3)$$

Figure 5.3 shows that a mask with  $\delta = 2$  would be good for an ideal, diffraction-limited ring. For a typical image sequence, however, the ring is widened by telescope aberrations and atmospheric distortions. So we set  $\delta = 4$  which covers the actual ring image with a sufficiently conservative, but still reasonable margin.

The simulations show that scintillation and aberrations add to the fluctuations of the estimated radii and thus bias the results of FADE. To reduce this effect, we sub-divide the ring into eight  $45^\circ$  sectors and – utilizing the same center estimate  $(x_c, y_c)$  – apply Eq. 5.2 to each sector separately, and then average the result. This reduces the effect of azimuthal intensity variations. An added advantage of the procedure is that the relative variance  $s$  of the total intensities in the sectors  $I_k$  with respect to their average  $\bar{I}_k$  serves as a measure of the scintillation, hence of the turbulence height,

$$s = \frac{1}{8} \sum_{k=1}^8 (I_k - \bar{I}_k)^2 / \bar{I}_k^2. \quad (5.4)$$

The method of calculating the ring parameters  $(x_c, y_c, \rho)$  is less rigorous than fitting a wave-front model directly to the image. The great advantage of the estimator (5.2), however, is its simplicity.

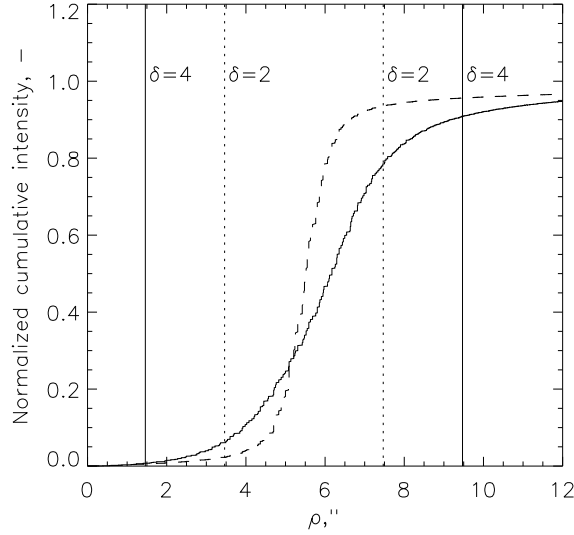


Figure 5.3: Total intensity inside concentric circles of radii  $\rho$  for the average of 1024 centered images. Full line: sequence of Fomalhaut images recorded on Nov 2<sup>nd</sup>. Dashed line: simulated diffraction-limited ring images (see Table 5.3).

### 5.3.2 Noise and limiting stellar magnitude

The errors of the radius estimates caused by photon and readout noise are obtained by differentiating Eq. (5.2) and using the independence of the noise in each pixel:

$$\sigma_{\rho, \text{noise}}^2 = \left( \frac{\sigma_{\text{ron}}}{N_{\text{ph}}} \right)^2 \sum_{l,k} (r_{l,k} - \bar{\rho})^2 + \frac{\delta_{\rho}^2}{N_{\text{ph}}}, \quad (5.5)$$

$$\delta_{\rho}^2 = \sum_{l,k} I_{l,k} (r_{l,k} - \bar{\rho})^2 / N_{\text{ph}}. \quad (5.6)$$

Here  $\sigma_{\text{ron}}$  is the rms detector noise,  $N_{\text{ph}} = \sum_{l,k} I_{l,k}$  is the total stellar flux in one exposure (both in electrons),  $\bar{\rho}$  is the average ring radius, and  $r_{l,k}$  is the distance of pixel  $(l, k)$  from the center, expressed either in pixels or arc-seconds. The rms ring-width  $\delta_{\rho}$  quantifies the ring sharpness which turns out to be critical for getting unbiased measurements with FADE (see 5.8.1). The summation is extended only over pixels inside the mask, as described in Section 5.3.1. We recognize a familiar sum of the readout noise (first term) and photon noise (second term), where the first term typically dominates. Eq. (5.5) does not account for such additional noise sources as scintillation, image distortion, etc.

Formula (5.5) is useful for predicting the limiting magnitude of FADE. A star of zero  $V$ -magnitude gives a flux  $N_{\text{ph}} \sim 6 \cdot 10^5$  photo-electrons in 1 ms exposure in our instrument. The rms noise on the radius estimate with plausible parameters ( $\rho = 5''$ ,  $\sigma_{\text{RON}} = 13$ ,  $\delta = 4$ ) is then about 2 mas. It will increase to

20 mas for a star with  $m_V = 2.5^m$  – still much less than the atmospheric signal. Hence, despite very short exposures, FADE is not photon-starved.

### 5.3.3 The response coefficient of FADE

The relation between the ring radius fluctuations  $\Delta\rho$  and the atmospheric defocus (Zernike coefficient  $a_4$ ) is intuitively clear. But what is the *exact* coefficient  $A$  in the formula  $\Delta\rho = Aa_4$ ? Recall that the atmospheric defocus  $a_4$  is related to the phase distortion  $\varphi(r)$  as

$$a_4 = \int z_4(r) \varphi(r) d^2r, \quad (5.7)$$

where  $r$  is the normalized coordinate vector on the pupil and  $z_4(r)$  is the orthonormal Zernike defocus given by Noll [50] for the circular aperture and in Fig. 5.4 for the annular aperture.

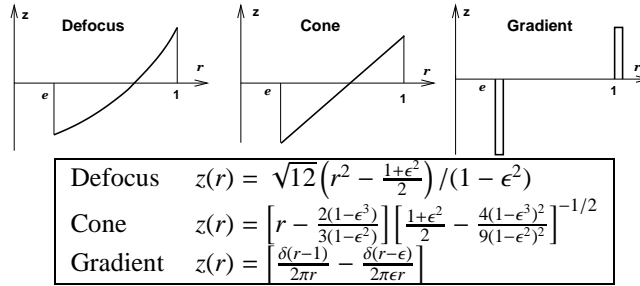


Figure 5.4: Response functions  $z(r)$  on annular aperture for Zernike defocus, conic aberration, and average radial gradient. The first two functions are normalized in the Noll [50] sense. The coefficients  $a_4$ ,  $a_c$  and  $a_g$  are calculated as integrals (5.7). Here  $\delta$  is the Dirac's delta-function.

A reaction of our simple radius estimator (5.2) to a small perturbation of phase and amplitude at the telescope pupil can be determined analytically (cf. Perrin et al. [54] for an example of similar analytics). It turns out that the response to a phase perturbation in the pupil plane is not exactly proportional to the Zernike defocus. Moreover, it depends on the adopted mask half-width  $\delta$ . For  $\delta \sim 1$ , the response resembles a cone, therefore FADE measures something similar to a conic aberration. On the other hand, for  $\delta \geq 2$  the computed ring radius is related to the average radial gradient of the wave-front, and therefore FADE measures the difference  $a_g$  between the phase averaged on the outer and inner edges of its annular aperture. Its response is further modified when the ring is distorted by aberrations. In this case, the radius estimate is sensitive to both amplitude and phase fluctuations. Although we developed a full analytical treatment of this problem, it is omitted here for the sake of simplicity.

The three quantities – Zernike defocus  $a_4$ , conic aberration  $a_c$ , and average phase gradient  $a_g$  – are similar, especially on the annular aperture (Fig. 5.4).

FADE measures yet something else, but its response is most closely approximated by  $a_g$  when the ring radius is calculated with a large mask width  $\delta$ . Let  $a_g$  be the average phase difference between the outer and inner borders of the aperture, the corresponding change of the angular ring radius is then

$$\Delta\rho = \frac{a_g \lambda}{\pi D(1 - \epsilon)}. \quad (5.8)$$

The Zernike defocus on the annular aperture is proportional to  $a_4 \sqrt{12}r^2/(1-\epsilon^2)$ , where  $r$  is normalized by the pupil radius. Hence,  $a_g = a_4 \times \sqrt{12}$  and the proportionality coefficient  $A$  follows from Eq. (5.8),

$$\Delta\rho = A a_4 = a_4 \frac{\lambda}{\pi D} \frac{\sqrt{12}}{1 - \epsilon}. \quad (5.9)$$

The atmospheric variance of the defocus  $a_4$  or gradient  $a_g$  on an annular aperture can be computed, as done by Noll [50] for a filled aperture. Alternatively, the variance of the ring radius may be directly written as

$$\sigma_\rho^2 = C_\rho(\lambda/D)^2(D/r_0)^{5/3} \quad (5.10)$$

in analogy with similar formulae for the gradient or Zernike tilt. Our numerical calculation for the average-gradient response (see Eq. 5.8) leads to an approximation valid for  $\epsilon < 0.6$  with an accuracy of  $\pm 7 \cdot 10^{-5}$ :

$$C_\rho \approx 0.03288 + 0.0503\epsilon - 0.05638\epsilon^2 + 0.04056\epsilon^3. \quad (5.11)$$

We studied the response of FADE by analytical calculation and numerical simulations and found that the exact coefficient  $C_\rho$  in Eq. 5.10 depends on all parameters of the instrument and data processing. A choice of  $\delta \geq 2.5$  ensures a relative stability of the response with respect to small aberration, propagation, etc. A small correction to the “ideal” response coefficient is finally determined by simulation (Sect. 5.8.1) and applied to the real data.

The lack of a unique, well-established coefficient relating measurements to atmospheric parameters may appear disturbing. However, a similar analysis applied to the classical DIMM instrument leads to the conclusion that its response, too, depends on the details of centroid calculation and, furthermore, is modified by propagation and optical aberrations. In this respect, FADE and DIMM are not different.

### 5.3.4 Derivation of the seeing and coherence time

We convert the measured ring radius into defocus using coefficient  $A$  (see Eq. 5.9) and calculate the temporal structure function (SF) of defocus  $D_4(t)$ ,

$$D_4(t) = \langle [a_4(t' + t) - a_4(t')]^2 \rangle. \quad (5.12)$$

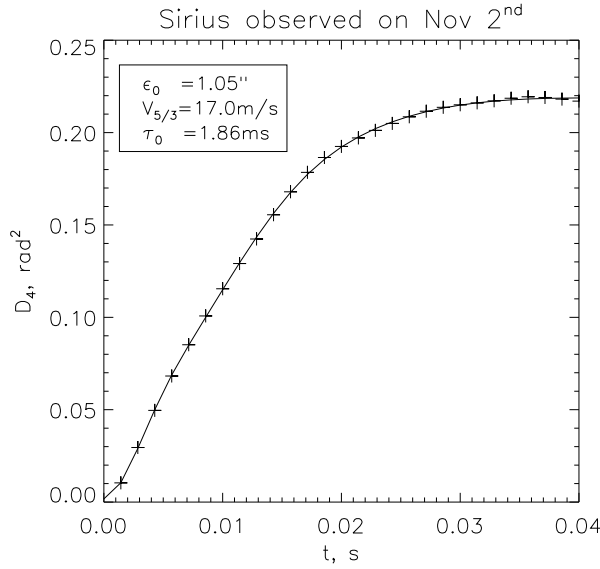


Figure 5.5: Structure function of focus variations measured at 700 Hz (crosses) fitted with a model of three turbulent layers (line).

A typical SF is plotted in Fig. 5.5.

A theoretical expression for the defocus SF has been derived in KT07. We generalize it to annular apertures in Appendix B. The initial, quadratic part of the SF is directly related to the combined time constant  $\tau_0$  of all turbulent layers. However, the acquisition frequency is not fast enough to capture the initial quadratic part of the SF extending only to time lags of  $< 0.1t_{\text{cross}}$ . In order to get two points on this part for a layer moving with  $V = 50$  m/s, a frame rate of  $\sim 3$  kHz would be required.

To overcome the sampling problem, we fit the initial part of the SF to a model of  $N$  turbulent layers with Fried parameters  $r_{0,i}$  and velocities  $V_i$ ,  $1 \leq i \leq N$ :

$$D_4(t > 0) = 1.94D^{5/3} \sum_{i=1}^N r_{0,i}^{-5/3} K_4(2tV_i/D, \epsilon) + \frac{2\sigma_{\rho, \text{noise}}^2}{A^2}, \quad (5.13)$$

where the function  $K_4(\beta, \epsilon)$  is defined in Appendix B and  $\sigma_{\rho, \text{noise}}^2$  is the noise of the radius estimate determined by Eq. 5.5. The adjusted parameters are  $r_{0,i}$  and  $V_i$ . As will be seen in Section 5.4.1, the estimate of  $\tau_0$  is independent of  $N$  if  $N \geq 3$ . Accordingly, a three-layer model is chosen for the data analysis (Fig. 5.5). We fit only the initial part of the SF, up to the time increment  $\Delta t$ . Its exact value is not critical, as long as it is large enough for unambiguous fitting of the parameters,  $\Delta t \nu > 2N + 1$ . For further data analysis, we set  $\Delta t = 40$  ms.

The atmospheric parameters  $(r_0, \bar{V}, \tau_0)$  are calculated as

$$r_0^{-5/3} = \sum_{i=1}^N r_{0,i}^{-5/3}, \quad (5.14)$$

$$(\bar{V}/r_0)^{5/3} = \sum_{i=1}^N (V_i/r_{0,i})^{5/3}, \quad (5.15)$$

$$\tau_0 = 0.314 r_0/\bar{V}. \quad (5.16)$$

The estimate of  $r_0$  is also obtained directly from the ring-radius variance  $\sigma_\rho^2$  by subtracting the noise,

$$\sigma_\rho^2 - \sigma_{\rho,\text{noise}}^2 = C_\rho(\lambda/D)^2(D/r_0)^{5/3}. \quad (5.17)$$

When the SF reaches its asymptotic value on time increments smaller than 40 ms, the same value of  $r_0$  is derived from the ring-radius variance (Eq. 5.17) and from the model (Eq. 5.14). The robustness of parameter estimates derived by model fitting has been confirmed by numerical simulation and by fitting alternative models to real data (Section 5.4.1).

## 5.4 Analysis of observations

Seeing and coherence time were estimated from all sequences of 4000 images recorded with FADE at Cerro Tololo between October 29<sup>th</sup> and November 2<sup>nd</sup>, 2006. In this Section, we check the FADE results for consistency and compare them with the MASS-DIMM.

### 5.4.1 Influence of instrumental parameters

During data acquisition, instrumental parameters were varied over a broad range to evaluate their effect on the results. Even though the non-stationarity of the atmosphere precludes direct comparisons, some conclusions can nevertheless be drawn.

The *ring sharpness*,  $\delta_\rho$ , has been identified as a major source of instrumental bias in FADE when significant high-altitude turbulence is present. In our data, most images have  $1'' < \delta_\rho < 1.5''$ , whereas a perfect diffraction-limited ring has  $\delta_\rho = 0.9''$ . Analysis of the average ring-images confirms that the optimum combination of defocus and spherical aberrations was not reached,  $a_4$  and  $a_{11}$  often being of the same sign rather than of opposite signs. For our data, the dispersion and mean of  $\tau_0$  increase when  $\delta > 1.25''$ , accordingly sequences with  $\delta_\rho > 1.25''$  are disregarded. Still, some bias caused by radially defocused images remains.

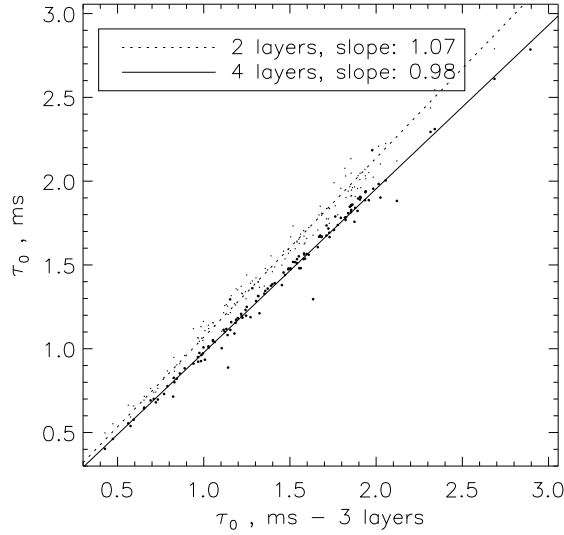


Figure 5.6: Coherence time derived from the recorded data by fitting a model with  $N = 3$  layers (x-axis) is compared to the coherence time derived with  $N = 2$  (dotted line) and  $N = 4$  (solid line) models.

As described in Sect. 5.3.4, the data are fitted to a model with a discrete *number of turbulent layers*,  $N$ . Which is the minimum value of  $N$  that permits a correct derivation of  $\tau_0$ ? Figure 5.6 shows that the  $\tau_0$  values obtained with 3 and 2 (resp. 4) layers differ on average by 7% (resp. 2%). An average difference of 2% is likewise obtained when comparing the estimates with of 3 and 5 layers. A 3-layer model is thus a good compromise enabling to fit the data with only six parameters.

The influence of the *acquisition frequency* on the measured coherence time is examined in Fig. 5.7. The data sequences recorded at frequencies  $\nu \geq 700$  Hz were re-analyzed considering every other image. The coherence time obtained with a slower  $\nu/2$  sampling is on the average 9% longer than with the fast sampling. This difference is reproduced by simulations if the turbulence is placed at 5 km altitude and if the ring-images are slightly defocused in the radial direction ( $a_{11}/a_4 \approx -0.07$  or  $-0.14$  instead of  $a_{11}/a_4 = -0.11$  corresponding to a sharp ring). The effect of temporal under-sampling is perceptible if the same comparison is repeated with sequences recorded at frequencies below 700 Hz: the number of points on the initial, increasing part of the SF is then not always sufficient to extract unambiguously the six fitted parameters and the coherence time is hence poorly constrained. To ensure a correct temporal sampling under fast turbulence, we disregard the sequences with  $\nu < 500$  Hz.

In line with the simulations, the coherence time estimates do not depend on the average *ring image radius*. Similarly, the parameter statistics seems unbiased by the *stellar flux* and by the *exposure time*. While the sequences of Sirius ( $m_V = -1.5$ ) and Fomalhaut ( $m_V = 1.2$ ) images were recorded with exposure times of  $dt < 0.5$  ms and  $1.0 < dt < 1.9$  ms respectively, no obvious difference

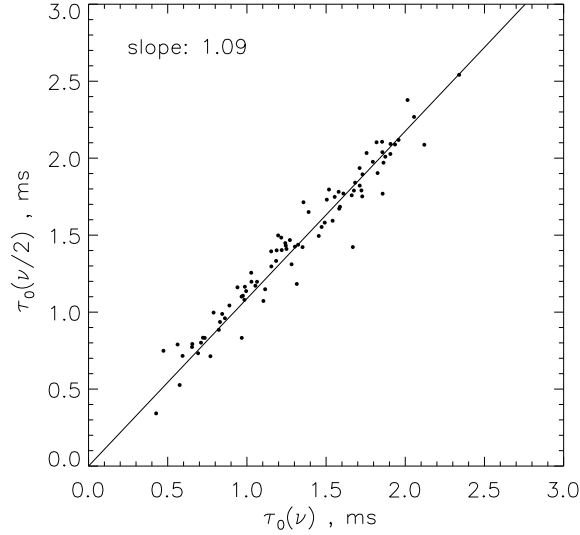


Figure 5.7: Coherence time derived from all sequences recorded with  $\nu \geq 700$  Hz when every image (x axis) and every other image (y axis) is considered.

exists between the mean and rms of the atmospheric parameters measured in terms of these two stars,

$$\begin{aligned} \epsilon_0^S &: (0.9 \pm 0.2)'' & \epsilon_0^F &: (0.8 \pm 0.1)'' \\ \tau_0^S &: (1.4 \pm 0.5) \text{ ms} & \tau_0^F &: (1.3 \pm 0.5) \text{ ms}. \end{aligned}$$

### 5.4.2 Comparison with MASS and DIMM

In this section, the seeing and coherence time obtained with FADE are compared to simultaneous measurements by the CTIO site monitor located at 10 m distance from FADE on a 6 m high tower. The monitor consists of a combined MASS-DIMM instrument fed by the 25-cm Meade telescope and looking at bright ( $V = 2^m \dots 3^m$ ) stars near zenith. Of particular interest here is the time constant  $\tau_0$  estimated by MASS from the temporal characteristics of scintillation by the method of Tokovinin [68]. This method is intrinsically biased because it does not account for the turbulence below  $\sim 500$  m. Moreover, it has been recently established by simulations that the coefficient used to calculate  $\tau_0$  in the MASS software must be increased by 1.27.<sup>1</sup> In the following, we correct  $\tau_0$  by applying this coefficient and including the contribution of the ground layer:

$$\tau_0^{-5/3} = (1.27 \tau_{\text{MASS}})^{-5/3} + 118 \lambda^{-2} V_{\text{GL}}^{5/3} (C_n^2 dh)_{\text{GL}}. \quad (5.18)$$

The turbulence integral in the ground layer,  $(C_n^2 dh)_{\text{GL}}$ , is computed from the difference between the turbulence integrals measured by DIMM (whole atmo-

<sup>1</sup>See the unpublished report by Tokovinin (2006) at <http://www.ctio.noao.edu/~atokovin/profiler/timeconst.pdf>

sphere) and MASS (above 500 m), while the ground layer wind speed,  $V_{GL}$ , is known from the local meteorological station. Even after correction by Eq. (5.18), the coherence time measured by MASS-DIMM should be taken with some reservation because it has never been checked against independent instruments and some bias is possible.

Figure 5.8 compares the estimates of  $\varepsilon_0$  and  $\tau_0$  obtained with FADE from October 29<sup>th</sup> to November 2<sup>nd</sup>, to the results of MASS-DIMM. We do not expect detailed correlation because the instruments were sampling different atmospheric volumes. As seen on Fig. 5.8, the seeing measurements are better correlated than the coherence times.

Statistically, it appears that FADE slightly under-estimates the seeing. This effect is reproduced with simulations of high-altitude turbulence if the ratio of spherical aberration to defocus  $a_{11}/a_4$  is set larger than its optimum value  $-0.1$  corresponding to sharp ring images. In this case, FADE also under-estimates the coherence time. The bias on  $\tau_0$  can however not be ascertained by Fig. 5.8 because the  $\tau_0$  estimates by MASS might likewise be biased.

## 5.5 Conclusions and perspectives

We have built a first prototype of the site-testing monitor, FADE, suitable for routine measurements of the atmospheric coherence time,  $\tau_0$ , as well as the seeing,  $\varepsilon_0$ . The instrument has been tested on the sky. Extensive simulations substantiate the validity of the FADE results and indicate potential instrumental biases. Our main conclusions are as follows:

- The sampling time of the image sequence must be a small fraction of the aperture crossing time  $t_{\text{cross}} = D/V$  ( $\sim 10$  ms for  $D = 0.36$  m and wind speed  $V = 36$  m/s). Sampling at  $\nu \geq 500$  Hz appears adequate under most conditions.
- The sharpness of the ring image in the radial direction does not bias the results when the turbulence is located near the ground. But it can bias both  $\tau_0$  and  $\varepsilon_0$  estimates when high layers dominate, and *strict control of the telescope aberrations is thus required*. The aberrations (hence the data validity) can be evaluated *a posteriori* from the average ring image. Real-time estimates of the ring radius  $\rho$  and width  $\delta_\rho$  are necessary to ensure good optical adjustment of the instrument.
- The FADE monitor with 36-cm telescope can work on stars as faint as  $m_V = 3^m$ .
- A simple estimator of the ring radius (Eq. 5.2) is adequate and robust, provided a wide enough mask around the ring ( $\delta \sim 4$ ) is used in the calculation.

- Moderate telescope aberrations such as coma are acceptable. The results are not critically influenced by small telescope focus errors.

The current FADE prototype stores all image sequences, leading to a large data volume; the data are processed off-line. While this procedure was necessary for the first experiments, on-line processing will be implemented in a definitive instrument. We have formulated and tested the data processing algorithm and can now develop adequate real-time software.

We plan to develop an improved version of FADE with real-time data analysis. It will be compared to simultaneous estimates of the atmospheric time constant from currently working adaptive-optics systems (Fusco et al. [23]) and/or long-baseline interferometers such as VLTI. Characterization of Antarctic sites for future interferometers is an obvious application for FADE.

*Acknowledgements: This work was stimulated by discussions with Marc Sarazin and other colleagues involved in site characterization. We acknowledge financial and logistic help from ESO in building and testing the first FADE prototype. We thank Cerro Tololo Inter-American Observatory for its hospitality and support of the first FADE mission.*

## 5.6 Appendix A – Estimator of the ring radius and center

The parameters of the ring-like image – its center  $(x_c, y_c)$  and radius  $\rho$  – can be derived by minimizing the intensity-weighted mean squared distance of the pixels from the circle,  $\delta_\rho^2$ :

$$\delta_\rho^2 = \frac{\sum_{l,k} I_{l,k} (r_{l,k} - \rho)^2}{\sum_{l,k} I_{l,k}}, \quad (5.19)$$

where  $r_{l,k} = [(l - x_c)^2 + (k - y_c)^2]^{0.5}$  is the distance of pixel  $(l, k)$  from the ring-center,  $(x_c, y_c)$ . Setting the partial derivative of  $\delta_\rho^2$  over  $\rho$  to zero, we obtain the radius estimator of Eq. 5.2. However, it still depends on the unknown parameters  $(x_c, y_c)$ . By use of Eq. 5.2, Eq. 5.19 is simplified to:

$$\delta_\rho^2 = \frac{\sum_{l,k} I_{l,k} r_{l,k}^2}{\sum_{l,k} I_{l,k}} - \left[ \frac{\sum_{l,k} I_{l,k} r_{l,k}}{\sum_{l,k} I_{l,k}} \right]^2. \quad (5.20)$$

This formula does not contain  $\rho$ . The center coordinates  $(x_c, y_c)$  can be derived by setting the partial derivatives of  $\delta_\rho^2$  over parameters to zero and solving the equations. We determine the center numerically by minimizing Eq. 5.20 and using the center-of-gravity coordinates as a starting point.

## 5.7 Appendix B – Structure function of atmospheric defocus

The temporal structure function of atmospherically-induced defocus variations – Zernike coefficient  $a_4$  in Noll's [50] notation – has been derived in KT07 for a filled circular aperture. Here we generalize it to an annular aperture. Without repeating the whole derivation, we refer the reader to KT07 and modify only the spatial spectrum of the Zernike defocus, taking into account the central obstruction ratio  $\epsilon$ . The resulting expression is

$$D_4(t) = 0.821 k^2 D^{5/3} \int_0^{+\infty} dh C_n(h)^2 K_4\left(\frac{2tV(h)}{D}, \epsilon\right), \quad (5.21)$$

$$K_4(\beta, \epsilon) = \frac{12}{(1 - \epsilon^2)^4} \int_0^{+\infty} dx x^{-8/3} [1 - J_0(\beta x)] \\ \times \left[ \frac{J_3(x)}{x} - \epsilon^4 \frac{J_3(\epsilon x)}{\epsilon x} + \epsilon^2 \frac{J_1(x)}{x} - \epsilon^2 \frac{J_1(\epsilon x)}{\epsilon x} \right]^2, \quad (5.22)$$

where  $k = 2\pi/\lambda$ ,  $J_n$  is the Bessel function of order  $n$ ,  $C_n(h)^2$  and  $V(h)$  are the altitude profiles of the refractive-index structure constant and wind speed, respectively. Considering the known relation between the turbulence integral and the Fried parameter,  $r_0^{-5/3} = 0.423 k^2 C_n^2 dh$ , we can also write the defocus SF produced by a single layer as

$$D_4(t) = 1.94 (D/r_0)^{5/3} K_4(2tV/D, \epsilon). \quad (5.23)$$

For calculating the function  $K_4$ , it is convenient to approximate the integral (5.22) by an analytical formula, as in KT07. We suggest the approximation

$$K_4(\beta, \epsilon) \approx \frac{C_1 \beta^2 + C_2 \beta^6}{1 + C_3 \beta^\alpha + \beta^6}, \quad (5.24)$$

where the coefficients are cubic polynomials of  $\epsilon$ :

$$C_i = C_{i,0} \sum_{k=0}^3 c_{i,k} \epsilon^k, \quad (5.25)$$

cf. Table 5.2. This approximation is valid for  $\epsilon < 0.6$  with a maximum relative error of less than 5% (3% for  $\epsilon = 0.42$ ) and correct asymptotes. The asymptotic value  $K_4(\infty, \epsilon) = C_2$  gives the focus variance on annular aperture, analogous to the Noll's coefficient. For  $\epsilon = 0$ , we get  $C_2 = 0.024$  and the focus variance coefficient of  $1.94 \times 0.024/2 = 0.0233$ , in agreement with the Noll's result.

The function  $K_4(\beta, \epsilon)$  reaches half its saturation value at  $\beta = 0.63$ , hence the atmospheric defocus correlation time is  $\sim 0.3D/V$ , as is well known in adaptive optics.

The above analysis is valid for instantaneous measurements, while in fact the defocus is averaged over the exposure time. This effect is usually important for

Table 5.2: Coefficients of (5.24)

| Param.   | $C_0$   | $\epsilon^0$ | $\epsilon^1$ | $\epsilon^2$ | $\epsilon^3$ |
|----------|---------|--------------|--------------|--------------|--------------|
| $C_1$    | 0.04642 | 1            | -0.182       | -2.431       | 2.028        |
| $C_2$    | 0.0240  | 1            | -0.017       | -3.619       | 2.833        |
| $C_3$    | 1       | 1.25         | 0            | 0            | 7.5          |
| $\alpha$ | 1       | 2.18         | -0.93        | 0            | 0            |

the DIMM. The time averaging can be included as an additional factor in the integral (5.22), as done e.g. in (Tokovinin [68]). We made this calculation and found that the initial, quadratic part of  $D_4(t)$  is reduced by 0.8 for an exposure time  $t_{\text{exp}} \sim 0.3D/V$ . Actual exposure times are much shorter, hence the bias caused by the finite exposure in FADE can be neglected. In the hindsight, this result could be expected: in order to follow the focus variations, we need such a fast sampling that the integration during the sampling period has a negligible effect.

## 5.8 Appendix C – Simulations

A new seeing monitor can be validated by comparing it with another, well-established instrument. In the case of FADE, however, there is no reliable comparison data on  $\tau_0$ . Instead, we simulated our instrument numerically as faithfully as we could and studied the influence of various instrumental and data-reduction parameters on the final result.

Table 5.3: Simulation parameters.

|                  | $N$  | $\nu$<br>Hz | $dt$<br>ms | $m_V$ | $\sigma_{\text{ron}}$<br>el. | $\rho$<br>" | $a_4$<br>rad | $a_7$<br>rad | $a_{11}$<br>rad | $a_{27}$<br>rad | $h$<br>km | $\varepsilon_0$<br>" | $\bar{V}$<br>m/s |
|------------------|------|-------------|------------|-------|------------------------------|-------------|--------------|--------------|-----------------|-----------------|-----------|----------------------|------------------|
| Fig. 5.2         | 1024 | 700         | 0.15       | -1.5  | 17                           | 3.8         | 0            | 0.7          | -0.75           | 0.3             | 13        | 1.05                 | 17               |
| Fig. 5.3         | 1024 | 700         | 0.15       | -1.5  | 17                           | 5.5         | 0            | 0            | 0               | 0               | 5         | 1.00                 | 17               |
| Eq. 5.26         | 1024 | 700         | 0.15       | -1.5  | 17                           | 3.8         | 0            | 0            | 0               | 0               | 10        | var.                 | 35               |
| Fig. 5.9 top     | 1024 | 700         | 0.15       | -1.5  | 17                           | 0           | 12           | 0.7          | var.            | 0.3             | 0         | var.                 | 35               |
| Fig. 5.9 bottom  | 1024 | 700         | 0.15       | -1.5  | 17                           | 0           | 12           | 0.7          | var.            | 0.3             | 5         | var.                 | 35               |
| Fig. 5.10 left   | 1024 | 700         | 1.4        | var.  | 17                           | 4           | 0            | 0            | 0               | 0               | 5         | var.                 | 35               |
| Fig. 5.10 middle | 1024 | 700         | 0.15       | -1.5  | 17                           | var.        | 0            | 0            | 0               | 0               | 5         | var.                 | 35               |
| Fig. 5.10 right  | 1024 | 700         | 0.15       | -1.5  | 17                           | 4           | 0            | var.         | 0               | 0               | 5         | var.                 | 35               |

### 5.8.1 Simulation tool

Our simulation tool generates the complex amplitude of the light field propagated through one or several phase screens with Kolmogorov spectrum. The screens are typically  $1024^2$  pixels with 1 cm sampling, i.e. about 10 m across. The resulting amplitude pattern is periodic, without edge effects. It is “dragged” in front of the simulated telescope with a chosen wind speed, wrapping around

edges in both coordinates and eventually covering the whole area. The monochromatic images created by a telescope with a perfect conic aberration of specified amplitude and, possibly, some additional intrinsic aberrations are re-binned into the detector pixels, distorted by readout and photon noise and fed to the data-analysis routine instead of the real data. Our tool has been verified by comparing with analytical results for weak perturbations and has been used for simulating other instruments such as DIMM and MASS. The limitations of this tool are: monochromatic light, single wind velocity for all layers, instantaneous exposure time.

We used two alternative, nearly equivalent ways of producing ring images. In the first method, a perfect conic wavefront was generated, and its amplitude was expressed as a ring radius  $\rho$ . In the second method, we do not apply conic aberration ( $\rho = 0$ ), but, instead, select a combination of defocus and spherical aberrations to mimic a real telescope. The sense of the Zernike coefficients  $a_4$  and  $a_{11}$  in both cases is distinct.

### Parameters of the simulations

For convenience, the simulation parameters are gathered in Table 5.3. These parameters are:

- number of images in the sequence  $N$ ,
- acquisition frequency  $\nu$ ,
- exposure time  $dt$ ,
- visual stellar magnitude  $m$ ,
- readout noise  $\sigma_{\text{ron}}$ ,
- conic aberration quantified by the average ring radius  $\rho$ ,
- amplitudes of the Zernike aberrations  $a_4$  (defocus),  $a_7$  (coma),  $a_{11}$  (spherical), and  $a_{27}$ ,
- altitude of the single turbulent layer  $h$ ,
- seeing  $\varepsilon_0$ ,
- wind speed  $\bar{V}$ .

Simulated ring images are compared in Fig. 5.2 to the images of Sirius recorded on Nov. 2<sup>nd</sup>. The combination of exposure time and magnitude results in the detected flux of  $3 \cdot 10^5$  electrons per simulated image, as in the actual images of Sirius. For this sequence, the estimated turbulence parameters equal:  $\varepsilon_0 = 1.05''$ ,  $\bar{V} = 17 \text{ m/s}$ ,  $\tau_0 = 1.86 \text{ ms}$  (Fig. 5.5). The same parameters are chosen for the simulated images. For best resemblance between simulated and real images, telescope aberrations are set to  $a_7 = 0.7 \text{ rad}$ ,  $a_{11} = -0.75 \text{ rad}$ ,

$a_{27} = 0.3$  rad. The turbulence is placed at 13 km altitude to reproduce the actual level of scintillation, evaluated from the intensity variance between ring sectors  $s = 0.011$  (cf. Eq. 5.4).

### Refining the response coefficient

The coefficient  $A$  relating radius variation to defocus is given by Eq. 5.9. Its actual numerical value, however, depends on the method of radius estimation, and in particular on the choice of the mask width  $\delta$ . For  $\delta = 4$ , we determined it to equal 1.077 by comparing  $\tau_0$  estimates from sequences of simulated images, to the nominal input value of  $\tau_0$  when Eq. 5.9 is used to relate the radius to defocus. The corresponding simulation parameters are summarized in Table 5.3. Thus,

$$\Delta\rho/a_4 = 1.077 \frac{\lambda}{\pi D} \frac{\sqrt{12}}{1 - \epsilon}. \quad (5.26)$$

### Instrumental biases

The data analysis relies on radius estimates that can be altered by telescope aberrations, scintillation, detector and photon noise, etc. Here we evaluate the instrumental bias by changing some parameters, while other parameters are fixed. In each case, a sequence of 1024 simulated images is generated with parameter values listed in Table 5.3. The wind speed is set to 35 m/s and the coherence time is then changed by modifying the seeing.

**Ring sharpness.** The ring is sharp in the radial direction when the wavefront is exactly conic. A good approximation of the conic wavefront is achieved by the optimum combination of defocus and spherical aberrations,  $a_{11} = -0.1 a_4$ . Here we explore the effect of unsharp ring images by setting  $a_4 = 12$  rad and varying  $a_{11}$  about its optimum value  $a_{11} = -1.2$  rad. Unlike the rest of the simulations, we do not apply conic aberration and set  $\rho = 0$ . Wrong values of  $a_{11}$  make the ring wider, as evidenced by its rms width,  $\delta_\rho$  (Eq. 5.6).

As seen in Fig. 5.9, the seeing and coherence-time estimates are biased in case of blurred rings and high-altitude turbulence. The sign of the bias depends on the sign of the deviation from the optimum  $a_{11}$ . When the turbulent layers are low, the scintillation is weak and the parameters are correctly derived even if the ring images are blurred.

To ensure a correct derivation under any atmospheric conditions, the ring width should be close to its diffraction-limited value  $\delta_{\rho,0}$ :

$$\delta_\rho < 1.2 \delta_{\rho,0} ; \quad \delta_{\rho,0} = 1.7 \lambda / [D(1 - \epsilon)], \quad (5.27)$$

where the coefficient 1.7 is determined from the width,  $\delta_\rho = 0.87''$ , of diffraction-

limited rings. Given the instrumental set-up, images should be rejected if  $\delta_\rho < 1''$ . However, all images recorded with the FADE prototype have  $\delta_\rho > 1''$ . Hence we apply a softer data-selection criterion:  $\delta_\rho < 1.25''$ , and note that the resulting estimates might still be biased if the turbulence was high.

**Stellar magnitude, ring radius and coma.** Figure 5.10 examines the stability of the seeing and coherence time estimates with respect to the stellar magnitude  $m_V$ , ring image radius  $\rho$ , and coma aberration  $a_7$ . In agreement with Eq. 5.5, estimates are correct up to stellar magnitudes 2–3. Spatial sampling and coma aberration do not affect the estimates if  $\rho \geq 2''$  (i.e. 5 pixels) and  $a_7 \leq 2$  rad.

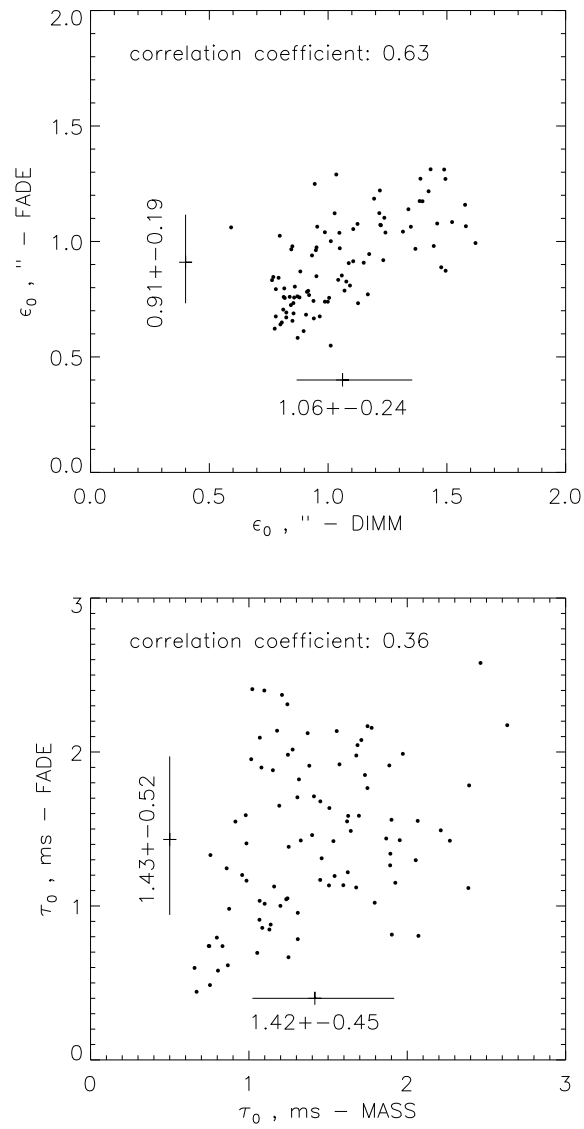


Figure 5.8: Seeing and coherence time measured with FADE between October 29<sup>th</sup> and November 2<sup>nd</sup>, compared to simultaneous measurements by the MASS-DIMM. The average values and standard deviations of parameters and the correlation coefficients are indicated.

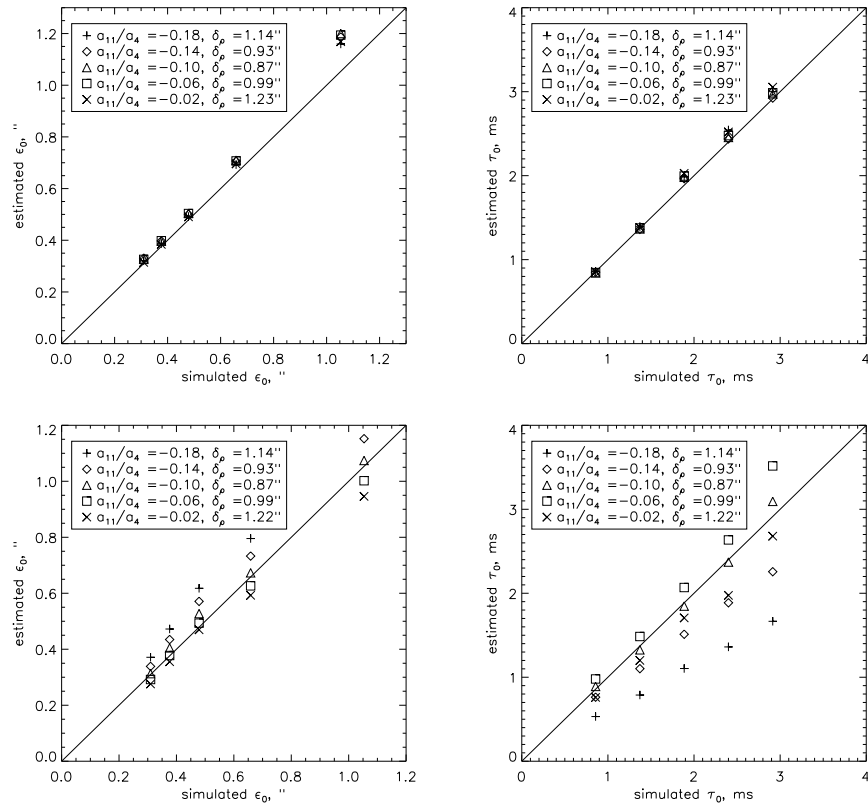


Figure 5.9: Influence of the ring sharpness – quantified in terms of the ring width  $\delta_p$  – on the seeing and coherence time estimates. Top – turbulence layer at ground level, bottom – turbulence layer at 5 km altitude. Simulation parameters are given in Table 5.3.

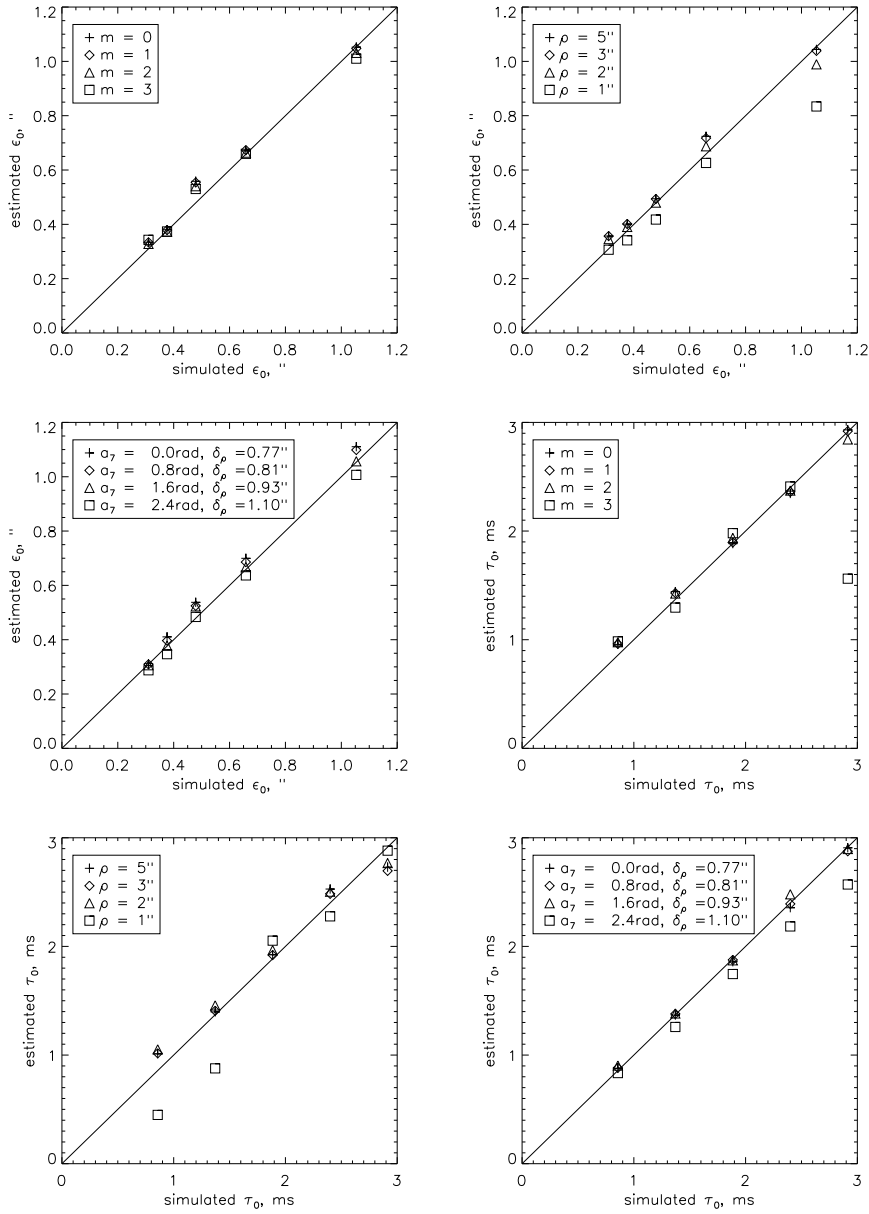


Figure 5.10: Dependence of the seeing and coherence time estimates on stellar magnitude  $m_V$ , mean ring radius  $\rho$  and coma aberration  $a_7$ . Simulation parameters are given in Table 5.3.

## Chapter 6

# Interferometric observations of the multiple stellar system $\delta$ Velorum

### 6.1 Introductory remarks to the article

New techniques for characterizing atmospheric turbulence and an improvement of the underlying theory are not an end in itself; for the astronomers they are of consequence where they facilitate and advance observational techniques. This chapter is meant to exemplify one area where interferometry is of particular importance.

A central issue in astrophysics, the theory of stellar evolution, has made considerable progress during the last century, but it is still incomplete and in many major aspects tentative. In the range of intermediate stellar masses, luminosities and ages, the theory is essentially consistent. But where the early and the final phases of stellar evolution are concerned, and also the extremely massive and the very low-mass stars, it tends to fail. Essential mechanisms remain largely unresolved. The energy transport out of the stellar centers, i.e. the efficiency and relative contribution of the two major mechanisms, conduction and convection, is reasonably known for a star of lower mass, such as our sun, but outside the normal range no reliable answers can currently be given.

The underlying problem is the impossibility to determine, with conventional techniques, the relevant parameters of a star. The mass, the chemical composition and the age of a star are the essential characteristics that determine its luminosity, size, heavy-element generation, and ultimately its fate. However, the stellar age can never be determined directly and the mass only under special conditions. These two parameters must, therefore, be derived from the luminosity, color or effective temperature by the use of relations obtained via evolutionary models.

To calibrate these relations, observations are required that are not possible with single stars, but can be made on physical binary and multiple-star systems, i.e., on star systems that are not associated by chance alignment, but are coupled by their gravitational forces. Such systems offer the possibility to determine directly the masses of stars that have been formed from the same pre-stellar cloud and are, thus, of same age. For a binary system the masses are inferred from Kepler's laws of motion, provided a number of parameters are obtained: the period, the semi-major axis and the eccentricity of the binary's orbit, and the ratio of the two stars' distances to their center of mass. These parameters are inferred from the stellar radial velocities via the Doppler shifts of spectral lines, and from the stars' positions via astrometric measurements.

Astrometry requires the stars to be sufficiently separated to be resolved as separate objects, i.e. the stars in binaries or multiple systems need to be reasonably widely separated. This, however, implies long orbital cycles and, accordingly, it obviates the quick acquisition of the relevant data. It is, thus, more desirable to work on close binaries or on the closely associated components in multiple stars, which usually are hierarchical, i.e. contain close binaries. But in all these cases, where small distances are involved, positions and separations need to be obtained through interferometric measurements. While – as documented in the most up-to-date 1999 revision of Tokovinin's catalogue [69] – speckle interferometry has been successful in past observations, long-baseline interferometry is required to deal with the close distances that are currently of much interest.

It must be noted that the true three-dimensional orbit can be reconstructed only if the interferometric measurements of the positions and the Doppler-measurements of the radial-velocity are combined. This is so, because the actual measured quantities are, first, the two-dimensional projections of the positions onto the celestial sphere and, second, the one-dimensional projection of the velocities along the line of sight. In practice, the measurements are often not yet sufficient to derive the two stellar masses without additional assumptions, such as for example the mass of the primary, which might be estimated indirectly from the luminosity or spectral type.

In an eclipsing binary, the orbit is oriented so that one star passes in front of the other as we observe the system. This not only reduces the problem to two dimensions, but also permits to readily derive several parameters from the temporal variations of the stellar flux: Twice during an orbital period the flux drops as one star eclipses the other. The relative durations of these eclipses and the relative durations between the eclipses are related to the eccentricity and the orientation of the orbit. Further, the ratio of the stellar surface brightnesses is obtained from the intensity ratio of the two eclipses. The orbital and physical properties of two eclipsing stars can therefore be determined far more precisely than with conventional binary systems.

The subsequent article exemplifies the use of interferometry in its application to  $\delta$  Velorum, which is prominent in the center of the Southern hemisphere, where it is going to be the polar star in the year 9000. While  $\delta$  Velorum contains

an eclipsing close binary, (Aa, Ab), which causes two substantial brightness reductions during the 45-days orbital period, it has, amazingly, been taken for a single star until recently. Only after  $\delta$  Velorum A was chosen as reference for the space probe Galileo, and after it failed as such, it was recognized to be a binary system. The subsequent article outlines the study that has come, by the use of interferometry, to some unexpected conclusions on the multiple-star system  $\delta$  Velorum.

# Interferometric observations of the multiple stellar system $\delta$ Velorum

A. Kellerer, M. G. Petr-Gotzens, P. Kervella, V. Coudé du Foresto, 2007,  
A&A, 469, 633-637

## Abstract

The nearby ( $\sim 24$  pc) triple stellar system  $\delta$  Velorum contains a close, eclipsing binary (Aa, Ab) discovered in 2000. Multiple systems provide an opportunity to determine the set of fundamental parameters (mass, luminosity, size, chemical composition) of coeval stars.

These parameters can be obtained with particular precision in the case of eclipsing binaries; so we exploited this potential for  $\delta$  Velorum's components (Aa, Ab).

We have analysed interferometric observations of the close binary (Aa, Ab), obtained with the VINCI instrument and two VLTI siderostats. The measurements, which resolve the two components for the first time, are fitted onto the simple model of two uniformly bright, spherical stars.

The observations suggest that Aa and Ab have larger diameters than expected for stars on the main sequence, hence they must be in a later evolutionary state.

## 6.2 Introduction

One of the fifty brightest stars on the sky, with a visual magnitude of  $m_V = 1.96$  mag (Johnson et al. [39]),  $\delta$  Velorum (HD 74956), is a multiple stellar system (e.g. Worley & Douglass [71]). But in spite of its brightness and proximity,  $\pi = (40.90 \pm 0.38)$  mas (Perryman et al. [55]), the issue of its composition remains unresolved. As early as 1847, Herschel published his detection of two faint visual companions,  $\delta$  Vel C and D, at a distance of  $69''$  from  $\delta$  Vel A. Another companion –  $\delta$  Vel B at the time separated by  $\sim 3''$  from  $\delta$  Vel A – was later discovered by Innes [37]. The separation  $0'.736 \pm 0'.014$  between components A and B appeared surprising when measured by *Hipparcos*, but it was explained later in terms of the orbit computation of Argyle et al. [4], which showed a highly elliptical orbit of component B with period  $P = 142$  yr. In 1979, preliminary results from speckle interferometry suggested yet another component of the system (Tango et al. [65]). This apparent companion was found at a separation of  $\sim 0'.6$  and was taken to be a further component, because the separation for star B at the time was believed to be  $\sim 3''$ .

By now, however, it seems very likely that the speckle observations resolved  $\delta$  Vel B; while there is still an unexplained disagreement for the position angle, the measured small separation does fit well with the orbital solution found by Argyle et al. [4]. As noted in earlier publications (Hoffleit et al. [35], Otero et al. [52]), the two stars that are currently termed  $\delta$  Vel C and D were taken to be associated with the pair AB because of seemingly similar proper motion. However, we have not found the source of the proper motion measurement of C and D. Finally, the most luminous component, A, was recently recognized to be a close eclipsing binary with a period  $T = 45.15$  days (Otero et al. [52]). Since then,  $\delta$  Vel has been classified as a quintuple stellar system.

This investigation is focussed on the bright eclipsing binary,  $\delta$  Vel A, but we also argue that  $\delta$  Vel C and D are not physically associated with  $\delta$  Vel A,B. While this makes  $\delta$  Vel a triple system, it takes little away from its challenging potential for obtaining important information on stellar evolution. As the inclination,  $i$ , of its orbital plane is constrained to be close to  $90^\circ$ , an eclipsing binary system provides one of the best means to obtain, in terms of the Kepler laws of motion, fundamental stellar parameters.

In this research note, we present the first interferometric observations of the eclipsing binary  $\delta$  Vel A, obtained with ESO's Very Large Telescope Interferometer (VLTI) and its "commissioning instrument" VINCI. The measurements resolve this binary system for the first time. They are analysed here with non-linear least-square fitting methods. We combine our interferometric results with existing photometric and spectroscopic observations, estimate some orbital parameters of the  $\delta$  Vel A binary system, and discuss the stellar properties of the individual components based on the results.

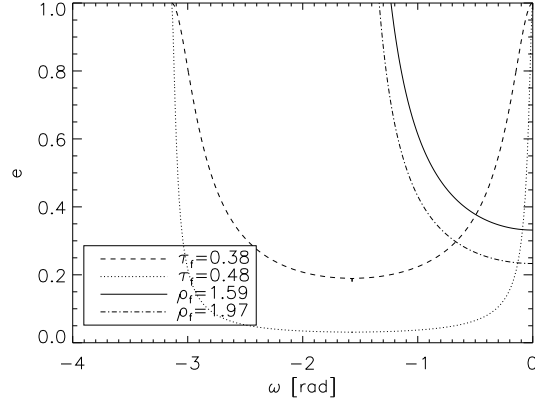


Figure 6.1: The angle,  $\omega$ , at primary eclipse and the eccentricity,  $e$ , as constrained by the fractional durations between the eclipses,  $\tau_f = 0.43 \pm 0.05$ , and the fractional durations of the eclipses,  $\rho_f = 1.78 \pm 0.19$ .

### 6.3 Characteristics of $\delta$ Vel A derived from previous measurements

In the following, *a priori* estimates of two orbital parameters for the  $\delta$  Vel (Aa-Ab) system are derived from the time interval between the eclipses and their durations. In subsection 6.3.2, stellar properties are then estimated from existing photometric and spectroscopic observations.

#### 6.3.1 Orbit orientation and eccentricity

As reported by Otero et al. [52] and Otero [53], the fractional orbital period from the primary to the secondary eclipse equals  $\tau_f = 0.43 \pm 0.05$ . The secondary eclipse was observed by the Galileo satellite in 1989, and its duration and depth were fairly precisely established as  $0.91 \pm 0.01$  days and  $\Delta m_{II} = 0.32 \pm 0.02$  (Otero [53]). The same spacecraft observed the primary eclipse several years later, although its measurements had become less accurate by then. The approximate duration and depth of the primary eclipse are  $0.51 \pm 0.05$  days and  $\Delta m_I = 0.51 \pm 0.05$  (Otero [53]). The ratio of durations thus amounts to  $\rho_f = 1.78 \pm 0.19$ . As will be seen now, the eccentricity,  $e$ , and the angle,  $\omega$ , between the semi-major axis and the line of sight, are constrained by  $\tau_f$  and  $\rho_f$ . The angle  $\omega$  is similar to, but must not be confused with, the more generally used parameter *longitude of periastron*.

The relative motion of the two stars  $\delta$  Vel Aa and Ab is taken to be independent of external forces, and the vector,  $\mathbf{s}$ , from Ab to Aa traces an elliptical orbit around Ab as a focal point. Because the photometric light curve indicates a total eclipse for  $\delta$  Vel A, the inclination of the orbit needs to be close to  $90^\circ$ . To simplify the equations, we assume  $i = 90^\circ$ , and Ab is taken to be the star with the higher surface brightness. During the primary eclipse, which is

deeper, Ab is thus eclipsed by Aa. The angle  $\theta$  of  $\mathbf{s}$ , also called the *true anomaly*, is zero at periastron and increases to  $\pi$  as the star moves towards apastron. The distance between the stars depends on  $\theta$  according to the relation:

$$s(\theta) = a(1 - e^2)/(1 + e \cos(\theta)), \quad (6.1)$$

where  $a$  denotes the semi-major axis. In line with Kepler's second law, the vector  $\mathbf{s}$  covers equal areas per unit time. The fractional orbital period to reach angle  $\theta$  is, accordingly:

$$\tau(\theta) = \frac{2}{A} \int_0^\theta s^2(\theta') d\theta' \quad (6.2)$$

$$= [2\arctan(f_1 \tan(\theta/2)) - f_2 \sin(\theta)/(1 + e \cos(\theta))]/2\pi, \quad (6.3)$$

where  $A = \pi a^2 \sqrt{1 - e^2}$  equals the area of the ellipse, and  $f_1 = \sqrt{(1 - e)/(1 + e)}$  and  $f_2 = e \sqrt{1 - e^2}$ .

During the primary eclipse, when the star with the lower surface brightness, Aa, covers Ab, the vector  $\mathbf{s}$  is directed towards Earth, and  $\theta$  equals  $\omega$ . During the secondary eclipse  $\theta$  equals  $\omega + \pi$ . Thus:

$$\tau_f = 0.43 \pm 0.05 \quad (6.4)$$

$$= \int_\omega^{\omega+\pi} d\theta/(1 + e \cos(\theta))^2 \quad (6.5)$$

$$= [\arctan(f_1 \tan((\omega + \pi)/2)) - \arctan(f_1 \tan(\omega/2)) + f_2 \sin(\omega)/(1 - e^2 \cos(\omega)^2)]/\pi, \quad (6.6)$$

which determines  $\omega$  for any given eccentricity,  $e$  (Fig. 6.1). The orbital velocity decreases as  $\theta$  goes from zero to  $\pi$ , i.e. from the periastron to the apastron. In the subsequent interval,  $\pi$  to  $2\pi$  (or  $-\pi$  to 0), it increases again. If the line of sight contained the orbital major axis, i.e.  $\omega = 0$  or  $\pi$ , the fractional duration between eclipses  $\tau$  would equal 0.5. Note that for such values of  $\omega$ , Eq. 6.6 is not defined, yet  $\tau$  tends towards 0.5 when  $\omega$  approaches 0, or  $\pi$ . If the line of sight contained the orbital minor axis, i.e.  $\omega = \pi/2$  or  $-\pi/2$ , the maximum and minimum values of  $\tau$  would be reached. Values of  $\tau$  less than 0.5 are thus associated with negative  $\omega$  values. Since the fractional orbital period from the primary to the secondary eclipse is 0.43, the angle  $\omega$  must lie between  $-\pi$  and 0. As Fig. 6.1 shows, the eccentricity needs to be larger than  $\approx 0.03$ .

On the other hand,  $\omega$  can be further constrained through the ratio of the eclipse durations as follows. The eclipse durations are inversely proportional to the product  $r d\theta/dt$  of radius and angular velocities during the eclipses. They are thus proportional to  $s(\theta)$ , and their ratio is:

$$\rho(\omega) = (1 - e \cos(\omega))/(1 + e \cos(\omega)). \quad (6.7)$$

Given  $\rho_f = 1.78 \pm 0.19$ , this leads to a second relation between  $e$  and  $\omega$ . As illustrated by Fig. 6.1, simultaneous agreement with both observed values  $\tau_f$

and  $\rho_f$  is reached only if  $e \in [0.23 - 0.37]$  and  $\omega \in -[0.1 - 0.7]$  rad.

### 6.3.2 Semi-major axis and stellar parameters

Orbital motion in the triple system  $\delta$  Vel(Aa+Ab+B) has recently been substantiated and analysed by Argyle et al. [4]. From position measurements taken over a period of roughly 100 years, the authors inferred a  $P = 142$  yr orbit for component B and deduced a total dynamical mass  $M(Aa) + M(Ab) + M(B) = 5.7^{+1.27}_{-1.08} M_{\odot}$ . Photometric and spectroscopic measurements of the individual components being few and partly inconclusive, individual mass estimates are still difficult.

*Hipparcos* measured an apparent magnitude of  $H_p = 1.991$  for  $\delta$  Vel A and  $H_p = 5.570$  for  $\delta$  Vel B. With the transformations given by Harmanec [?], the approximate Johnson V magnitudes are  $m_V = 1.99$  and  $m_V = 5.5$  for  $\delta$  Vel A and  $\delta$  Vel B, respectively. With the colours of the individual  $\delta$  Vel components being unknown, it needs to be noted that the uncertainty of  $m_V$  can be as high as  $\sim 0.07$  mag. Since  $\delta$  Vel is close ( $d = 24.45$  pc according to *Hipparcos*), no interstellar reddening towards the source needs to be assumed, making the absolute magnitudes are  $M_V \sim 0.05$  for  $\delta$  Vel A and  $M_V \sim 3.6$  for  $\delta$  Vel B.

Several authors have analysed spectra of  $\delta$  Vel A (e.g. Wright [72]; Alekseeva [3]; Levato [48]; Gray & Garrison [27]). Many of their measurements have probably included  $\delta$  Vel B, but its flux is too low to add a significant contribution. From the metal line ratios and Balmer line equivalent widths, all authors deduced either spectral type A0 V or A1 V. This being most likely an average classification of the two stars, Aa and Ab, one star should be slightly hotter and the other cooler than an A0/1V star. No signatures of a double-lined spectroscopic binary were reported in any of the spectroscopic observations.

Based on the spectrophotometric information referred to above and under the assumption that all  $\delta$  Vel components are on the main sequence, it is suggested that Aa and Ab have spectral type between A0V and A5V with masses in the range  $2.0\text{--}3.0M_{\odot}$ . Furthermore, it follows that B is an F-dwarf with mass about  $\sim 1.5M_{\odot}$ . This agrees reasonably well with the total dynamical mass derived by Argyle et al. [4].

An *a priori* estimate of the semi-major axis,  $a$ , of the Aa-Ab system is next derived from the mass sum of Aa+Ab ( $5 \pm 1 M_{\odot}$ ) and its orbital period ( $T = 45.150 \pm 0.001$  days), which leads to  $a = (6.4 \pm 0.5) \times 10^{10}$  m =  $0.43 \pm 0.04$  AU. If they are main sequence early A stars, Aa and Ab should have stellar diameters between  $1.7 - 2.4 D_{\odot}$ .

Finally, the depths of the eclipses can be used to constrain the surface brightness ratio  $\phi$  of the two eclipsing components,  $\delta$  Vel Aa and Ab,

$$1.28 \leq \phi = \frac{1 - 10^{-\Delta m_I/2.5}}{1 - 10^{-\Delta m_{II}/2.5}} \leq 1.67. \quad (6.8)$$

Table 6.1: Details of the VINCI measurements. The uncertainty on the phase determination equals  $\pm 0.002$ .

| Date      | Julian Date<br>- 2452700 | Phase | $V^2$<br>% | $\sigma_{V^2}$<br>% | $N_s$ |
|-----------|--------------------------|-------|------------|---------------------|-------|
| 21 Apr 03 | 50.628                   | 0.937 | 57.40      | 3.60                | 383   |
|           | 50.633                   | 0.937 | 54.20      | 3.60                | 298   |
|           | 50.639                   | 0.937 | 54.00      | 3.50                | 311   |
| 03 May 03 | 62.498                   | 0.200 | 27.54      | 0.66                | 96    |
|           | 62.502                   | 0.200 | 34.03      | 0.70                | 393   |
|           | 62.507                   | 0.201 | 43.40      | 2.20                | 260   |
|           | 62.512                   | 0.201 | 42.20      | 5.07                | 68    |
|           | 62.542                   | 0.201 | 13.37      | 0.45                | 80    |
|           | 62.545                   | 0.201 | 8.47       | 0.58                | 122   |
|           | 62.554                   | 0.202 | 5.06       | 0.17                | 356   |
| 10 May 03 | 69.551                   | 0.357 | 44.30      | 1.80                | 435   |
|           | 69.556                   | 0.357 | 52.20      | 2.00                | 446   |
|           | 69.561                   | 0.357 | 56.40      | 2.10                | 455   |
| 11 May 03 | 70.492                   | 0.377 | 8.30       | 0.45                | 258   |
|           | 70.506                   | 0.378 | 2.92       | 0.40                | 116   |
|           | 70.519                   | 0.378 | 1.30       | 1.40                | 45    |

## 6.4 VLT Interferometer/VINCI observations

### 6.4.1 Data description

During April-May 2003, the ESO Very Large Telescope Interferometer (VLTI) was used to observe the eclipsing binary  $\delta$  Vel (Aa+Ab) in the K-band at four orbital phases with the single-mode fiber-based instrument VINCI (Glinde-mann [25]; Kervella et al. [40]). The observations were performed with two siderostats, placed at stations B3 and M0, separated by 155.368 m. Table 6.1 lists the observing dates, the orbital phases of  $\delta$  Vel (Aa+Ab), the calibrated squared visibilities  $V^2$  and their standard deviations  $\sigma_{V^2}$ , and the number of accepted scans  $N_s$  (out of 500).

Every interferometric observation yields a fringe contrast or squared visibility,  $V^2$ , whose variations are due not only to interferometric modulation, but also to atmospheric and instrumental fluctuations. Accordingly the raw squared visibilities need to be calibrated by a reference star. To this purpose the observations of  $\delta$  Vel were combined with observations of HD 63744, a star of spectral type K0III, with an estimated diameter of  $1.63 \pm 0.03$  mas (Bordé et al. [10]). The interferometric measurements were then analysed by use of the VINCI data reduction pipeline, described in detail in Kervella et al. [40].

Additionally, the calibrated  $V^2$  values need to be corrected for the influence of the nearby component  $\delta$  Vel B. The diffraction on the sky (through an individual VLTI 0.4 m siderostat) of the fundamental fiber mode, which defines the interferometric field of view, is equivalent to an Airy disk with a  $1''.38$  diameter. At the time of the observations, Aa+Ab and B were separated by

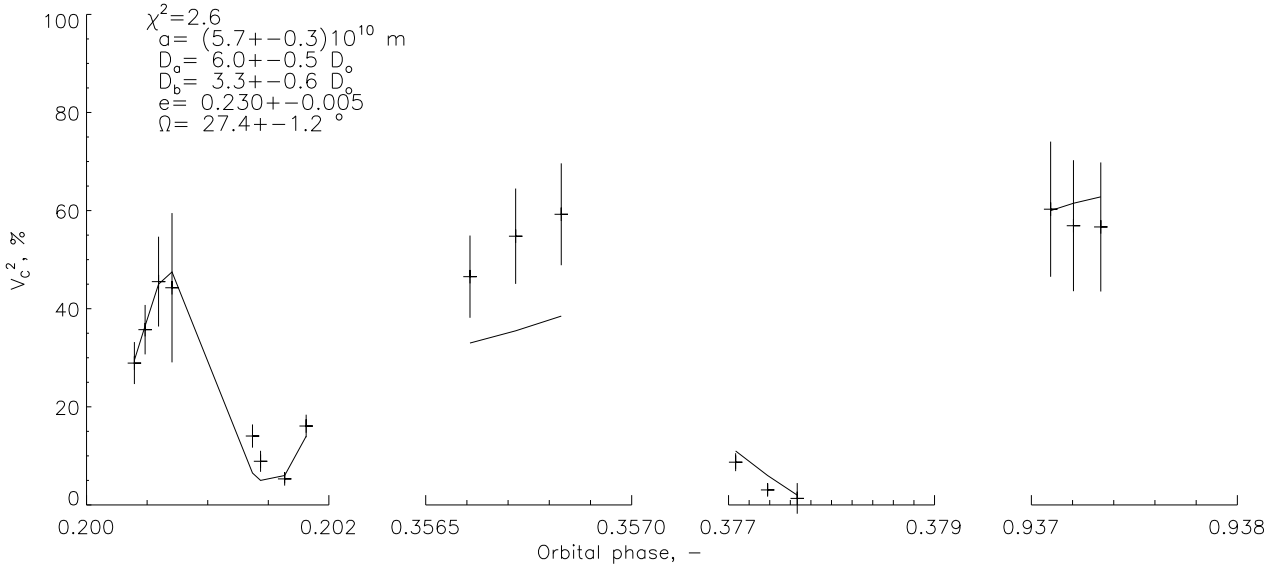


Figure 6.2: Corrected visibility values and standard deviation, compared to a model of two uniformly luminous, spherical stars. The parameter values of the best fit (solid line) are indicated in the upper left corner.

$\sim (1.0 \pm 0.3)''$ . Depending on atmospheric conditions, the interferograms are, therefore, contaminated by a random and time-varying fraction of light, i.e. an incoherent signal, from star B. The visibilities must, accordingly, be multiplied by a factor:

$$V_c = V \times (1 + I_B/I_{Aa+Ab}) = (1.05 \pm 0.05) \times V, \quad (6.9)$$

where  $I_B$  and  $I_{Aa+Ab}$  are the intensities collected by the interferometer from  $\delta\text{Vel} B$  and  $\delta\text{Vel} (Aa+Ab)$ . The value of  $I_B/I_{Aa+Ab}$  lies between 0 (no light from B) and  $10^{-\Delta m/2.5} = 0.09$  (star B is completely in the field of view), where  $\Delta m \sim 2.6$  equals the K-band magnitude difference between B and Aa+Ab.

## 6.4.2 Comparison to a model

The 17 visibility measurements,  $V_c^2$ , were fitted to a model of a binary system of two uniformly bright spherical stellar discs, observed at K-band with a filter of finite bandwidth. Five parameters of the binary model (stellar diameters  $D_a, D_b$ , position angle of the ascending node  $\Omega$ , semi-major axis  $a$ , eccentricity  $e$ ) were adjusted for optimum fit to the observations. The fitting procedure utilises a non-linear least-square algorithm (Markwardt [51]) that follows the direction of steepest descent of  $\chi^2$  in the parameter space,  $\chi^2$  being the reduced sum of squared deviations, i.e. the sum divided by the 13 degrees of freedom. To distinguish between local and absolute minima, the initial parameters were varied over the broad ranges of their potential values: The semi major axis,  $a$ , was considered between  $5.4 \cdot 10^{10}$  m and  $8.0 \cdot 10^{10}$  m, which corresponds to a total mass of Aa and Ab in the range 3 – 10  $M_\odot$ . As specified in Sect. 6.3,  $e \in [0.23, 0.37]$ . The stellar diameters were examined between 0.4 and 12.4 mas.

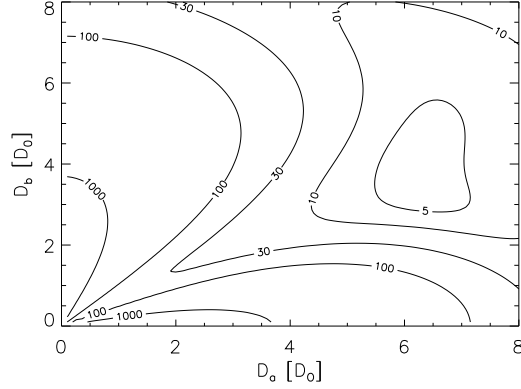


Figure 6.3:  $\chi^2$  as a function of the stellar diameters. The three other parameters of the model are set equal to:  $a = (5.7 \pm 0.3)10^{10}\text{m}$ ,  $e = 0.230 \pm 0.05$  and  $\Omega = 27.4 \pm 1.2^\circ$ .

These limits refer respectively to the resolution limit of the interferometer and to the Roche lobe volume diameter  $D_L$ . The latter is approximated to better than 1% by  $D_L/d \sim 12.4\text{mas}$  (Eggleton [20]). If one of the stars were to have a diameter larger than  $D_L$ , the system would be an interacting binary and the simple model of two spherical, uniformly bright stars would not apply. The position angle of the ascending node  $\Omega$ , measured from North to East, equals 0 if the projected orbital plane and the North-South axes are aligned. No previous measurement of  $\Omega$  exists, and the angles  $\Omega$  and  $\Omega + \pi$  cannot be distinguished through interferometric measurements; therefore,  $\Omega$  is considered between 0 and  $\pi$ . Varying the surface brightness ratio  $\phi$  over the range specified in Eq. 6.8 has virtually no effect on  $\chi^2$ ,  $\phi$  is so fixed at 1.46. Likewise, the period of the binary  $\delta\text{Vel}$  (Aa-Ab) is fixed at  $T = 45.150$  days. No apsidal motion of the eclipsing system has been noted since its discovery in 2000. The orbital inclination has been fixed at  $90^\circ$ , although given the stellar diameters and separations deduced in Section 6.3.2, the actual inclination could lie between  $87.5^\circ$  and  $92.5^\circ$ .

The best adjustment of the model to the measured visibilities and their 1-sigma statistical errors is shown in Fig. 6.2. It corresponds to a reduced mean squared deviation  $\chi_0^2 = 2.6$  and is obtained for the following parameter values:  $a = (5.7 \pm 0.3) \times 10^{10}\text{m}$ ,  $e = 0.230 \pm 0.005$ ,  $\Omega = (27.4 \pm 1.2)^\circ$ ,  $D_a = (6.0 \pm 0.5) D_\odot$ ,  $D_b = (3.3 \pm 0.6) D_\odot$ . The angle at primary eclipse is derived by the eccentricity as specified in Section 6.3.1:  $\omega = -(20 \pm 3)^\circ$ . The parameter uncertainties equal the statistical errors,  $\sigma$ , scaled by the reduced mean deviation of the model to the measurements, i.e.  $\chi_0 \sigma$ . The dependence of  $\chi^2$  on the stellar diameters is illustrated in Fig. 6.3.

The three visibilities measured on May 10, 2003 systematically deviate from the model fit (see Fig. 6.2). There is no evident explanation for this deviation: the data were obtained under good atmospheric conditions and the calibrator was the same as on the other nights. If the three points are removed, the quality of the fit is improved,  $\chi_0^2 = 1.4$ , but within the uncertainties, the resulting

parameter values are unchanged:  $a = (5.4 \pm 0.5) \times 10^{10} \text{m}$ ,  $e = 0.230 \pm 0.005$ ,  $\Omega = (29.2 \pm 2.4)^\circ$ ,  $D_a = (6.6 \pm 0.5) D_\odot$ ,  $D_b = (3.2 \pm 0.5) D_\odot$ .

It is apparent from the relatively high  $\chi_0^2$  that there are deviations in addition to the purely statistical errors. They might be due to an underestimation of the calibrator's size or might reflect some inaccuracies in the model for two uniformly bright, spherical stars. This is discussed in the subsequent section.

## 6.5 Results and discussion

### 6.5.1 The close eclipsing binary $\delta$ Vel (Aa-Ab)

The computations could be slightly biased if the diameter of the calibrator star were substantially misestimated or if HD 63744 were a – still undiscovered – binary system. On the other hand, HD 63744 is part of the catalog of interferometric calibrator stars by Bordé et al. [10], with its diameter ( $1.63 \pm 0.03$ ) mas specified to a precision of 1.8%. Furthermore, it has been studied simultaneously with other calibrator stars in VINCI observations by one of the authors (P. Kervella). In these investigations the visibilities of HD 63744 equal those expected for a single star of  $1.63 \pm 0.03$  mas diameter. Thus, HD 63744 appears to be a reliable calibrator.

Perhaps more relevant are the possible astrophysical complexities of  $\delta$  Vel (Aa+Ab) that are disregarded in the model of two uniformly bright, spherical stars. In particular, the rotational velocities of Aa and/or Ab are found to be high, with values of  $\sim 150 - 180$  km/s (Royer et al. [57]; Hempel et al. [33]; Holweger et al. [36]), which indicates that the two stars need not be uniformly luminous or circular.

Another possible over-simplification of our binary model is the constraint on the orbital inclination,  $i$ , being fixed at  $90^\circ$ . Given the fitted semi-major axis and stellar diameters, we note that the eclipse durations ( $0.51 \pm 0.05$  days and  $0.91 \pm 0.01$  days) are shorter than they should be in the case of  $i = 90^\circ$ , where the duration of the longer eclipse would have to exceed  $D_a T / (2\pi a) = 1.06$  days. We conclude that  $i$  is  $\sim 88^\circ$  or  $\sim 92^\circ$ , rather than  $90^\circ$ . All observations were performed out of eclipse and, therefore, the visibility values are nearly unaffected by such a small variation in  $i$ . With substantially more visibility measurements and an increased number of fitted parameters, the issue on the precise orbital inclination might be addressed in more detail.

The most important and remarkable result of our analysis is that the stellar diameters of Aa and Ab are found to equal  $6.0 \pm 0.5 D_\odot$  and  $3.3 \pm 0.6 D_\odot$ , respectively. This exceeds significantly, by factors  $\sim 1.4 - 3$ , the values expected if Aa and Ab are main sequence stars. If both diameters are constrained to lie below  $2.5 D_\odot$ , the best fit corresponds to  $\chi^2 = 16.7$ , which is far beyond the present result and confirms that large diameters are required to account for

the measured visibilities.

### 6.5.2 The physical association of $\delta$ Vel C and D

Ever since the observations of Herschel [34],  $\delta$ Vel has been taken to be a visual multiple star, with  $\delta$ Vel C and D the outer components of the system. With  $m_V$  of 11.0 mag and 13.5 mag (Jeffers et al. [38]), C and D would need to be of late spectral type, certainly no earlier than M, if they were as distant as  $\delta$ Vel (Aa+Ab+B). To our knowledge, the only existing spectra of C and D were recorded during a survey of nearby M dwarfs (Hawley et al. [32]). While the limited range and resolution of the spectra precluded ready determination of the spectral types of C and D, they were nevertheless estimated as  $\sim$ G8V and  $\sim$ K0V. Therefore, given their apparent magnitudes, C and D must be much farther away than  $\delta$ Vel (Aa+Ab+B). We conclude that  $\delta$ Vel C and D are not physically associated. Hence,  $\delta$ Vel ought to be only classified as a triple stellar system.

## 6.6 Summary

Seventeen VINCI visibility measurements of  $\delta$ Vel (Aa+Ab) were fitted onto the model of two uniformly bright, spherical stars. The adjustment to the measurements does not provide individual diameters compatible with A-type main sequence stars. The two stars thus appear to be in a more advanced evolutionary stage. More data are needed however to confirm this result. As the stellar evolution is fast during this period, more detailed knowledge of the system might also constrain the models more tightly. Precise photometric and spectroscopic observations of the eclipses should provide the separate intensities and chemical compositions of Aa and Ab and, hence, permit further inferences on the age and evolutionary state of  $\delta$ Vel.

*Acknowledgements: We thank Rosanna Faraggiana for her extensive help, Sebastian Otero for providing the light curves  $\delta$ Vel Aa, Ab, and Neil Reid for making the spectra of  $\delta$ Vel C, D available. The manuscript was improved by helpful comments from the referee.*



## Chapter 7

# Conclusion

The various subjects in this thesis have as a common denominator the effects of atmospheric turbulence on high-resolution astronomical observations. In conclusion the main results are summarized and some perspectives are given.

### Summary

#### **Interferometric observations of $\delta$ Velorum**

The study of the close, double-star system in  $\delta$  Velorum exemplifies the potential of interferometric observations: With a single telescope a mirror of 100-meter diameter would be required to resolve  $\delta$  Velorum Aa and Ab, but this resolution has here been achieved with two small 0.4 m telescopes placed 100 m apart.

The analysis of the observations suggests that the stellar diameters are considerably larger – by factors two to three – than indicated by their luminosity and the combined spectrum of  $\delta$  Velorum (Aa+Ab). Possibly the stars are older than previously assumed, and have reached the stage where the hydrogen in their cores has largely been converted into helium. They should then be expanding by now, while helium and heavier elements are being fused.

Interferometry falls short of providing images of a stellar system, it merely yields parameter values for an assumed model. In our case it excludes the possibility that  $\delta$  Velorum (Aa+Ab) is a system of two uniformly bright, spherical stars that are located on the main-sequence. Given the small amount of available data, the observations permit no more than this conclusion. In particular, it is not possible, at this point, to exclude a perhaps more realistic model that might include two circumstellar discs.

Further observations have recently been obtained with the new *Astronomical*

*Multiple Beam Recombiner*, AMBER, that is installed behind the *Very Large Telescope Interferometer*, VLTI, since 2001. The  $\delta$  Velorum binary (Aa+Ab) was observed with three 8 m-telescopes during three nights, i.e. at three different configurations of the double-star system. The analysis of the raw AMBER data is complex and has been carefully performed by Stefan Kraus from the Max-Planck Institut für Radioastronomie, Bonn. The results should permit an assessment of various double-star models, and given the present conclusion, these models should include alternatives, such as circumstellar discs.

It must be emphasized, that  $\delta$  Velorum can be observed interferometrically, because it is a particularly bright star. In fact, interferometry is, at present, essentially limited by its poor sensitivity. This limitation is due to the detrimental effects of turbulence and can only be overcome by phasing-devices when the turbulence is sufficiently slow. To make the best use of interferometers – and adaptive-optics as well – it is therefore essential to assess and specify the time-scales of atmospheric turbulence. The focus of this work has, accordingly, been on improved methods to measure these time scales at existing observatories and at potential observatory sites.

### **The coherence time of atmospheric turbulence**

Current corrections with adaptive-optics can react with sufficient amplitude to compensate for the atmosphere-induced phase distortions, but they fail to attain the high speeds that are required. While the necessary amplitude is determined by the turbulent intensity, the speed requirements reflect the time scales of turbulence. Accordingly, the site selection for the coming generations of single-dish telescopes and interferometers, should largely rely on the specification of the turbulence-time scales. But which quantity – or, possibly, which quantities – must be measured? Does the same parameter determine the operating performance of single dish-telescopes and of interferometers? Or are certain observational techniques more affected by high-altitude turbulent layers, while others are particularly sensitive to low-altitude turbulence?

To answer these questions, several quantities were examined, that are jointly termed “coherence time” while they are actually defined in relation to specific observational techniques with single-dish telescopes or with interferometers, with or without adaptive-optic systems. These various coherence-times are found to have almost the same dependance on the altitude profiles of turbulence and to be thus essentially equivalent. Accordingly, the sensitivity of interferometers and the performance of phasing devices and of adaptive-optic systems can be predicted by measuring one and the same quantity: the coherence time,  $\tau_0$ .

## How is the coherence time to be measured?

**Pistonscope** A first attempt was made to measure the coherence time with the *Pistonscope*, which is in essence a *Differential Image Motion Monitor*, DIMM, without prism. This endeavour turned out to be a very partial success for reasons inherent to the instrument. The pistonscope images a star through two small, circular openings, the resulting image being a fringe pattern within two, superimposed diffraction discs. The difference between the turbulence-induced motion of the interference pattern and that of the two diffraction discs is then used to assess the coherence time. The principal limitation of this method is that it involves the measurement of a small, differential movement that depends on the altitude-profile of the wind direction.

The pistonscope has been set up at Dome C, during daytime in February 2005. The measurements have provided promising lower limits for the coherence-times, but exact values could not be obtained, because the measurements are dependent on the unknown profiles of wind directions. The work has, thus, affirmed the need for an approach that allows regular monitoring of the coherence-time with an appropriate instrument.

**FADE** To measure the coherence time without continuous assessment of the wind directions, an instrument has been conceived that can be seen as an isotropic analogue to DIMM. The image of a star is shifted somewhat out of focus, which converts it – due to a central obstruction on the primary mirror – into a blurred ring. The image is then sharpened into a narrow ring by insertion of a lens with proper spherical aberration. Turbulence-induced variations of the defocus aberration cause, then, fast changes of the ring radius, and the coherence time and seeing are deduced from the amplitude and the velocity of these changes. The instrument is accordingly termed the *Fast Defocus Monitor*, FADE.

First observations with a prototype of the FADE monitor have been obtained at the Cerro Tololo observatory in October 2006. The resulting seeing values and coherence-times agree with simultaneous estimates in terms of the *Multi Aperture Scintillation Sensor*, MASS, and DIMM instruments.

FADE slightly underestimates the seeing; this bias is reproduced by simulations of somewhat blurred ring images, in the presence of optical aberrations or scintillation spots. We conclude that, to minimize the effects of scintillation and telescope aberrations on the FADE monitor, relatively sharp ring images are needed, close to the diffraction limit.

## Further work required

### Bringing the coherence-time monitor into practical use

**Further tests** The initial coherence-time estimates were obtained with the prototype of FADE and have been compared to results from the MASS monitor. MASS is based on scintillation measurements and is, therefore, insensitive to the low turbulent layers roughly below 500 m altitude. The actual coherence times are, accordingly, obtained from combined observations with MASS and DIMM. This estimation is indirect and can not be used to test the validity of the coherence times derived in terms of FADE.

To check the validity of the FADE estimates, observations must be obtained in parallel to measurements by an adaptive optics system or by an interferometer. Simultaneous measurements with FADE and with NAOS, the adaptive-optic system installed behind one of the VLT telescopes, are, therefore, planned for August 2007 at the observatory of Paranal.

**Making FADE user friendly** Two major requirements must be met to establish FADE as a regular monitoring instrument. First, an automatic procedure needs to be incorporated for bringing the ring-image close to its diffraction-limit and then measuring its width. Secondly there needs to be a standard data-acquisition chain.

These conditions can not be attained with the current, commercial camera-software, and a suitable software is, therefore, now being developed at the observatoire de Meudon; it should be available for the forth-coming observations, in August 2007.

### Application at Dome C, Antarctica

The measurements with the MASS monitor at the *Concordia* station on Dome C, suggest that the coherence time of the high-altitude turbulence is at this location considerably longer than at mid-latitude sites [46]. On the other hand, estimates of seeing by the DIMM have shown that the low-layer turbulence might be particularly strong at Dome C [2]. This raises a decisive question. Should coming generations of large telescopes and interferometers be installed at *Concordia*? Should they then be placed twenty or forty meters above the ground?

This being an important issue, direct measurements of the coherence time need to be performed. FADE may be ideally suited for such measurements, provided the experimental setup can resist antarctic temperatures. FADE's survival-ability under antarctic conditions is, therefore currently examined.

# Bibliography

- [1] Absil, O., den Hartog, R.H., Gondoin, P.A., et al., *A&A*, 448, 787 (2006)
- [2] Agabi, A., Aristidi, E., Azouit, M., et al., *PASP*, 118, 344 (2006)
- [3] Alekseeva, G.A., Arkharov, A. A., Galkin V. D. et al., *Pulkovo Spectrophotometric Catalog* (1997)
- [4] Argyle, R. W., Alzner, A. , & Horch, E. P., *A&A*, 384, 171 (2002)
- [5] Aristidi, E., Agabi, K., Fossat, E., et al., *A&A*, 444, 651 (2005)
- [6] Avila, R., Vernin, J., Chun M.R., et al., *Proc. SPIE*, 4007, 721 (2000)
- [7] Avila, R., Ziad, A., Borgnino, J., et al., *J. Opt. Soc. Am. A.*, 14, 3070 (1997)
- [8] Azouit, M., & Vernin, J., *PASP*, 117, 536 (2005)
- [9] Bonfils, X., Forveille, T., Delfosse, X., et al., *A&A*, 443, L15 (2005)
- [10] Bordé, P., Coudé du Foresto, V., Chagnon, G. & Perrin, G., *A&A*,393,183B (2002)
- [11] Butterley, T., Wilson, R., & Sarazin, M., *MNRAS*, 369, 835 (2006)
- [12] Central Intelligence Agency, Reference maps, <https://www.cia.gov/library/publications/the-world-factbook/docs/refmaps.html>
- [13] Colavita, M.M., Shao, M., & Staelin, D.H., *Appl. Opt.*, 26, 4106 (1987)
- [14] Conan, R., Borgnino, J., Ziad, A., et al., *J. Opt. Soc. Am. A*, 17, 1807 (2000)
- [15] Conan, R., Ziad, A., Borgnino, J. et al., *proc. SPIE*, 4006, 963 (2000)
- [16] Conan, J.-M., Rousset, G., & Madec, P.Y., *J. Opt. Soc. AM. A*, 12, 1559 (1995)
- [17] Davidson, P.A., *Turbulence – An Introduction for Scientists and Engineers*. Oxford University Press, 1st ed. (2004)
- [18] The drawings of Leonardo da Vinci, <http://www.drawingsofleonardo.org/>
- [19] Eggleton, P. P., *ApJ*, 268, 368E (1983)

- [20] European Centre for Medium-Range Weather Forecasts, <http://www.ecmwf.int/> (2007)
- [21] Fuchs, A., Tallon, M., & Vernin, J., *PASP*, 110, 86 (1998)
- [22] Fusco, T., Ageorges, N., Rousset, G., et al., *proc. SPIE*, 5490, 118 (2004)
- [23] Gendron, E., Léna, P., *Ap&AS*, 239, 221 (1996)
- [24] Glindemann, A., Bauvir, B., van Boeckel, R., et al., *LIACo*, 36, 27 (2001)
- [25] Gradshteyn, I.S., & Ryzhik, I.M., *Table of integrals, series, and products*. New York: Academic Press, 5th ed. (1965)
- [26] Gray, R. O., & Garrison, R. F., *ApJS*, 65, 581 (1987)
- [27] Greenwood, D.P., & Fried, D.L., *J. Opt. Soc. Am.*, 66, 193 (1976)
- [28] Habib, A., Vernin, J., Benkhaldoun, Z., & Lanteri, H., *MNRAS*, 368, 1456 (2006)
- [29] Hardy, J.W., *Adaptive Optics for Astronomical Telescopes*. Oxford: Oxford Univ. Press (1998)
- [30] Harmanec, P., *A&A*, 335, 173 (1998)
- [31] Hawley, S., Gizis, J. E., & Reid, I. N., *AJ*, 112(6), 2799 (1996)
- [32] Hempel, M., Holweger, H., & Kamp, I., *CoSka*, 27, 246 (1998)
- [33] Herschel, J. F. W., London, Smith, Elder and co. (1847)
- [34] Hoffleit, D., Warren, W. H., *The Bright Star Catalogue*, 5th Revised Ed. (Preliminary Version) (1991)
- [35] Holweger, H., Hempel, M., & Kamp, I., *A&A*, 350, 603 (1999)
- [36] Innes, R.T.A., *MNRAS*, 55, 312 (1895)
- [37] Jeffers, H. M., van den Bos, W. H., & Greeby, F. M., *Publications of the Lick Observatory* (1963)
- [38] Johnson, H. L., Iriarte B., Mitchell R. I., & Wisniewski W. Z., *CoLPL*, 4, 99 (1966)
- [39] Kervella, P., Thévenin, F., Ségransan, D., et al., *A&A*, 404, 1087 (2003)
- [40] Kellerer, A., Sarazin, M., Coudé Du Foresto, et al., *Applied Optics*, 45, 5709 (2006)
- [41] Kellerer, A., & Tokovinin, A., *A&A*, 461, 775 (2007)
- [42] Kolmogorov, A.N., “About the Analytical Methods of Probability Theory” in: *Selected works of A.N. Kolmogorov*, vol. 1, ed. Tikhomirov, V. M.. Springer-Verlag (2001)
- [43] Kornilov, V., Tokovinin, A., Vozyakova, O., et al., *Proc. SPIE*, 4839, 837 (2003)

- [44] Landau, L.D., Lifshitz, E.M., Fluid Mechanics. Pergamon Press, 1st edition (1959)
- [45] Lawrence, J.S. , Ashley, M.C.B., Tokovinin, A., & Travouillon, T., Nature, 431, 278 (2004)
- [46] Lawrence Livermore National Laboratory, University of California, <http://www.llnl.gov/str/June05/Carrano.html>
- [47] Levato, O. H., PASP, 82, 584 (1972)
- [48] Lopez, B., A& A, 253, 635 (1992)
- [49] Markwardt, C., Mpfir version 1.38, <http://cow.physics.wisc.edu/~craigm/idl/fitting.html> (2005)
- [50] Noll, R., J. Opt. Soc. Am., 66, 207 (1976)
- [51] Otero, S. A., Fieseler, P. D., & Lloyd, C., IBVS, 4999 (2000)
- [52] Otero, S.A., [http://ar.geocities.com/varsao/delta\\_Velorum.htm](http://ar.geocities.com/varsao/delta_Velorum.htm) (2006)
- [53] Perrin, M.D., Sivaramakrishnan, A., Makidon, R.B. et al., ApJ, 596, 702 (2003)
- [54] Perryman, M.A.C., Lindegren, L., Kovalevsky, J. et al., A&A, 323, L49 (1997)
- [55] Richardson, L.F., Proc. Roy. Soc. London A, 110, 709 (1926)
- [56] Royer, F., Gerbaldi, M., Faraggiana, R., & Gomez, A.E., A&A, 381, 105 (2002)
- [57] F. Roddier, Prog. Optics, 19, 281 (1981)
- [58] Sarazin, M., & Tokovinin, A., in: Beyond conventional adaptive optics, eds. E. Vernet, R. Ragazzoni, S. Esposito, N. Hubin, ESO Conf. Workshop Proc. No. 58, Garching: ESO (2002)
- [59] Sarazin, M., & Roddier, F., A&A, 227, 294 (1990)
- [60] Sasiela, R.J., Electromagnetic Wave Propagation in Turbulence. Berlin: Springer-Verlag (1994)
- [61] Schoeck, M., Spillar, E.J., J. Opt. Soc. Am. A, 17, 1650 (2000)
- [62] Schoeck, M., & Spillar, E.J., SPIE, 3353, 1092 (1998)
- [63] Tango, W.J., & Twiss, R.Q., Progress in Optics, XVII, 239 (1980)
- [64] Tango, W.J., Davis, J., Thompson, R.J., & Hanbury, R., PASAu, 3, 323 (1979)
- [65] Taylor, G.I., Proc. R. Soc. Lond. A, 164, 476 (1938)
- [66] Tokovinin, A. & Heathcote, S. PASP, 118, 1165 (2006)
- [67] Tokovinin, A., Appl. Opt., 41, 957 (2002)

- [68] Tokovinin, A., *A&A Suppl. Ser.*, 124, 75 (1997)
- [69] Wikipedia, Concordia Station, [http://en.wikipedia.org/wiki/Concordia\\_Station](http://en.wikipedia.org/wiki/Concordia_Station)
- [70] Worley, C.E., & Douglass, G.G., *A&A Suppl.*, 125, 523 (1997)
- [71] Wright, C.O., Egan, M.P., Kraemer, K.E., & Price, S.D., *The Tycho-2 Spectral Type Catalog* (2003)
- [72] Ziad, A., Conan, R., & Tokovinin, A., et al., *Appl. Opt.*, 39, 5415 (2000)

**Summary** The research brought together in this thesis is concerned with the distortion of astronomical observations due to atmospheric fluctuations. These fluctuations are especially critical for the technique of interferometry whose potential is here exemplified by the study of  $\delta$  Velorum. The focus of the research is, accordingly, on improved methods to assess the changing viewing conditions at existing observatories, as well as to determine the suitability of potential observatory sites.

Site-testing and site-monitoring missions are usually directed at the assessment of the Fried parameter with instruments such as the *Differential Image Motion Monitor*, DIMM. An estimation of the coherence time requires then, in addition, wind-speed measurements by weather stations. A more refined evaluation is obtained with instruments such as the *Multi Aperture Scintillation Sensor*, MASS, that measure the altitude profiles of the index structure constant,  $C_n^2$ , and the wind speed with a resolution of about 500 m, and infer the coherence time from the integrated turbulence profiles. The main error in the estimated coherence time results from the turbulence below 500 m altitude not being accounted for.

To avoid these complexities, we suggest the direct measurement of a quantity proportional to the coherence time. The variance of the defocus velocity is a suitable option, because it can be evaluated through fast and continuous sampling of the atmospheric defocus coefficient. The concept of a *Fast Defocus Monitor*, FADE, an instrument using a small telescope, some simple optics and a fast camera is described, and first measurements are presented.

The final aim is to use FADE for site monitoring and site testing campaigns. A particularly challenging and interesting project will be to monitor the coherence time at Dome C.

**Résumé** La vie sur Terre est rendue possible grâce au rideau protecteur que constitue l'atmosphère. Avec sa masse équivalente à dix mètres d'eau, l'atmosphère est une condition préalable à l'apparition de la vie. Mais ce rideau rend la vie difficile aux astronomes qui préféreraient avoir une vue directe sur l'Univers. Il est donc indispensable de caractériser et de spécifier les conditions atmosphériques qui permettent la meilleure utilisation des systèmes d'optiques adaptatives et des interféromètres – les interféromètres, dont le potentiel est ici illustré à travers les observations d'un système de trois étoiles,  $\delta$  Velorum.

Le temps de cohérence de la turbulence est un paramètre essentiel qui détermine la sensibilité des interféromètres et la performance des systèmes d'optiques adaptatives. Il existe plusieurs instruments qui mesurent le temps de cohérence ou des paramètres reliés, mais tous ces instruments ont des limitations intrinsèques: ou bien ils nécessitent de grands télescopes, ou bien l'analyse des données est complexe, ou encore la méthode n'est sensible qu'à une partie de la turbulence. C'est pourquoi les campagnes de tests de sites et de monitoring reposent principalement sur la mesure du *seeing*, avec des instruments comme le *Differential Image Motion Monitor*, DIMM.

Pour palier à ce manque, nous avons proposé un instrument pour mesurer le temps de cohérence: le *Fast Defocus Monitor*, FADE. La méthode consiste à transformer l'image d'une étoile, à travers un petit télescope de 0.35 m de diamètre, en un anneau fin. La turbulence cause alors des variations temporelles du rayon de l'anneau, dont la vitesse et l'amplitude sont reliées au temps de cohérence et au *seeing*. Cette méthode est présentée ici avec les résultats de premières observations.